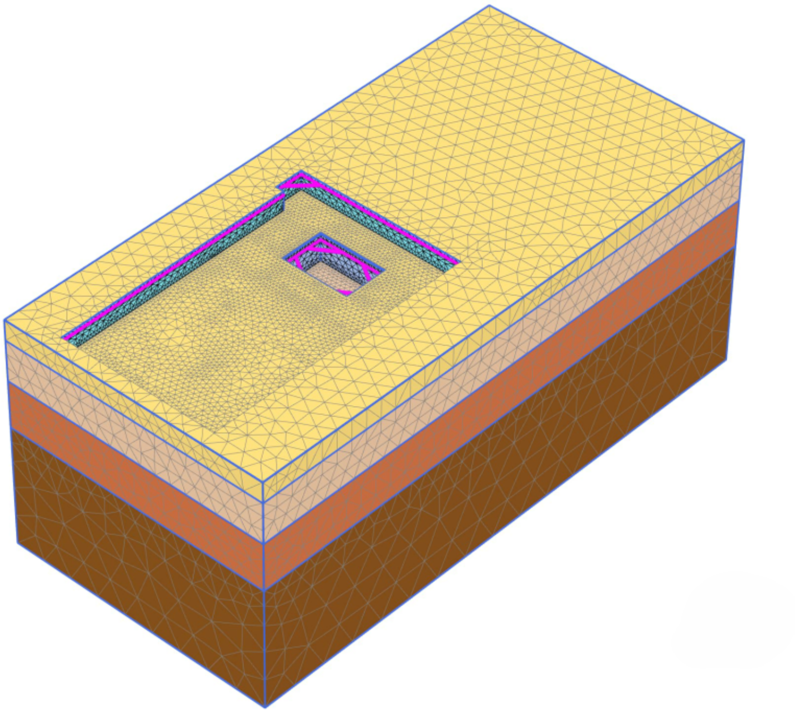

2D and 3D Numerical Modelling of Sheet Pile Walls in Soft Clay

Comparison of NGI-ADP and Creep-SCLAY1S

Master's thesis in the Master's Programme Infrastructure and Environmental Engineering

EMIL TOLL WESTER

OLIVER SJÖLUND

DEPARTMENT OF ARCHITECTURE AND CIVIL ENGINEERING
DEVISION OF GEOLOGY AND GEOTECHNICS

CHALMERS UNIVERSITY OF TECHNOLOGY
Master's thesis ACEX30
Gothenburg, Sweden 2024

MASTER'S THESIS ACEX30

2D and 3D Numerical Modelling of Sheet Pile Walls in Soft Clay
Comparison of NGI-ADP and Creep-SCLAY1S

Master's Thesis in the Master's Programme Infrastructure and Environmental Engineering

EMIL TOLL WESTER
OLIVER SJÖLUND

CHALMERS
UNIVERSITY OF TECHNOLOGY

Department of Architecture and Civil Engineering
Division of Geology and Geotechnics
CHALMERS UNIVERSITY OF TECHNOLOGY
Gothenburg, Sweden 2026

2D and 3D Numerical Modelling of Sheet Pile Walls in Soft Clay
Comparison of NGI-ADP and Creep-SCLAY1S
Master's Thesis in the Master's Programme Infrastructure and Environmental Engineering

EMIL TOLL WESTER

OLIVER SJÖLUND

Supervisor: Lucas Hansson, Norconsult AB
Supervisor: Lisa Sundström, Norconsult AB
Examiner: Minna Karstunen, Department of Architecture and Civil Engineering

Examensarbete ACEX30
Institutionen för Arkitektur och Samhällsbyggnadsteknik
Chalmers Tekniska Högskola, 2026

Department of Architecture and Civil Engineering
Division of Geology and Geotechnics
Chalmers University of Technology
SE-412 96 Göteborg
Sweden
Telephone +46 31 772 1000

Cover:
Final mesh of the site used in PLAXIS 3D, Figure 3.16.
Department of Architecture and Civil Engineering
Göteborg, Sweden, 2026

2D and 3D Numerical Modelling of Sheet Pile Walls in Soft Clay
Comparison of NGI-ADP and Creep-SCLAY1S

Master's thesis in the Master's Programme Infrastructure and Environmental Engineering

EMIL TOLL WESTER

OLIVER SJÖLUND

Department of Architecture and Civil Engineering
Division of Geology and Geotechnics
Chalmers University of Technology

ABSTRACT

This thesis examines the behavior of sheet pile walls in soft clay in 2D and 3D finite element analyses using PLAXIS, with a focus on comparing the constitutive models NGI-ADP and Creep-SCLAY1S. The study is based on the ground construction of Hotel Draken at Järntorget in Gothenburg, where sheet pile walls of type PU12 and AZ18 were used to retain the soil during a staged excavation. The northern outer sheet pile wall was selected as the primary element of analysis, since inclinometer measurements were available for this wall.

Both 2D and 3D models were created to simulate the construction sequence, including installation of sheet pile walls, staged excavation, casting of concrete, and installation of waling beams and corner struts. To address the impact of surcharge loading from machines or other equipment, two load scenarios were investigated. A sensitivity analysis was also performed for the sheet pile walls on the anisotropic plate input parameters in 3D.

The results from the analyses show that the 2D plane-strain assumption overestimates the horizontal displacement compared to 3D. However, the choice of constitutive model also proved equally, or even more influential than the choice of dimensionality even for a non-symmetrical complex geometry. The more advanced Creep-SCLAY1S model produced results closer to the measured inclinometer data compared to the NGI-ADP model. The inclusion of surcharge loads from construction machinery was found to significantly affect the predicted displacement profile both in 2D and 3D, particularly in the upper portion of the wall. The sensitivity analysis of the anisotropic plate parameters regarding the area moment of inertia I_2 and I_{12} in the 3D model showed to have negligible influence on computed wall displacements.

Key words: PLAXIS 2D, PLAXIS 3D, Sheet pile walls, Excavation, Numerical modelling, Finite Element Method, NGI-ADP, Creep-SCLAY1S

2D och 3D numerisk modellering av spontväggar i mjuk lera
Jämförelse av NGI-ADP och Creep-SCLAY1S

Examensarbete inom masterprogrammet Infrastruktur och Miljöteknik

EMIL TOLL WESTER

OLIVER SJÖLUND

Institutionen för arkitektur och samhällsbyggnadsteknik
Avdelningen för Geologi och Geoteknik
Chalmers tekniska högskola

SAMMANFATTNING

Detta examensarbete undersöker beteendet hos spontväggar i lös lera med hjälp av 2D- och 3D-finita elementanalyser i PLAXIS, med fokus på att jämföra de konstitutiva modellerna NGI-ADP och Creep-SCLAY1S. Studien baseras på grundläggningsarbetet för Hotell Draken vid Järntorget i Göteborg, där spontväggar av typerna PU12 och AZ18 användes för att hålla tillbaka jorden under stegvis schaktning. Den norra yttre spontväggen valdes som huvudsakligt analysobjekt, eftersom inklinometermätningar fanns tillgängliga för denna vägg.

Både 2D- och 3D-modeller skapades för att simulera byggprocessen, inklusive installation av spontväggar, stegvis schaktning, gjutning av betong samt installation av hammarband och hörnsträvor. För att beakta effekten av ytlast från maskiner eller annan utrustning studerades två lastfall. En känslighetsanalys genomfördes också för spontväggarna med avseende på de anisotropa väggelementens indata i 3D.

Resultaten från analyserna visar att 2D-analysen överskattar de horisontella deformationerna jämfört med 3D. Valet av konstitutiv modell visade sig dock vara lika eller även mer avgörande än valet av dimension, även för en icke-symmetrisk och komplex geometri. Den mer avancerade modellen Creep-SCLAY1S gav resultat som låg närmare de uppmätta inklinometerdata jämfört med NGI-ADP-modellen. Inkluderingen av ytlast från byggmaskiner visade sig ha en betydande inverkan på den beräknade deformationsprofilen både i 2D och 3D, särskilt i den övre delen av väggen. Känslighetsanalysen av de anisotropa väggelementens parametrar som avser yttröghetsmomenten I_2 och I_{12} i 3D-modellen visade att dessa har försumbar inverkan på de beräknade väggdeformationerna.

Nyckelord: PLAXIS 2D, PLAXIS 3D, Spontväggar, Numerisk modellering, Finita Elementmetoden, NGI-ADP, Creep-SCLAY1S

Contents

Preface

This master's thesis was conducted as part of the Department of Architecture and Civil Engineering at Chalmers University, in collaboration with Norconsult. The work was carried out at Norconsults office in Gothenburg.

We would like to express our sincere gratitude to our supervisors at Norconsult, Lucas Hansson and Lisa Sundström for their valuable feedback and support during this project. A special thanks to our supervisor and examiner at Chalmers, Minna Karstunen, who provided guidance and valuable insights throughout the entire semester. We would also like to thank the employees at the geotechnics department at Norconsult, for the support and interest in our work, and for making us feel welcome.

Gothenburg, June 2026
Emil Toll Wester & Oliver Sjölund

1 Introduction

Sheet pile walls are often used as retaining structures in excavations performed in soft clay in urban areas, where there is limited space and existing buildings and infrastructure nearby. To properly predict the behavior of these walls, numerical modelling can be used. However, the accuracy of the numerical models are highly dependent on the choice of the constitutive model, input parameters and boundary conditions, as well as if the analysis is done in 2D or 3D.

For geotechnical projects, two-dimensional finite element analysis is the most common method for cases like these. The 2D-analysis assumes a plane strain condition, where all deformations occur in one plane. In most cases this is a conservative assumption. Although 2D analysis is a computationally efficient method that is well researched, it still has limitations in certain cases. When utilized for complex three-dimensional geometries, especially ones including structural elements that reach into the third dimensions, such as waling beams and corner struts, the simplified plane strain assumption can produce inaccurate results, leading to over- or underestimation of the stresses and the movements of the soil and structural elements. A 3D-analysis is sometimes more suitable for these scenarios, since it can better capture the real-life behavior of the soil and structures, with the drawback of having greater computational cost and being more complex to model.

Selecting the right constitutive model for the soil is also important for an accurate result. The soft clays found in Gothenburg have low shear strength, they are compressible and sensitive, and also anisotropic. To capture the response of this type of soft clay, two different constitutive models have been developed - NGI-ADP and Creep-SCLAY1S. The NGI-ADP model is an undrained total stress model that directly takes the input of shear strengths to capture the anisotropic behavior of clay, suitable for analyses of short-term response. The Creep-SCLAY1S model is a rate dependent effective stress model that takes anisotropy, destructuration, and creep into account, which enables modelling of the construction as a time-dependent process.

1.1 Case study

On behalf of Hotell Draken AB, Norconsult AB was tasked in 2016 with carrying out a geotechnical site investigation and the designing of earth retaining structures for the construction of a new hotel connected to Folkets hus at Järntorget in Gothenburg. The hotel was to be built adjacent to several existing buildings and in close proximity to the western opening of the Göta Tunnel, approximately 10 meters north of the area. The hotel, which was to be the tallest building in the area housing a parking garage in the basement, required both sheet piling for excavation of masses, and subsequent piling due to the deep clay depositions. An important consideration when constructing a subsurface facility in an urban environment is the impact of ground movements. Because of the nearby sensitive structures at Järntorget, an inclinometer was placed adjacent to the northern sheet piles, and measuring studs were placed around the entire area, after which special alarm and limit values were set to protect the Göta Tunnel in particular.

To properly predict the behavior of the construction, different tests were performed on the soil in the area. This allowed the evaluation of the soil layering and composition. The stratification of the area where the construction took place begins with 2-4 meters of fill material. This fill consists of a variety of materials, with sand being the main material, but gravel, clay, stones, and construction materials such as concrete, wood, and bricks. Following this, there is a clay layer that starts as dry crust but transitions into a soft clay that reaches at most down to a depth of 45 meters. Shell fragments, mud, sand, silt, and plants can be found in the clay. Below, there is a layer of frictional soil with a thickness of 0 to 3 meters, which overlays the bedrock. The groundwater level sits at about a depth of 2 meters, at level +0.

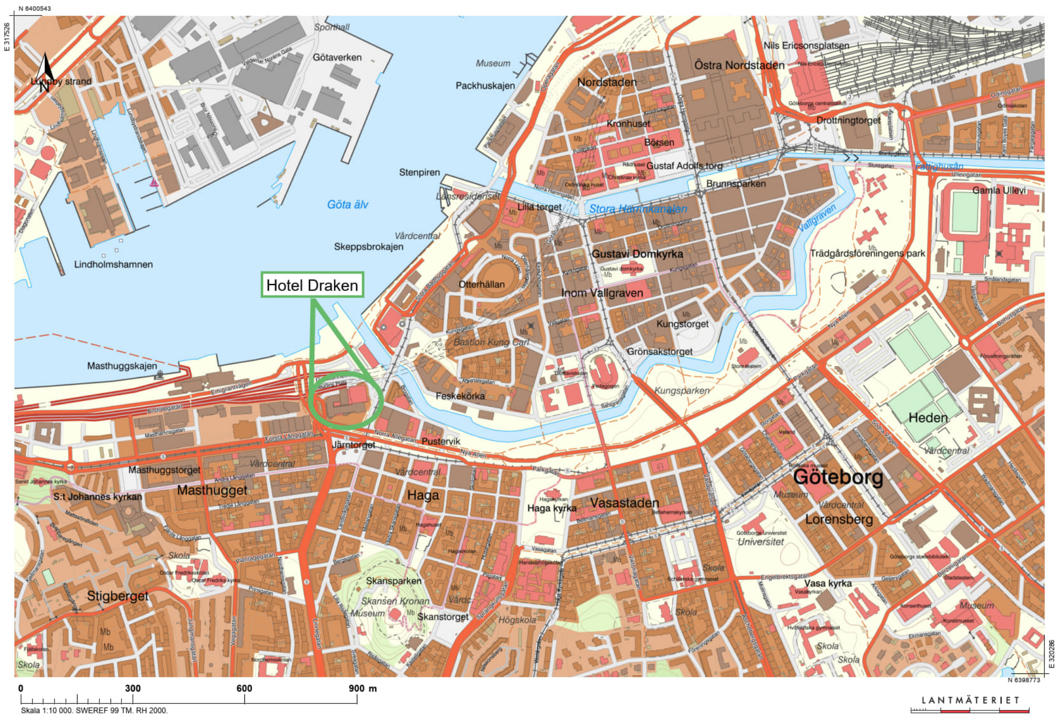

Figure 1.1: Map of the project area and its location in Gothenburg marked with green.

1.2 Earlier research

Earlier studies have been made regarding the 3D effects on ground movement around supported excavations in clay. Finno et al. (2007) conducted 150 finite element analyses in PLAXIS 2D and 3D FOUNDATION to determine when when a simpler 2D plane strain model is sufficient and when a full 3D analysis is necessary. The influence of the excavation geometry was determined by the Plane Strain Ratio (PSR), defined as the maximum wall movement from 3D analysis normalized by the maximum wall movement from 2D plain strain analysis. For a PSR of 1, the maximum wall movement from 3D analysis and the maximum wall movement from 2D plain strain analysis produce the same results.

Finno et al. (2007) concluded that the PSR approached 1 as L/H_e (wall length/Excavation depth) approached 6, making 2D plane strain analysis sufficient. For wall length to excavation depth ratio < 6, the 3D effects become significant and 2D analyses overpredict movement. Additionally, if all else are kept the same, lower L/B (wall length/wall width) produced lower PSR values, stiff wall systems produce lower PSR and lower factors of safety against basal heave produced lower PSR. The authors therefore also proposed an empirical formula incorporating both the wall length to excavation depth ratio L/H_e, the excavation aspect ratio L/B, the wall stiffness factor k and the basal heave stability factor C. It should however be noted that the most influential parameter was the wall length to excavation depth ratio L/H_e.

Even though Finno et al. (2007) considered different lengths, widths and wall stiffnesses, the geometry was still relatively simple. This suggests that this may not be applicable in more complex excavations such as at Hotel Draken, where the width is non-uniform and multiple excavations are carried out in close proximity.

The anisotropic behavior of 3-dimensional sheet pile walls for staged excavations in soft clay, with a focus on the input parameters, was also studied by Persson and Sigström (2010). The authors found that the PLAXIS user manual recommended procedure for estimating the anisotropic behavior of plate elements in 3D yields a wall that is too stiff. Instead, they suggested that the area moment of inertia $I_2 = I_1/7533$ and $I_{12} = I_1/100$. Sheet pile walls are not equally stiff in all directions because of their corrugated geometry, so the authors used manufacturer section properties to define the flexural rigidity in the horizontal direction but estimated the flexural rigidity in the vertical direction by modelling of corrugated sections in PLAXIS 2D and 3D FOUNDATION. However, this can be questioned since the moment of inertia against bending over the horizontal axis for the entire wall was used to simulate the behavior of the individual steel plates that comprised the corrugated beam, instead of directly using the area moment of inertia for each plate.

1.3 Aims and objectives

This study aims to analyze how the predicted displacement of a sheet pile wall differ between PLAXIS 2D and PLAXIS 3D, by simulating the ground construction process for Hotel Draken in Gothenburg.

The following objectives were considered:

- Model the construction site of Hotel Draken in 2D and 3D to compare the deformations and structural forces in a sheet pile wall.
- Compare how the two constitutive models NGI-ADP and Creep-SCLAY1S affect the behavior and deformation of a sheet pile wall.
- Investigate how sheet pile walls should be modelled in 3D, and assess the sensitivity of the parameters simulating anisotropy.
- Evaluate how applied loads simulating the machines used for construction affect the results of numerical analysis in 2D and 3D.

1.4 Limitations / Demarcations

- Only the study area of Hotel Draken is analyzed
- Only the outer northern sheet pile wall used for construction of Hotel Draken is analyzed.
- Only using the constitutive soil models NGI-ADP and Creep-SCLAY1S for the clay and Mohr-Coulomb for the fill.

1.5 Societal, ethical and ecological impacts

This thesis contributes to safer and more reliable urban excavation design. Societal and ethical impacts are related to infrastructure safety, as the movements of the retaining walls can affect nearby buildings, tunnels, and public spaces, with potentially severe economic and social consequences. Ecological impacts are not assessed.

2 Background

The following chapter presents and discusses theory that is of relevance to the project, so that the reader can understand the ideas presented in this thesis.

2.1 Basic soil mechanics

Firstly, it can be beneficial to to provide some basic concepts and terminology in order to easier understand the field of geotechnics. The most fundamental to soil mechanics being *The Principal of Effective Stress* proposed by Terzaghi in 1943. The principal recognizes that the forces vertically transmitted by fully saturated soil per unit area can be defined as the sum of effective stresses transmitted by the soil skeleton σ' and the pore water pressure in the void space between particles u. The total stress (σ) can therefore simply be described as the saturated unit weight of soil γ_{sat}, per unit depth (z) (Equation 2.1). γ_w is the unit weight of water.

$$\sigma = \sigma' + u = (\gamma_{sat} - \gamma_w)z + \gamma_w z = \gamma_{sat} z \tag{2.1}$$

2.1.1 Mohr-Coulomb Failure Criterion

A soil element in a two-dimensional stress space requires the description of both normal effective vertical stress σ'_z, normal effective horizontal stress σ'_x and shear stress τ_{xz} in order to describe the state at which the soil reaches failure. The yield point, beyond which plastic deformation occur, can be described by the *Mohr-Coulomb Failure Criterion* by assuming perfectly plastic behavior (Knappett and Craig, 2012). The principal stresses acting on the soil is then sufficient for representing the prevailing stress state by drawing of a Mohr's circle (Figure 2.1). For a two-dimensional soil element the major principal stress (σ'_1) and the minor principal stress (σ'_3) are often the vertical stress (σ'_z) and horizontal stress (σ'_x), respectively. When a stress state occurs at which the soil reaches failure, shear and effective normal stresses overcome the shearing resistance from the internal friction of the soil particles (φ') and the apparent cohesion (c'). At failure the Mohr's circle touches the failure envelope, representing the shear strength of the soil (Equation 2.2).

$$\tau_f = c' + \sigma' tan\varphi' \tag{2.2}$$

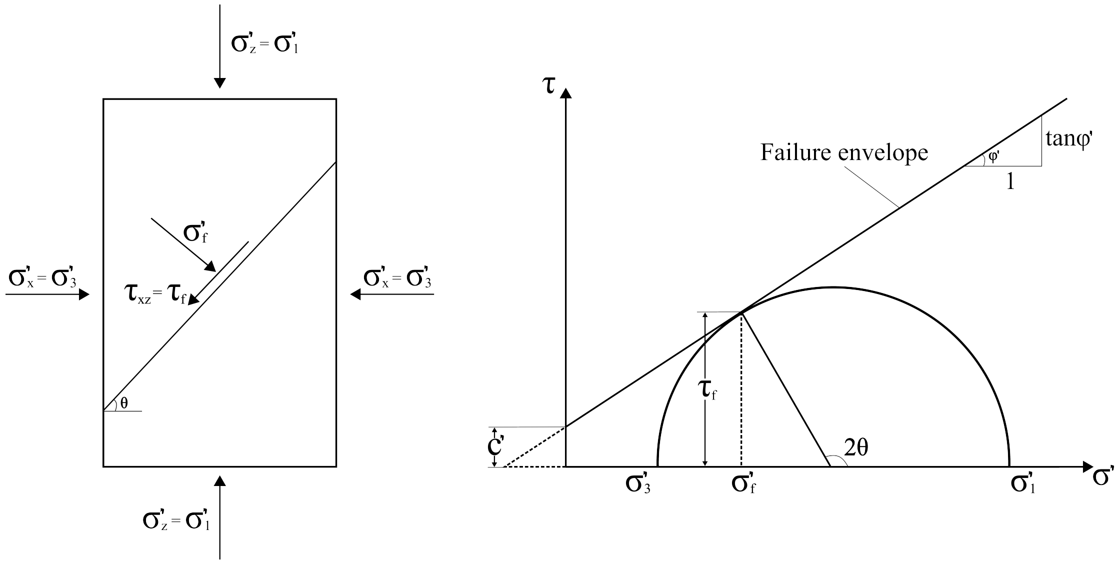

Figure 2.1: The Mohr-Coulomb failure criterion shown in a Mohr's circle.

2.1.2 Sheet pile walls and Rankine's Theory of Earth Pressure

Sheet pile walls are commonly used structures that support excavations (Bilgin, 2010). They consist of vertical sheets of steel piles that are interlocked with each other, forming together a barrier that can hold back the soil and water (U.S. Army Corps of Engineers (Department of the Army), 1994). Timber and reinforced concrete walls can also be used as an alternative to sheet pile walls. Sheet pile walls can undergo significant deformations because of their low system stiffness and are therefore considered as flexible walls. They can also be supported with struts across the excavation to maintain its stability (Bilgin, 2010).

Additionally, wailing beams can be added to support the structure. The waling beams are horizontal beams, often made of steel, that can be welded to a sheet pile wall. They have several purposes, but the main function is to distribute the load that acts along the sheet pile wall and transfer the forces from the strut to the sheet piles. The horizontal stresses acting on the wall in a state of shear failure or plastic equilibrium of the soil can be described by *Rankine's Theory of Earth Pressure*. Initially, when the soil is in a state of rest, the ratio of the in-situ horizontal effective stress (σ'_{h_0}) to in-situ vertical effective stress (σ'_{v_0}) is determined by the coefficient of lateral earth pressure at rest (K_0).

$$K_0 = \frac{\sigma'_{h_0}}{\sigma'_{v_0}} \tag{2.3}$$

When the soil movement is large enough behind a wall, the horizontal stresses will decrease until the current stress state touches the failure envelope in which plastic equilibrium occurs. When the wall moves away from the soil towards the excavation, the limiting state is known as the active condition. The vertical stress is the major principal stress and the horizontal stress is the minor principal stress. On the other side of the wall, the horizontal stresses will instead increase until the current stress state touches the failure envelope in which plastic equilibrium occurs. When the wall moves towards the soil, the limiting state is known as the passive condition. The vertical stress now becomes the minor principal stress and the horizontal stress become the major principal stress. The active pressure and passive pressures can be considered as limit pressures, since they are a minimum and maximum value respectively (Knappett and Craig, 2012).

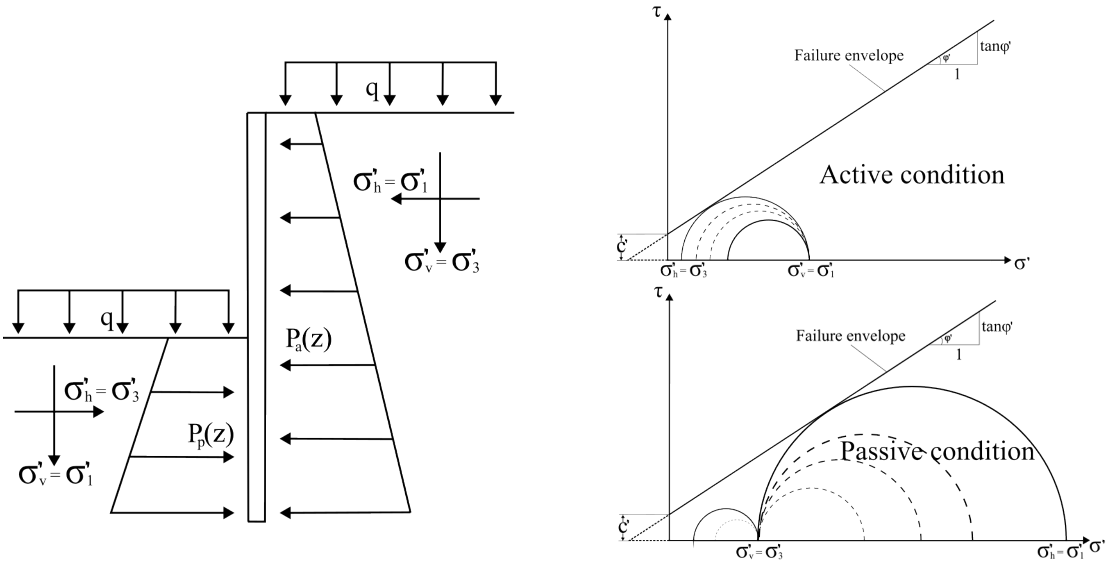

Figure 2.2: Rankine's Theory of Earth Pressure.

There are three types of sheet pile walls commonly used for providing lateral earth support, namely cantilever walls, braced walls, and anchored walls. Cantilever sheet pile walls rely entirely on the passive earth pressure below the excavation for stability. On the other hand, anchored sheet pile walls use tie-back anchors to stabilize the wall, while braced walls use walers and struts. The height of the wall affects which type of wall can be used, with higher walls needing to be supported by struts or anchors, while cantilever walls can be utilized for shorter wall heights (Bilgin, 2010).

The sheet piles are installed by driving them into the ground, and the soil is excavated once the wall is fully installed. The way that the sheet pile wall is installed will have an effect on how the soil surrounding the wall is loaded and deformed, which in turn will affect the behavior of the wall. Furthermore, the installation of the walls (and anchors) will disturb the soil. The construction method is not taken into account in the classical methods based on limit equilibrium. However, numerical models, like the finite element method, can model the entire construction process (Bilgin, 2010).

There are several failure states that need to be checked for when designing a sheet pile wall. A cantilever wall can fail by horizontal translation of the wall, by rotation of the wall, and bearing failure of the wall. For anchored walls there are additional failure checks to be considered. These are failure by the anchor being pulled out of the soil, and structural failure of the anchors (Knappett and Craig, 2012). Likewise, for walls with props and wailers, the structural capacity needs consideration.

The flexibility or stiffness of a sheet pile wall will affect its behavior. In flexible walls, arching can occur. Arching is the condition in which there is an increase in pressure on the parts of the wall that are unyielding and a decrease in pressure on the parts of the wall that are yielding. The lateral earth pressures are then effectively being redistributed. This effect only occurs in flexible walls, not in stiff walls (Knappett and Craig, 2012).

The pore water pressure distribution around the wall is affected by the water table levels. It can be neglected if the water table level is the same on both sides of the wall. If instead the levels are not the same, which is the case of a dry excavation, there will be an imbalance of the distribution on the two sides (Knappett and Craig, 2012).

2.1.3 Soft clay behavior

Soft clays exhibit low shear strength, are highly compressible, and have high natural moisture content and porosity. This makes soft soil highly susceptible to ground movements. This type of soil is commonly found in coastal areas (Wang et al., 2024). Sensitive clay deposits reaching depths of 100 m can be found in the central parts of Gothenburg which is situated in the Göta River valley where the geology is dominated by glacial and post-glacial clay formed during the Late Pleistocene period (Tornborg et al., 2021).

Most natural soils are also anisotropic, having different characteristic properties in different directions, because of its non-homogeneous constituents and stress history. There can also be a certain degree of interparticle bonding, this is influenced by the mineral and pore water composition. The bonding provide the soils with additional strength and resistance to yielding, but will degrade by plastic straining due to rearrangement of the soil particles. This process is known as destructuration (Karstunen et al., 2005).

2.1.4 Consolidation and creep

The effective stress response from an increase in vertical stress such as surcharge loading results in vertical and horizontal deformation and gradual volume reduction due to the flow of water from the pores causing rearrangement of the soil particles, this phenomenon is known as consolidation. Upon loading, the excess pore water pressure produced is equal to the increase in total vertical stress and no additional stress is transmitted by the soil particles. If the soil is laterally confined, the effective stress therefore remain unchanged as the water is not allowed to dissipate. This is referred to as undrained conditions (Knappett and Craig, 2012).

The buildup of excess pore water pressure creates a hydraulic gradient which allow water seepage to occur until hydrostatic conditions are achieved. This is referred to as drained conditions and the effective stress will gradually increase as more stress is transmitted by the soil skeleton and consolidation progresses (Knappett and Craig, 2012). Even when hydrostatic conditions have been reached, the soil can continue to deform while maintaining the same effective stresses. This phenomenon, known as creep occurs, at a much slower pace, during longer time spans (Sällfors, 2013).

For excavations or other cases where unloading of the soil occurs, the pore water pressure will decrease due to gradual increase in soil volume as the soil particles rearrange. The process can be described as the opposite of consolidation. Negative pore water pressure can in saturated clays result in upward displacement known as heave (Knappett and Craig, 2012).

2.2 Field and laboratory investigation equipment

Multiple in-situ tests and laboratory testing methods were used during the planning and construction process for Hotel Draken. The results from these investigations are the basis for the subsequent site characterization. The following section aims to explain the theory behind the equipment used to carry out these investigations and their use case.

2.2.1 Cone penetration test (CPT) and CPTU

The cone penetration test (CPT), combined with pore pressure measurements, can be used to measure the stratigraphy and identify soil layers. It can also be used to determine geotechnical parameters for the materials present in the ground. To perform a CPTU, a Cone Penetrometer, which is a cylinder with a tip shaped as a cone, is pushed into the ground at a constant rate. The shearing resistance, cone tip resistance and pore pressures are measured, cone resistance and sleeve friction shall be corrected by for pore pressure effects using u_2 in Figure 2.3. These values are then used to identify the stratigraphy. The geotechnical parameters that are often derived based on the CPTU data are the undrained shear strength, the lateral earth pressure at rest and the Over-Consolidation Ratio (OCR) for fine-grained soils. For coarse-grained soils the effective friction angle and relative density can be derived instead. (Knappett and Craig, 2012).

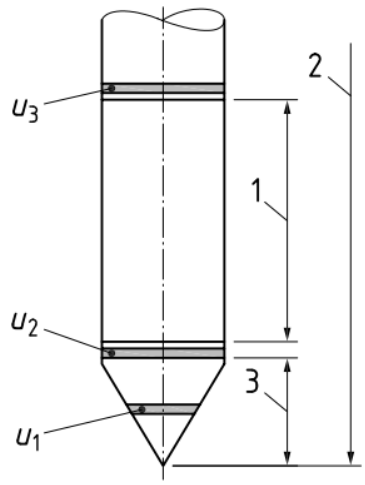

Figure 2.3: Cone configuration SS-EN ISO 22476-1:2023

2.2.2 Soil-rock sounding

Soil-rock sounding (Jord-bergsondering in Swedish) is a method used to identify boulders, measure the soil stratification, and to find how deep down the bedrock is. The method is performed by penetrating the soil with a hydraulic percussion drill, measuring torque, speed of penetration and depth among other things. What makes soil-rock sounding unique is that it can penetrate boulders and bedrock. However, it's ability to measure soil parameters is limited, so other methods are preferred for that (Ehrmantraut et al., 2021).

2.2.3 Piston sampling

Piston sampling (kolvprovtagning) is a method used to take undisturbed samples that can be analyzed in a laboratory. This method makes sure the that the properties of the soil samples are the same as they were at the depth of the site they were taken at (SGF, 2009).

2.2.4 Groundwater observations and Piezometers

In coarse, permeable soils, the level of the water table can be determined by measurements of the ground water surface in an open bore hole or well. The water level observed then represents the piezometric surface. For less permeable soils such as clays, a closed system piezometer can be used when determining the in-situ pore water pressure of a particular stratum (Sällfors, 2013).

2.2.5 Direct shear test

Direct simple shear tests can be used for determining both stiffness and strength parameters for soils. It measures the drained strength of the soil at failure by shearing the test horizontally while loading it vertically. The sample is consolidated under vertical force N through a loading plate with an area A, without knowledge of the effective horizontal stress state, and a horizontal force T cause the two halves of the shear box to slip while measuring the shear displacement. The shear strain and volumetric strain can then be approximated. The test must be done very slowly so that water can dissipate and the excess pore water pressure is negligible. The vertical total stress is then equal to the effective stress ($\sigma'_f = N/A$). The shear stress at failure ($\tau_f = T/A$) can then be plotted against effective stress for each test to determine the effective strength parameters (c' and φ') (Knappett and Craig, 2012).

2.2.6 Triaxial test

The behavior of soils in shear can also be measured in triaxial tests. The triaxial apparatus allow for testing of both drained and undrained conditions in compression and extension. Load is applied as a confining fluid pressure both axially and radially and axially through loading via a piston (deviatoric stress). The testing procedure can be divided into four parts: Preparation of the soil specimen, consolidation (for CU and CD tests only), shearing, and interpretation of the test data. The drainage condition during the consolidation step allows the water to drain. The consolidation stage can be anisotropic (recommended) or isotropic (often done by local tradition). The control of drainage during the shearing step enables either undrained or drained shearing. The three types of triaxial tests used for soil characterization are unconsolidated undrained (UU), consolidated undrained (CU) and consolidated drained (CD) (Knappett and Craig, 2012).

A triaxial cell holds the cylindrical soil specimen, commonly having a length/diameter ratio of 2. Solid or porous discs are placed on the top and the bottom, and the sample is sealed with a thin and flexible rubber membrane to separate the soil from the cell fluid. Through the discs at the top and the bottom, excess pore water pressure can dissipate via drainage hoses connected to an external water volume gauge. This applies for consolidation and drained shearing. Closing the drainage hoses prevents the flow of pore water, allowing for measurement of the excess pore water pressure. This applies to unconsolidated tests and undrained shearing (Knappett and Craig, 2012).

In the consolidation step the soil sample is normally stressed to the prevailing axial and radial stress state in-situ either isotropically or anisotropically. For consolidated tests the sample is allowed to drain the excess pore water, for unconsolidated tests the drainage hoses are now closed. The applied radial load is controlled by the coefficient of earth pressure at rest (K_0) with the confining water pressure (Knappett and Craig, 2012).

Shearing is the step in which gradual deviatoric stress is applied (either increased or decreased) under displacment control to the sample axially until failure. In active shearing, also known as triaxial compression tests, the sample is gradually stressed in axial compression while the confining water pressure is kept constant. For passive shearing or triaxial extension tests, the confining water pressure is also kept constant. However, the axial stress is gradually decreased (Knappett and Craig, 2012).

2.2.7 Oedometer

Oedometer tests are used for determining the characteristics of a soil during one-dimensional consolidation or swelling with zero lateral strain. The cylindrical sample sits within the oedometer apparatus between two porous stones, and is laterally confined by a smooth polished ring for minimum vertical friction (Knappett and Craig, 2012).

Tests can either be incrementally loaded in steps (IL) or subjected to a constant rate of strain (CRS). For IL tests, the initial load applied vary depending on the soil type. Each loading increment being double that of the previous increment and normally maintained for 24 hours (Knappett and Craig, 2012).

For CRS tests, the soil specimen is compressed at a constant rate of displacement. The constant displacement rate is normally 0.0025 mm/min, such that 18% strain can be obtained in 24 h. For soft clays however, the rate should be lower, so that the measured pore water pressure do not exceed 10% of the total stress. The result of the CRS test provide a relationship between stress, strain and pore water pressure for the soil (Svenska Institutet för Standarder, 1991).

2.3 Numerical modelling

The behavior of complex systems, such as complex geometries and nonlinear behavior, can be impossible to solve analytically. Numerical modelling provides a solution to these problems at system level. Numerical modelling is the process of using computational algorithms to solve mathematical equations that describe physical systems. Instead of finding an exact solution, a solution is approximated (Potts, 1999; Wood, 2004).

The finite element method is a commonly used numerical method. In this method, the geometry is sectioned into finite elements that together form a finite element mesh. The geometry of these elements is described by nodes, with more curved elements needing more nodes than straight ones. The shape of these elements depends on if the modelling is done in 2D or 3D (Potts, 1999) and the desired accuracy.

2.3.1 Equilibrium and compatibility

The self weight of the soil (γ) combined with any loads applied on the soil results in a normal stress in the vertical and horizontal directions (σ). The stress in the horizontal direction can also cause shear stress (τ). The equations of equilibrium (Eqation 2.4) state that the sum of forces in any direction must be zero (Knappett and Craig, 2012).

$$
\begin{cases}
\frac{\partial \sigma_x}{\partial x} + \frac{\partial \tau_{yx}}{\partial y} + \frac{\partial \tau_{zx}}{\partial z} + \gamma = 0 \\
\frac{\partial \tau_{xy}}{\partial x} + \frac{\partial \sigma_y}{\partial y} + \frac{\partial \tau_{zy}}{\partial z} = 0 \\
\frac{\partial \tau_{xz}}{\partial x} + \frac{\partial \tau_{yz}}{\partial y} + \frac{\partial \sigma_z}{\partial z} = 0
\end{cases}
\tag{2.4}
$$

When a soil experiences loading there will also be straining of the soil mass, meaning that points of the soil will be displaced (u, v, w) relative to their original position. The equation of compatibility (Equation 2.5) states that the strains in the x-, y- and z- directions cannot be independent of each other, so that the soil mass will be continuous (Knappett and Craig, 2012).

$$
\begin{cases}
\varepsilon_x = -\frac{\partial u}{\partial x} \\
\varepsilon_y = -\frac{\partial v}{\partial y} \\
\varepsilon_z = -\frac{\partial w}{\partial z} \\
\tau_{xy} = -\frac{\partial v}{\partial x} - \frac{\partial u}{\partial y} \\
\tau_{yz} = -\frac{\partial w}{\partial y} - \frac{\partial v}{\partial z} \\
\tau_{xz} = -\frac{\partial w}{\partial x} - \frac{\partial u}{\partial z}
\end{cases}
\tag{2.5}
$$

2.3.2 Constitutive models

By combining the conditions of equilibrium and compatibility 15 unknowns are obtained, but only 9 equations. A solution requires 6 additional equations, which comes from a constitutive model (Potts, 1999). Constitutive models are used to describe how a material, for example soil, will behave when subjected to different loading conditions, by defining the stress-strain relationship of the material (Zhang et al., 2017).

The type of soil deformation that can be recovered is called elastic, and the type of deformation that cannot be recovered is plastic (or visco-plastic). The constitutive model for an elasto-plastic material can be obtained by formulating a relationship between both the elastic and plastic strains to the stresses (Equation 2.6). The constitutive matrix $[D^{ep}]$ represent both elastic and plastic behaviour for the relationship between the total incremental strains $(\Delta\varepsilon)$ and the total incremental stresses $(\Delta\sigma)$ (Potts, 1999).

$$
\{\Delta\sigma\} = [D^{ep}]\{\Delta\varepsilon\}
\tag{2.6}
$$

2.3.3 Linear elastic models

Solving a particular problem can be very difficult because of the aforementioned mechanics of soil. To make calculation easier, the stress-strain relationship can be simplified. The elastic-perfectly plastic model (Eqation 2.7) is an idealization, which assumes Hooke's Law, linearly elastic behavior, up until a certain point at which plastic strain occurs at a constant stress (Knappett and Craig, 2012).

$$\begin{Bmatrix} \Delta\sigma'_x \\ \Delta\sigma'_y \\ \Delta\sigma'_z \\ \Delta\tau_{xz} \\ \Delta\tau_{yz} \\ \Delta\tau_{xy} \end{Bmatrix} = \begin{bmatrix} K'+4/3G & K'-2/3G & K'-2/3G & 0 & 0 & 0 \\ 0 & K'-4/3G & K'-2/3G & 0 & 0 & 0 \\ 0 & 0 & K'-4/3G & 0 & 0 & 0 \\ 0 & 0 & 0 & G & 0 & 0 \\ 0 & 0 & 0 & 0 & G & 0 \\ 0 & 0 & 0 & 0 & 0 & G \end{bmatrix} \begin{Bmatrix} \Delta\varepsilon_x \\ \Delta\varepsilon_y \\ \Delta\varepsilon_z \\ \Delta\gamma_{xz} \\ \Delta\gamma_{yz} \\ \Delta\gamma_{xy} \end{Bmatrix} \tag{2.7}$$

Here G is the shear modulus and K' is the bulk modulus of a linear elastic material. This can be written more compactly as in Equation 2.8, where the $[D]$ matrix is used for the purely elastic behavior such as Hooke's law, and $\Delta\varepsilon^e$ is the incremental elastic strains.

$$\{\Delta\sigma\} = [D]\{\Delta\varepsilon^e\} \tag{2.8}$$

2.3.4 Yield Criterion

The yield surface is the boundary between the elastic and plastic deformation (Karstunen and Amavasai, 2017). The yield surface is defined as a function of the stress state $\{\sigma\}$ and the potential hardening or softening, known as state parameters $\{\mathbf{k}\}$ (Equation 2.9). The plastic state is reached when the stress state is on the yield surface. For $f < 0$ purely elastic behavior occur, for $f = 0$ elasto-plastic (or visco-plastic) behavior occur. For perfect plasticity the yield surface is independent of strain so $\{\mathbf{k}\}$ is constant. Examples of this are the Mohr-Coulomb and Tresca failure criteria. Incorporating strain hardening or softening implies that the yield surface change in magnitude with plastic straining so that $\{\mathbf{k}\}$ varies (Potts, 1999).

$$f(\{\sigma\}, \{\mathbf{k}\}) = 0 \tag{2.9}$$

When formulating a constitutive model it is more convenient to describe the general stress state in terms of stress invariants. By doing so, it is no longer necessary to determine the major and minor principal stresses for a certain stress state. The stress invariants are the mean effective stress p', the deviatoric stress J and Lode's angle θ. Different modified versions of these parameters are often used when describing constitutive models. The Tresca yield criterion adopting the stress invariants is shown in Equation 2.10, assuming perfectly plastic behavior (i.e. no plastic volumetric strain). The state parameter $\{\mathbf{k}\} = s_u$ representing the shear strength is therefore constant and independent of hardening or softening (Potts, 1999).

$$f(\{\sigma\}, \{\mathbf{k}\}) = \sigma_1 - \sigma_3 - 2s_u = Jcos\theta - s_u = 0 \tag{2.10}$$

2.3.5 Hardening and softening

To simulate a case where the plastic strain causes an increase in stress, making the soil harder during straining, the elastic-strain hardening plastic model is used. This model creates a new yield point at the stress level that the soil is unloaded and reloaded at (Knappett and Craig, 2012). Incorporating this into the Tresca yield criterion will result in the formulation of the yield criterion for the NGI-ADP model, which is introduced later in Section 2.3.9. There are also the elastic-strain softening plastic model, where the plastic strain results in a decrease in stress (Knappett and Craig, 2012). This causes the yield surface to shrink, for example because of dilation (Lees, 2016).

$$f(\{\sigma\}, \{\mathbf{k}\}) = Jcos\theta - \mathbf{k}s_u = 0 \tag{2.11}$$

2.3.6 Plastic potential function and flow rule

So far only the elastic strains have been considered, but the total incremental strains ($\Delta\varepsilon$) are the sum of both elastic ($\Delta\varepsilon^e$) and plastic (or visco-plastic) ($\Delta\varepsilon^p$) strains (Equation 2.12). By Combining Equations 2.12 and 2.8 it is now possible to obtain a relation between the plastic strains and the total stresses in Equation 2.13.

$$\{\Delta\varepsilon\} = \{\Delta\varepsilon^e\} + \{\Delta\varepsilon^p\} \tag{2.12}$$

$$\{\Delta\sigma\} = [D](\{\Delta\varepsilon\} - \{\Delta\varepsilon^p\}) \tag{2.13}$$

To represent the straining at every stress state it is also necessary to define the direction of strains. The flow rule defines the direction of plastic (or visco-plastic) strain increments during yielding (Equation 2.14). Where $\{\mathbf{m}\}$ is a vector of immaterial state parameters and Λ is a scalar plastic multiplier that defines the magnitude of the trains. The flow rule can be divided into the associated flow rule and the non-associated flow rule. The associated flow rule states that the plastic potential function is the same as the yield function, meaning that the plastic strain occurs in the same direction as the normal of the yield surface (Equation 2.15) (Potts, 1999).

$$\Delta\varepsilon_i^p = \Lambda \frac{\partial g(\{\sigma\}, \{\mathbf{m}\})}{\partial \sigma_i} \tag{2.14}$$

$$g(\{\sigma\}, \{\mathbf{m}\}) = f(\{\sigma\}, \{\mathbf{k}\}) \tag{2.15}$$

This is in general not suitable for soil when simple models are adopted, because it will lead to a very high prediction of the rates of dilation. This is because the dilation angle and the friction angle are assumed the same. If however a soil with a low friction angle is modelled, then the associated flow rule can be used. The non-associated flow rule (Equation 2.16) assumes that yield and plastic functions are different from each other. This avoids the problem with the dilation angle being too large, but makes the calculations more complex (Lees, 2016) (Potts, 1999).

$$g(\{\sigma\}, \{\mathbf{m}\}) \neq f(\{\sigma\}, \{\mathbf{k}\}) \tag{2.16}$$

2.3.7 Choice of model

The choice of which constitutive model needs to be considered carefully, since it will affect the accuracy of the analysis. The material that governs the failure probability and deformations is usually the soil, because it is softer and weaker than construction materials like steel and concrete. This makes the choice of constitutive model very vital.

The type of soil and rock that is present at the site is an important consideration to make. For example, certain soils are more anisotropic than others. However, this does not mean that the same constitutive model will be suitable for all types of projects where the same soil type is present. This is because different projects can require different outputs, and not all constitutive models provide the same outputs (Lees, 2016).

2.3.8 Formulation of the Mohr-Coulomb model

The Mohr-Coulomb model is a linear elastic perfectly plastic model based on Hooke's law of isotropic elasticity and the Mohr-Coulomb failure criterion assuming perfect plasticity. The yield condition consists of six yield functions (Equation 2.17), forming a hexagonal cone in the principal stress space. If the friction angle is set to zero the model reduces to the Tresca yield criterion, $c' = s_u$. Since the Mohr-Coulomb criterion allows for tensile strength, the addition of tension cut-off yield criteria restrict this often unwanted behavior.

To account for dilatancy, the model use a non-associated flow rule by introducing separate plastic potential functions. The six plastic potential functions in Equation 2.18 are required in order to model the plastic volumetric strains.

$$\begin{Bmatrix} f_{1a} \\ f_{1b} \\ f_{2a} \\ f_{2b} \\ f_{3a} \\ f_{3b} \end{Bmatrix} = \frac{1}{2} \begin{bmatrix} (\sigma'_2 - \sigma'_3) + (\sigma'_2 + \sigma'_3)\sin(\phi') - 2c'\cos(\phi') \\ (\sigma'_3 - \sigma'_2) + (\sigma'_3 + \sigma'_2)\sin(\phi') - 2c'\cos(\phi') \\ (\sigma'_3 - \sigma'_1) + (\sigma'_3 + \sigma'_1)\sin(\phi') - 2c'\cos(\phi') \\ (\sigma'_1 - \sigma'_3) + (\sigma'_1 + \sigma'_3)\sin(\phi') - 2c'\cos(\phi') \\ (\sigma'_1 - \sigma'_2) + (\sigma'_1 + \sigma'_2)\sin(\phi') - 2c'\cos(\phi') \\ (\sigma'_2 - \sigma'_1) + (\sigma'_2 + \sigma'_1)\sin(\phi') - 2c'\cos(\phi') \end{bmatrix} \tag{2.17}$$

$$\begin{Bmatrix} g_{1a} \\ g_{1b} \\ g_{2a} \\ g_{2b} \\ g_{3a} \\ g_{3b} \end{Bmatrix} = \frac{1}{2} \begin{bmatrix} (\sigma'_2 - \sigma'_3) + (\sigma'_2 + \sigma'_3)\sin(\psi) \\ (\sigma'_3 - \sigma'_2) + (\sigma'_3 + \sigma'_2)\sin(\psi) \\ (\sigma'_3 - \sigma'_1) + (\sigma'_3 + \sigma'_1)\sin(\psi) \\ (\sigma'_1 - \sigma'_3) + (\sigma'_1 + \sigma'_3)\sin(\psi) \\ (\sigma'_1 - \sigma'_2) + (\sigma'_1 + \sigma'_2)\sin(\psi) \\ (\sigma'_2 - \sigma'_1) + (\sigma'_2 + \sigma'_1)\sin(\psi) \end{bmatrix} \tag{2.18}$$

Table 2.1: Input parameters for the Mohr-Coulomb model.

Parameter	Description	Unit	Determination
E'_{ref}	Young's modulus	kN/m^2	Drainend triaxial test
ν'	Poisson's ratio	-	Drainend triaxial test
G	Shear modulus	kN/m^2	$\frac{E}{2(1+\nu)}$
E_{oed}	Oedometer modulus	kN/m^2	$\frac{E(1+\nu')}{(1-2\nu')(1+\nu')}$
c'	Cohesion	kN/m^2	Triaxial compression test
φ'	Friction angle	$^\circ$	Triaxial compression test
ψ	Dilatancy angle	$^\circ$	$\varphi' - 30^\circ$
σ_t	Tension cut-off and tensile strength	kN/m^2	Use specific

2.3.9 Formulation of the NGI-ADP model

NGI-ADP is an elastoplastic constitutive model that is developed specifically for clay to model undrained behavior, which often exhibit an anisotropic stress-strain-strength response and non-linear stress-strain behavior (hardening). The model takes the anisotropic behavior of clay into account by directly inputting different shear strengths based on triaxial compression, triaxial extension, and direct simple shear test. This distinguishes NGI-ADP from other constitutive models used for anisotropic behavior, in which the undrained shear strength is indirectly emerging based on several soil parameters. The model uses method C described in Section 2.3.17, meaning that it is a total stress method which can be used for determining the undrained response of clays (Grimstad et al., 2012) in situations when the short-term response is of interest.

The general stress state is defined in terms of a modified deviatoric stress vector (Equation 2.19), considering both undrained shear strength in compression (s_u^A), extension (s_u^p) and direct shear (s_u^{DSS}) as well as the hardening function, which is dependent on the plastic shear strain in compression , extension and direct shear.

$$\begin{Bmatrix} \hat{s}_{xx} \\ \hat{s}_{yy} \\ \hat{s}_{zz} \\ \hat{s}_{xy} \\ \hat{s}_{xz} \\ \hat{s}_{yz} \end{Bmatrix} = \begin{bmatrix} \sigma'_{xx} - \sigma'_{xx_0}(1-\kappa) + \kappa\frac{1}{3}(s_u^A - s_u^P) - \hat{p} \\ \sigma'_{yy} - \sigma'_{yy_0}(1-\kappa) + \kappa\frac{2}{3}(s_u^A - s_u^P) - \hat{p} \\ \sigma'_{zz} - \sigma'_{zz_0}(1-\kappa) + \kappa\frac{1}{3}(s_u^A - s_u^P) - \hat{p} \\ \tau_{xy}\frac{s_u^A + s_u^P}{2s_u^{DSS}} \\ \tau_{xz} \\ \tau_{yz}\frac{s_u^A + s_u^P}{2s_u^{DSS}} \end{bmatrix} \tag{2.19}$$

Where $\sigma'_{xx_0}, \sigma'_{yy_0}, \sigma'_{zz_0}$ are the initial stresses and $\hat{p}$ is the modified mean stress defined as:

$$\hat{p} = \frac{(\sigma'_{xx} - \sigma'_{xx_0}(1-\kappa)) + (\sigma'_{yy} - \sigma'_{yy_0}(1-\kappa)) + (\sigma'_{zz} - \sigma'_{zz_0}(1-\kappa))}{3} \tag{2.20}$$

The hardening function κ is given by Equation 2.21 for the plastic strain $\gamma^p <$ the failure (peak) shear strength γ_f^p.

$$\kappa = 2\frac{\sqrt{\gamma^p/\gamma_f^p}}{1+\gamma^p/\gamma_f^p} \tag{2.21}$$

The yield surface of the NGI-ADP model (Equation 2.22) is based on the Tresca yield criterion. One problem with the Tresca Yield criterion criterion is that numerical difficulties can arise as a result of the sharp corners of the inherent yield surface. The NGI-ADP model avoids this problem by creating a smooth yield surface instead. The approximation of the Tresca yield criterion is defined according to Equation 2.23, where $a_1 = 1.0$ is the exact solutions. By letting $a_1 = 0.99$, smoother corners can be obtained (Grimstad et al., 2012).

$$f = \sqrt{H(\omega)\hat{J}_2} - \kappa\frac{s_u^A + s_u^P}{2} = 0 \tag{2.22}$$

$$H(\omega) = cos^2\left(\frac{1}{6}arccos(1 - 2a_1\omega)\right) \tag{2.23}$$

$$\omega = \frac{27}{4}\frac{\hat{J}_3^2}{\hat{J}_2^3} \tag{2.24}$$

The modified second and third deviatoric invariants $\hat{J}_2$ and $\hat{J}_3$ are defined in Equation 2.25 and Equation 2.26 respectively.

$$\hat{J}_2 = -\hat{s}_{xx}\hat{s}_{yy} - \hat{s}_{xx}\hat{s}_{zz} - \hat{s}_{yy}\hat{s}_{zz} + \hat{s}_{xz}^2 + \hat{s}_{xz}^2 + \hat{s}_{yz}^2 \tag{2.25}$$

$$\hat{J}_3 = \hat{s}_{xx}\hat{s}_{yy}\hat{s}_{zz} + 2\hat{s}_{xy}\hat{s}_{yz}\hat{s}_{xz} - \hat{s}_{xx}\hat{s}_{yz}^2 - \hat{s}_{yy}\hat{s}_{xz}^2 - \hat{s}_{zz}\hat{s}_{xy}^2 \tag{2.26}$$

NGI-APD uses a non-associated flow rule to specify the direction of the plastic strain. The plastic potential function is shown in Equation 2.27, where $\hat{I}$ is a modified unit vector (Grimstad et al., 2012).

$$\frac{\partial g}{\partial \sigma'} = \frac{1}{2}\left(\hat{I} + \frac{\partial p}{\partial \sigma'}\left(\frac{\partial \hat{s}}{\partial \hat{p}}\right)^T\right)\frac{\partial \hat{J}_2}{\partial \hat{s}}\sqrt{\frac{1}{\hat{J}_2}} \tag{2.27}$$

Table 2.2: Input parameters for NGI-ADP.

Parameter	Description	Unit	Determination
γ_f^C	Shear strain at failure in triaxial compression	%	Triaxial compression test at peak strength
γ_f^E	Shear strain at failure in triaxial extension	%	Triaxial extension test at peak strength
γ_f^{DSS}	Shear strain in direct simple shear	%	Direct simple shear test at peak strength
$s_{u,ref}^A$	Reference plane strain active shear strength	kN/m^2	Triaxial compression test at peak strength
y_{ref}	Reference depth	m	At depth of triaxial compression test
$s_{u,inc}^A$	Increase of shear strength with depth	kN/m^2/m	Trend for triaxial compression test at peak strength
s_u^P/s_u^A	Ratio of plane strain passive shear strength over (plane strain) active shear strength	-	Triaxial extension and compression tests at peak strength
τ_0/s_u^A	Initial mobilization	-	$\frac{0.5(\sigma'_{v0}-\sigma'_{h0})}{s_u^A}$
s_u^{DSS}/s_u^A	Ratio of direct simple shear strength over (plane strain) active shear strength	-	Direct simple shear and triaxial compression test at peak strength
G_{ur}/s_u^A	Ratio unloading/reloading shear modulus over (plane strain) active shear strength	-	Oedometer test with unloading/reloading and triaxial compression test at peak strength

2.3.10 Formulation of the Creep-SCLAY1S model

The Creep-SCLAY1S model is an advanced rate dependent (differentiation w.r.t time) model, a visco-plastic model, designed to simulate normally- to slightly overconsolidated soft clays. It considers anisotropy, the evolution of anisotropy due to irrecoverable strains, destructuration due to the degradation of bonds in soft sensitive clays and creep (Amavasai et al., 2018) (Sivasithamparam et al., 2015).

Natural clays often exhibit both elastic and visco-plastic anisotropy due to sedimentation and consolidation. However, as the visco-plastic strains in most loading cases are significantly higher than the elastic strains, the anisotropy of the elastic strains can be neglected and assumed isotropic as well as non-linear. Furthermore, it is assumed that no purely elastic region exist and viscoplastic (creep) deformations occur at all stress levels (Sivasithamparam et al., 2015).

The mathematical formulation of the model can be represented in triaxial stress space and in terms of stress quantities, mean effective stress $p' = (\sigma'_1 + 2\sigma'_3)/3$, deviatoric stress $q = (\sigma'_1 - \sigma'_3)$ and strain quantities, volumetric strain $\varepsilon_v = (\varepsilon_1 + 2\varepsilon_3)$, deviatoric strain $\varepsilon_q = (\varepsilon_1 - \varepsilon_3)$. The total volumetric and deviatoric strain rates are defined as the sum of the elastic and creep strain rates in Equation 2.28. The superscript e and c refers to the elastic and viscoplastic strain component respectively and the subscript v and q to the volumetric and deviatoric component respectively.

The volumetric and deviatoric elastic rate of strain components are related to the stresses as shown in Equation 2.29 and Equation 2.30, where the elastic bulk modulus $K' = p'/\kappa^*$, the elastic shear modulus $G = 3p'/2\kappa^*(1 - 2\nu'/1 + \nu')$ and ν' is Poisson's ratio (Sivasithamparam et al., 2015).

$$\begin{cases} \dot{\varepsilon}_v = \dot{\varepsilon}^e_v + \dot{\varepsilon}^c_v \\ \dot{\varepsilon}_q = \dot{\varepsilon}^e_q + \dot{\varepsilon}^c_q \end{cases} \tag{2.28}$$

$$\dot{\varepsilon}^e_v = \frac{\dot{p}'}{K'} \tag{2.29}$$

$$\dot{\varepsilon}^e_q = \frac{\dot{q}}{3G} \tag{2.30}$$

Three separate surfaces and subsequently three separate hardening laws that relates to the volumetric hardening, the evolution of anisotropy and destruction are defined for the Creep-SCLAY1S model (Tornborg et al., 2021). All three surfaces have a similar shape and orientation which can be expressed according to Equation 2.31 (Amavasai et al., 2018). p'_s can be substituted for p'_{mi}, p'_{eq} or p'_m to describe the sizes of the Intrinsic Compression Surface (ICS), the Current Stress Surface (CSS) and the Normal Consolidation Surface (NCS) respectively, shown in Figure 2.4.

$$p'_s = p' + \frac{(q - \alpha p')^2}{(M(\theta_\alpha)^2 - \alpha^2)p'} \tag{2.31}$$

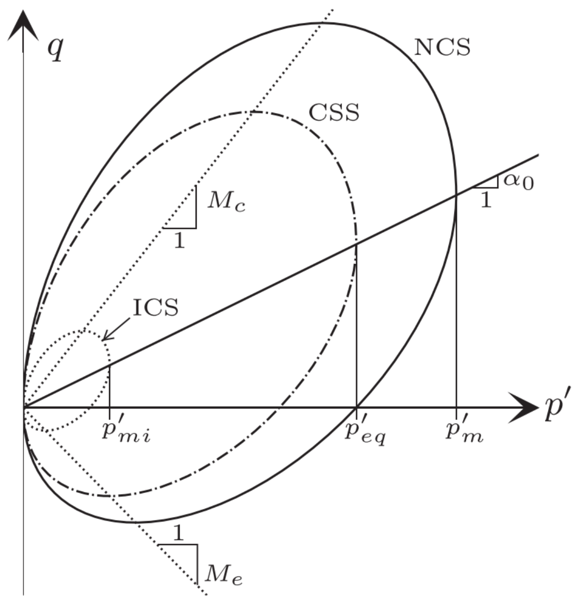

Figure 2.4: Illustration of the intrinsic (ICS), current stress (CSS) and normal compression (NCS) yield surfaces for the Creep-SCLAY1S model (Tornborg et al., 2021).

$M(\theta_\alpha)$ is the modified Lode angle which determines the stress ratio at critical state. This controls the slope of the critical state lines M_c and M_e shown in Figure 2.4.

The imaginary ICS, defined by the intrinsic preconsolidation pressure p'_{mi}, is the smallest ellipse in Figure 2.4. Its size evolves with the volumetric creep strains, controlled with the first hardening law in Equation 2.32. λ_i^* is the modified intrinsic compression index and κ^* the modified swelling index, explained further in Section 3.3.7. Subscript i refers to the intrinsic material property, where a complete loss of structure has occurred (Amavasai et al., 2018).

$$dp'_{mi} = \frac{p'_{mi}}{\lambda_i^* - \kappa^*} d\varepsilon_v^c \tag{2.32}$$

The intermediate ellipse in Figure 2.4 CSS represents the current effective stress state. In triaxial space α is a scalar state variable relating to the orientation of the yield surface, i.e. the evolution of anisotropy controlled by the second hardening law in Equation 2.33. Where the stress ratio $\eta = q/p'$, with ω and ω_d being model constants related to the effectiveness of the rotational hardening (Amavasai et al., 2018). In generalissed 3D version of the model, as implement in Plaxis, α is replaced with a fabric tensor.

$$d\alpha = \omega \left[\left(\frac{3\eta}{4} - \alpha \right) \langle d\varepsilon_v^c \rangle + \omega_d \left(\frac{\eta}{3} - \alpha \right) |d\varepsilon_q^c| \right] \tag{2.33}$$

The NCS is the outer sheared ellipse shown in Figure 2.4, defining the boundary between small and large creep strains. The size of the NCS is defined by the effective preconsolidation pressure p'_m and is related to the size of the ICS in Equation 2.34 with a state variable χ, representing the current amount of bonding in the soil. The degradation of bonding (destructuration) is controlled by the third hardening law in Equation

2.35, where ξ and ξ_d are related to the rate of destructuration. Thus, ICS allows to model for the effects of structural degradation of the soil by linking its size to the size of NCS.

$$p'_m = p'_{mi}(1-\chi) \tag{2.34}$$

$$d\chi = -\xi\chi\left[|d\varepsilon_v^c| + \xi_d|d\varepsilon_q^c|\right] \tag{2.35}$$

An associated flow rule is assumed, which means that the plastic (or viscoplastic) strain are assumed to occur in the same direction as the normal to NCS. However, this is combined with the evolution of anisotropy and thus, the possibility of an inclined yield surface (Amavasai et al., 2018). The flow rule is shown in Equation 2.36,

$$\begin{cases} \dot{\varepsilon}_v^c = \dot{\Lambda}\frac{\partial p'_{eq}}{\partial p'} \\ \dot{\varepsilon}_q^c = \dot{\Lambda}\frac{\partial p'_{eq}}{\partial q'} \end{cases} \tag{2.36}$$

where $\dot{\Lambda}$ is the (rate-dependent) viscoplastic multiplier defined in Equation 2.37. Subscript K_0^{NC} for α and η refers to the the inclination of the yield surface in the normally consolidated state and the stress ratio corresponding K_0 condition, respectively. The intrinsic modified creep index μ_i^* represents a state where the structure of the soil is completely erased, at large stresses. τ is the reference time of the loading in a 1D compression test (Amavasai et al., 2018).

$$\dot{\Lambda} = \frac{\mu_i^*}{\tau}\left(\frac{p'_{eq}}{(1+\chi)p'_{mi}}\right)^{\frac{\lambda_i^*-\kappa^*}{\mu_i^*}}\left(\frac{M_c^2-\alpha^2_{K_0^{NC}}}{M_c^2-\eta^2_{K_0^{NC}}}\right) \tag{2.37}$$

Table 2.3: Input parameters for Creep-SCLAY1S.

Parameter	Description	Unit	Determination
e_0	Initial void ratio	-	Based on water content and specific gravity
POP	Pre-overburden pressure	-	Oedometer IL test
OCR	Overconsolidation ratio	-	Oedometer IL test
α_0	Initial anisotropy	-	$\frac{(\eta_{K_0}^2+3\eta_{K_0}-M_c^2)}{3}$
χ_0	Initial amount of bonding	-	Oedometer IL or CRS test
λ_i^*	Modified intrinsic compression index	-	Oedometer IL or CRS test
κ^*	Modified swelling index	-	Oedometer IL or CRS test
ν'	Poisson's ratio	-	Triaxial test
μ_i^*	Modified intrinsic creep index	-	Oedometer IL test with fixed load duration
τ	Reference time	day	Time step employed in Oedometer IL test
M_c	Slope of critical state line in compression	-	Triaxial compression test CAUC
M_e	Slope of critical state lin in extension	-	Triaxial extension test CAUE
ω	Absolute effectiveness of rotational hardening	-	Triaxial extension test CAUE
ω_d	Relative deviatoric effectiveness of rotational hardening	-	$\frac{3(M_c^2-4\eta_{K_0}^2-3\eta_{K_0})}{8(\eta_{K_0}^2-M_c^2+2\eta_{K_0})}$
ξ	Absolute rate of destructuration	-	Back calculated from CRS and triaxial tests
ξ_d	Relative deviatoric rate of destructuration	-	Back calculated from CRS and triaxial tests
K_0^{NC}	Coefficient of lateral stress in normal consolidation	-	$1 - sin\,\varphi_c'$

2.3.11 Initial stress procedure

When analyzing a geotechnical problem using numerical modelling, the initial stresses need to be generated, and they need to be in equilibrium in order to predict deformations accurately. To correctly predict and generate these initial stresses, different methods can be used. The K_0 procedure utilizes the loading history of the soil, where the vertical stresses generated will be in equilibrium with the weight of the soil. The horizontal stresses, σ_h, are then calculated according to Equation 2.38. However, the K_0 procedure assumes that no shear stresses exist and because of this, equilibrium cannot be achieved for sloped surfaces. This method should therefore only be utilized for situations where all surfaces and soil layers are horizontal. If this is not the case, gravity loading should be used instead (Bentley Systems, 2025d).

$$\sigma_h = K_0 \cdot \sigma_v \tag{2.38}$$

2.3.12 Soil-structure interaction

The interaction between materials that have different properties to each other introduces complexity to the numerical modelling compared to when only one material is considered. The transfer of a load between the soil and a structure is not simple. If the soil is less stiff than the structural member, there will be less deflection of the soil and the structure. However, the bending moment increases because the structure can distribute loads more effectively. When the difference in stiffness decreases, the bending moment will also decrease because the soil will redistribute more stress. There are non-linear relationships between relative stiffness, deflection, and bending moment. Because of the complexity of these interactions, simplifications are sometimes made. For example, if the stiffness of a structure is much higher than for the soil, it can be considered as a linear elastic material (Lees, 2016).

2.3.13 2D modelling of sheet pile walls

In PLAXIS 2D, an isotropic plate requires input of four different parameters, shown in Table 2.4. Since the plates are modelled as a line, an equivalent thickness, d_{eq}, needs to be calculated to properly simulate the behaviour of the sheet pile wall. It is automatically calculated by PLAXIS 2D using Equation 2.39 (Bentley Systems, 2025a). Plates are discretized into beam elements where each node has three degrees of freedom that represent horizontal displacement, vertical displacement, and rotation. The number of nodes that each beam element has is dependent on how many nodes the soil elements have, with 6-node soil elements resulting in three nodes per beam element, and 15-node soil elements resulting in five nodes per beam element. The beams can deform both due to bending and shearing, thanks to the beam elements being based on Mindlin's beam theory.

Table 2.4: Input parameters for an isotropic plate in PLAXIS 2D

Property	Description	Unit
w	Unit weight	kN/m^2
EA	Axial stiffness	kN/m^2
EI	Bending stiffness	kNm^2/m
v	Poisson's ratio	-

$$d_{eq} = \sqrt{\frac{12EI}{EA}} \tag{2.39}$$

The plates also have Gaussian stress points, with a 3-noded plate element having two pairs of stress points and a 5-node plate element having four pairs of stress points. From these stress points the axial forces and bending moments can be calculated. Figure 2.5 shows the position of these nodes and stress points (Bentley Systems, 2025b).

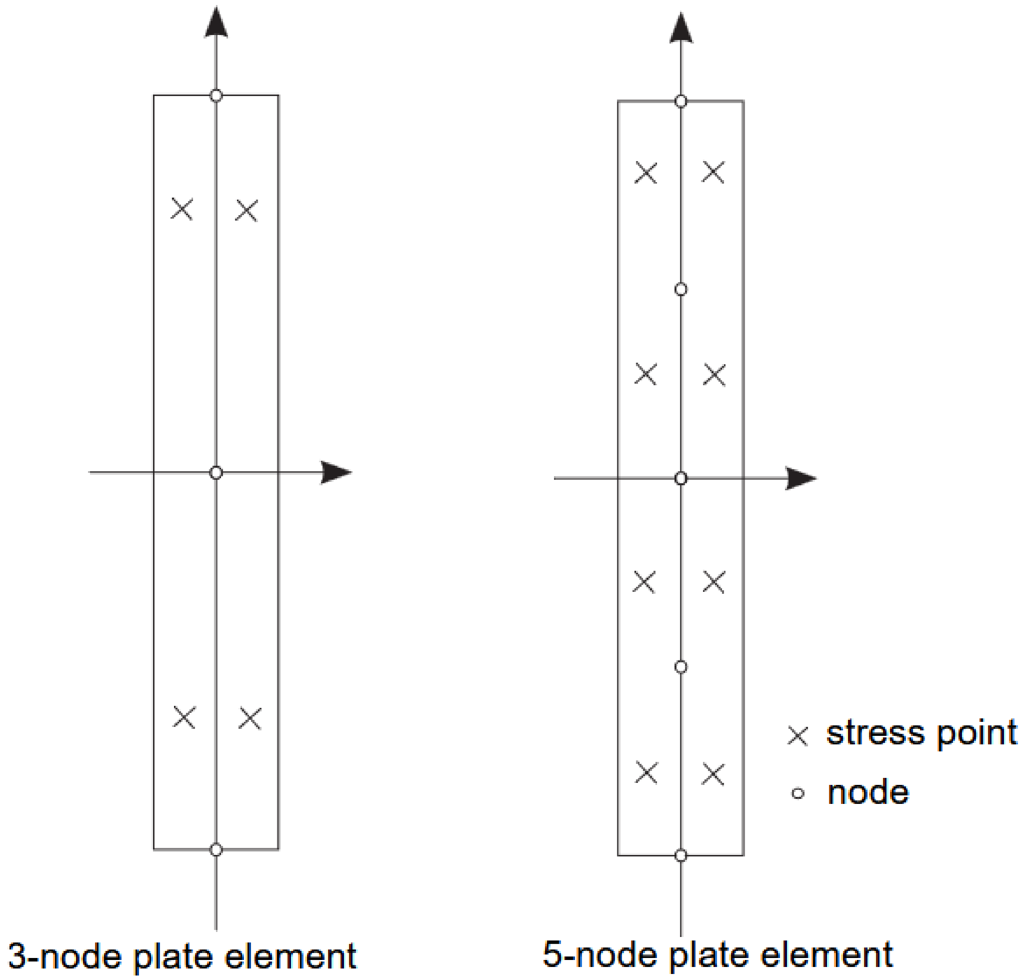

Figure 2.5: Position of nodes and stress points in 2D plate elements (Bentley Systems, 2025b).

To allow for interaction between the sheet pile wall and the soil, interfaces have to be introduced. If no interface is applied, the sheet pile wall will be attached to the soil, and the soil and the wall would share nodes. This would make it impossible for the wall to slip and gap, meaning that there would be no relative movement parallel to the interface and no relative displacements perpendicular to the interface (Bentley Systems, 2025b).

2.3.14 3D modelling of sheet pile walls

In Plaxis 3D, sheet pile walls are modelled as plates, with a surrounding interface to enable interaction between the soil and the sheet pile wall. Modelling a sheet pile wall in 3D requires some additional parameters compared to 2D, in order to simulate the behavior in 3 dimensions. Since the sheet pile walls are modelled as plates that have a rectangular shape, the anisotropic behavior that the walls inhibits due to their shape has to be modelled by using anisotropic material behavior, meaning that it has parameters representing all three dimensions. The parameters simulating this behavior, as well as an explanation for them, can be found in Table 2.5.

The first and second axis exist in the same plane as the plate, while the third axis is perpendicular to the plane. Figure 2.6 and Figure 2.7 show the direction of the three axes as well as a visualization of what the different parameters represent. In these figures it can be seen that three different bending moments exist (Bentley Systems, 2025c), which is unlike 2D-modelling, where only one bending moment exist. Bending moment M_{11} corresponds with the bending moment that is analyzed in 2D. Three different shear forces also exist, and here it is shear force Q_{13} that corresponds with the shear force analyzed in 2D.

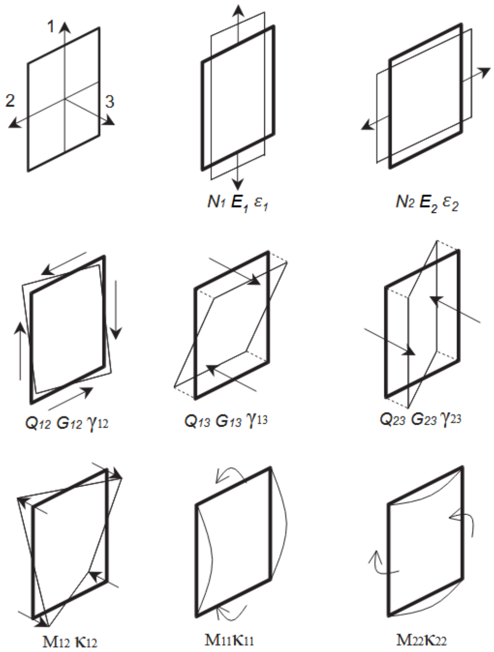

Figure 2.6: Definition of the direction of each axis, together with various parameters (Bentley Systems, 2025a).

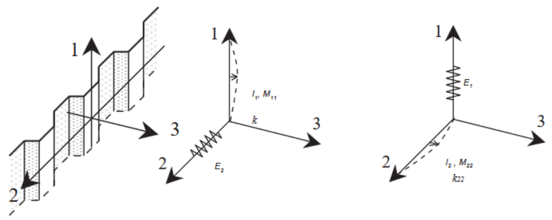

Figure 2.7: The three axes along a sheet pile wall, together with various parameters (Bentley Systems, 2025c).

The input parameters for the plates are shown in Table 2.5. Section 3.5.5 discusses how these parameters can be calculated.

Table 2.5: Input parameters for plate elements in PLAXIS 3D.

Property	Description	Unit
d_{eq}	Equivalent thickness of the plate element	m
E_1	Young's modulus in first axial direction	kN/m^2
E_2	Young's modulus in second axial direction	kN/m^2
G_{12}	In-plane shear modulus	kN/m^2
G_{13}	Out-of-plane shear modulus related to shear deformation over first direction	kN/m^2
G_{23}	Out-of-plane shear modulus related to shear deformation over second direction	kN/m^2
ν_{12}	Poisson's ratio	-

To calculate these parameters, additional parameters need to be known, shown in Table 2.6. The calculation of these parameters will be discussed in Section 3.5.5 and 3.6.

Table 2.6: Additional parameters for plate elements in PLAXIS 3D.

Property	Description	Unit
A_{13}	Effective material cross section area for shear forces Q_{13}	m^2
A_{23}	Effective material cross section area for shear forces Q_{23}	m^2
I_1	Moment of inertia against bending over the first axis	m^4
I_2	Moment of inertia against bending over the second axis	m^4
I_{12}	Moment of inertia against torsion	m^4

2.3.15 3D modelling of waling beams

The waling beams are modelled as a beam element in PLAXIS 3D. Just like the sheet pile walls, the beams have three degrees of freedom. The first axis is in the same direction as the axial beam direction, while the second and third axes are perpendicular to the first axis. The properties required for a waling beam in PLAXIS 3D are shown in Table 2.7. A visualization of the three axes are shown in Figure 2.8.

Table 2.7: Input parameters for a waling beam in 3D.

Property	Description	Unit
γ	Unit weight	kN/m^3
A	Beam cross section area	m^2
E	Young's modulus in the axial direction	kN/m^2
I_2	Moment of inertia against bending around the second axis	m^4
I_3	Moment of inertia against bending around the third axis	m^4

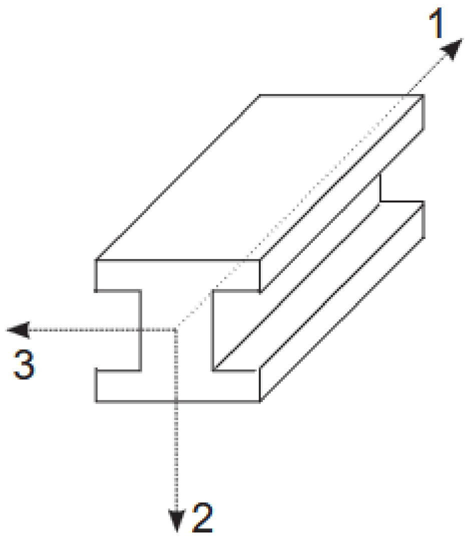

Figure 2.8: The three axes along a beam element (Bentley Systems, 2025c).

2.3.16 Comparison of 2D- and 3D-modelling

Whether 2D- or 3D-simulation should be used is dependent on what type of problem needs to be analyzed. For cases where the cross-section is uniform and for cases where the strain in the long dimension is essentially non-existent, 2D plane strain analysis is suitable. Plane strain is a condition in which the strain only occurs in one direction, but the normal stress are still be non-zero in the out-of-plane direction. However, a 2D plane strain analysis should (ideally) not be used when the site has ground anchors or foundation piling. (Lees, 2016).

When creating a model in 2D plane strain, it is assumed that the strain in the z-axis (third dimension) will be zero, and as a result the shear stress and strain will only have values in the 2D-plane. However, normal stress still exists in the third dimension (Lees, 2016). The geometry is represented by two dimensional elements, such as triangles and quadrilaterals (Potts, 1999). In a 2D plane strain model, the third dimension is simulated as an extension of the plane strain model in the perpendicular direction of the plane. This can result in the third dimension being simulated very differently in the plane strain model than what it actually is like in reality. A strut, pile, ground anchor and other structural elements can end up being modelled as continuous slabs instead of what they actually are, and a point load is functioning as an infinite line load in the third dimension. For such cases, it is very clear that the 2D plane strain model gives an incorrect version of the actual site (Lees, 2016).

Building a finite element model in 2D requires much less work than setting up a model in 3D. This is because the 3D model requires significantly more information on the geometry (Lees, 2016). In a 3D model there is strain in three dimensions instead of two. The geometry of the site is represented by three dimensional elements, such as hexahedra and tetrahedra. This leads to the 3D analysis having significantly more elements and nodes, thus increasing the time required for the analysis by several hours compared to a similar analysis in 2D (Potts, 1999).

2.3.17 Drained or undrained analysis

Whether to use a drained or undrained analysis mainly depends on the rate of loading. Drained analysis should be used when the rate of loading is slow enough for excess pore pressures to not be generated. Undrained analysis is more suitable for cases where the loading rate is high enough for the excess pore pressure to not dissipate (Lees, 2016). If in doubt, it is best to perform a consolidation analysis.

There are different methods for simulating undrained conditions in numerical modelling. Method A is an effective stress analysis and should be used when one wants to get the long-term outputs after construction in undrained conditions. This method generates excess pore pressures, and a consolidation analysis is done afterwards, where the excess pore pressures are dissipated, therefore simulating the long-term conditions. All the parameters, such as shear strength, are entered as effective values. To generate the excess pore pressures, the bulk modulus value for the pore water is high.

Method B is similar to Method A, but the shear stress is instead entered as its undrained value. This prevents the undrained shear strength from being overestimated, but will lead to the wrong prediction of excess pore pressures, so this method should not be used when a consolidation analysis is performed afterwards. This is because during a consolidation analysis, the excess pore pressures are dissipated, which in turn increases the effective stress, causing the soil to gain strength, but in Method B, the shear strength of the soil is fixed. If the excess pore pressures are wrong, the results are meaningless.

Method C is a total stress analysis and should be used when the other methods will predict unrealistic conditions. It takes the undrained shear strength as direct inputs, and the modulus is the undrained Young's modulus E_u, instead of E. As everything is in terms of total stress, no excess pore pressures are calculated. The undrained Poisson's ratio, ν_u, should be 0.5 so that the bulk modulus K_u can become infinitely small, but it is set 0.495 so that no numerical problems occur. This method cannot be followed by a consolidation analysis (Lees, 2016).

3 Methods

This chapter aims to describe the study area, how the geotechnical parameters needed for the constitutive models were obtained, and how the soil layering was modelled. Furthermore, the models used in PLAXIS 2D and 3D are described, going through the mesh generation, boundary conditions, construction stages, modelling of the structural materials, and other related information of interest.

3.1 Numerical calculations

To model the construction site and simulate the deformation of the sheet pile walls, PLAXIS 2D and PLAXIS 3D were used. These are softwares based on the finite element method, making analysis of geotechnical problems, such as excavations, possible. The results of the analyses are then viewed in PLAXIS Output, from which data can be extracted.

3.2 Study area

The entire site stretches approximately 25 by 40 meters with varying depths of excavation from level -0.97 m at the shallower parts to level -5.18 m at the deepest elevator shaft. The general ground surface elevation on the site originally sits at level +2.0 meters and the excavation was carried out in stages to allow for both access to the lower levels and additional support for the walls during installation. General purpose concrete of type C30/37 was cast as the excavation progressed to provide sufficient surfaces for further construction. A schematic for the horizontal projection of the site can be seen in Figure 3.1.

The site is confined by earth retaining embedded sheet pile walls to the north and west, whilst the south and east is enclosed by the foundations of already existing buildings. The confining sheet pile wall is referred to as "ytterspont" or outer sheet pile wall, and is of type PU12. To allow for the excavation of deeper elevator shafts, additional sheet pile walls are installed at lower levels inside the site, and these are made of type AZ18. The schematics for sheet pile wall PU12 and AZ18 are shown in Figure 3.2 and Figure 3.3. The data given from Norconsult shows that the largest deformations occurred in the northern sheet pile wall, making this area the most interesting for analysis. This is also where an inclinometer was placed, to measure the displacement of the outer sheet pile wall. No other inclinometers were placed on the site, but displacement were also measured using tape.

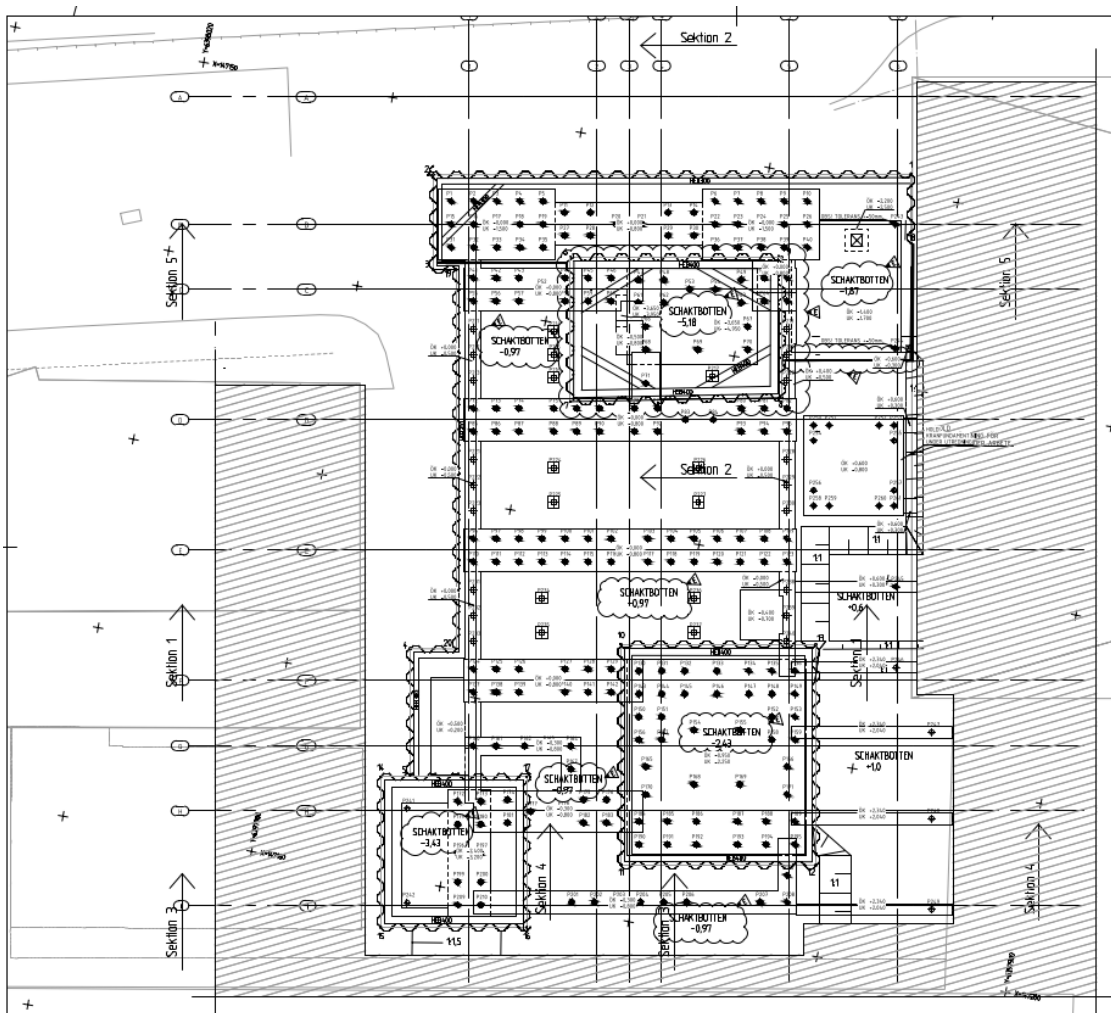

Figure 3.1: Plan view of the entire construction site of Hotell Draken

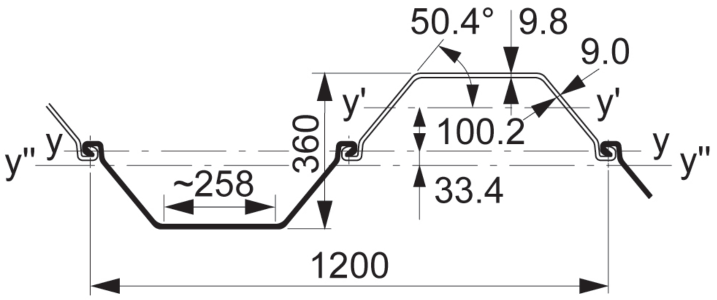

Figure 3.2: Sheet pile profile PU12, including dimensions [mm] (ArcelorMittal, 2022).

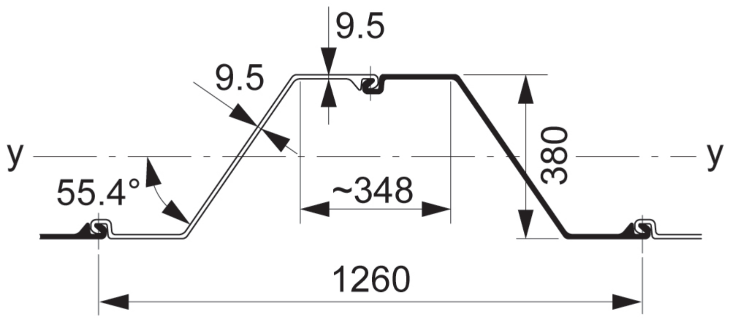

Figure 3.3: Sheet pile profile AZ18, including dimensions [mm] (ArcelorMittal, 2022).

3.3 Soil stratification

To determine the soil layering, several different parameters were considered to identify where the soil should be divided, a summary of field and laboratory investigations is shown in Figure 3.1. Undisturbed samples from the site were analyzed in laboratory and evaluated in connection with the feasibility study of the Hotel Draken project in 2016. Piston sampling were carried out at borehole NC2, after which oedometer tests of type CRS was performed at nine levels, direct simple shear tests at six levels and anisotropically consolidated undrained triaxial tests in compression at three levels. Soil type, density, natural water content, shear strength, sensitivity and liquid limit were also evaluated.

Additionally, disturbed soil sampling was carried out. Soil-rock sounding at boreholes NC1, NC2, NC3 and NC5 for identifying the depth to bedrock, field vane test at borehole NC5 for determination of the undrained shear strength in-situ, CPT tests at borehole NC6 and NC7 for determining the thickness and stratification of the soil, and flight auger sampling for classification of the top stratum at all boreholes. Results from the CPT are shown in Figure 3.5.

To complement the available data from the testing campaign at Hotel Draken, additional undisturbed piston sampling carried out in 2024 from project Mashuggskajen was used. Available laboratory investigation from borehole NC2406 provided CRS tests at seven levels, direct simple shear tests at four levels and triaxial tests in both compression and extension at three and two levels respectively. A compilation of all the results from the laboratory investigations on undisturbed piston samples are shown in Figure 3.4.

When using more advanced constitutive models such as the Creep-SCLAY1S model there is also an increased demand for more thorough soil investigations to produce the required input parameters. Therefore, the work of Tornborg et al. (2021), modelling the adjacent Göta tunnel, was used as support.

Table 3.1: Summary of field and laboratory investigations

ID	In-situ	Laboratory	Project
NC1	SRS, CFR		Hotel Draken
NC2	SRS, CFA, PS	CRS, CAUC, DSS	Hotel Draken
NC3	SRS, CFA		Hotel Draken
NC4	CFA		Hotel Draken
NC5	SRS, FVT, CFA		Hotel Draken
NC6	CPT, CFA		Hotel Draken
NC7	CPT, CFA		Hotel Draken
NC2406	PS	CRS, CAUC, CAUE, DSS	Masthuggskajen
1/430		CRS, IL, CAUC, CAUE	Tornborg et al. (2021)

(*PS*) Piston Sampling, (*CFA*) Continuous Flight Auger, (*SRS*) Soil-Rock Sounding, (*FVT*) Field Vane Test, (*CPT*) Cone Penetration Test, (*CRS*) Constant Rate of Strain, (*IL*) Incrementally Loaded, (*DSS*) Direct Simple Shear test, (*CAUC*) Consolidated Anisotropically Undrained Compression triaxial test, (*CAUE*) Consolidated Anisotropically Undrained Extension triaxial test.

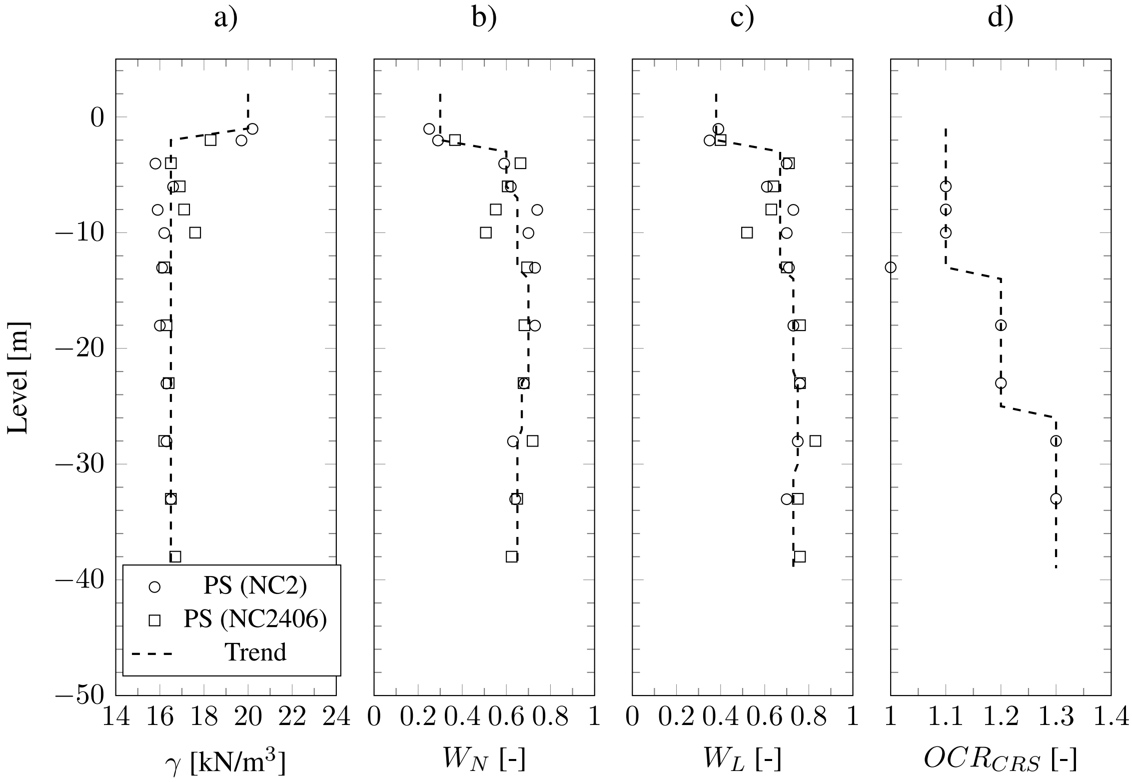

Figure 3.4: Results from laboratory investigations on undisturbed piston samples. a) Unit weight, b) Natural water content, c) Liquid limit, d) OCR from CRS test.

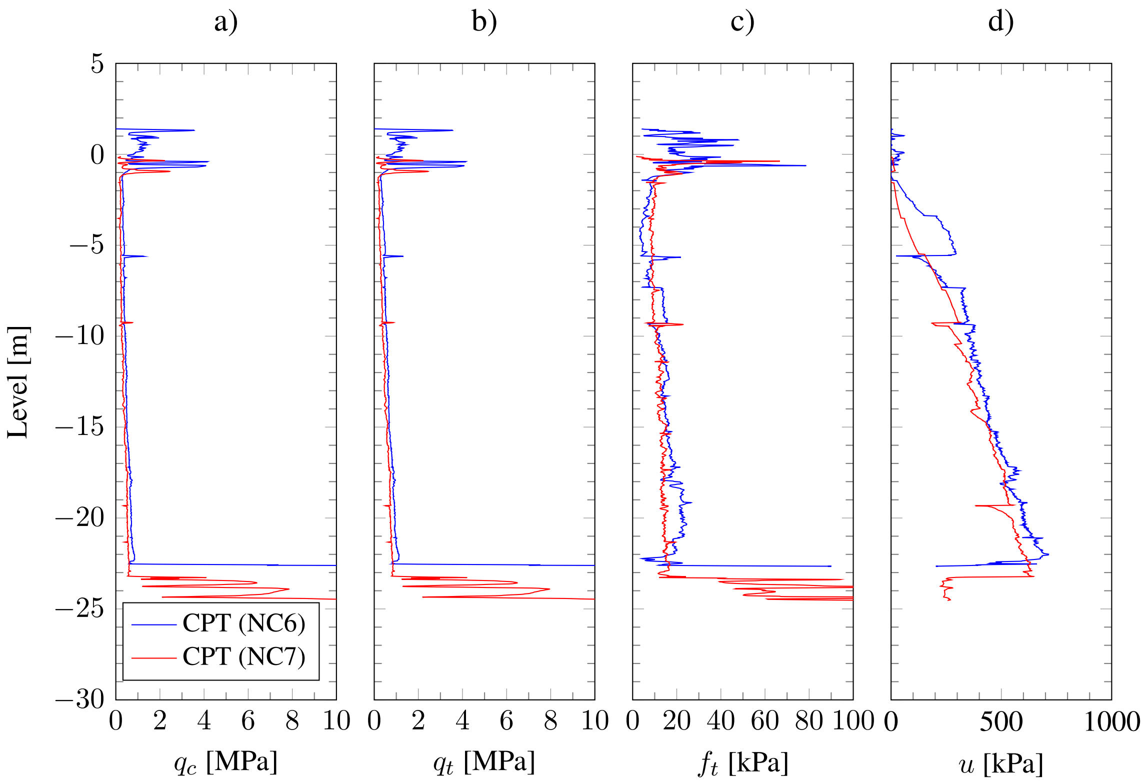

Figure 3.5: Results from CPT. a) Cone tip resistance, b) Cone tip resistance corrected for pore pressure effects, c) Sleeve friction, d) Pore water pressure.

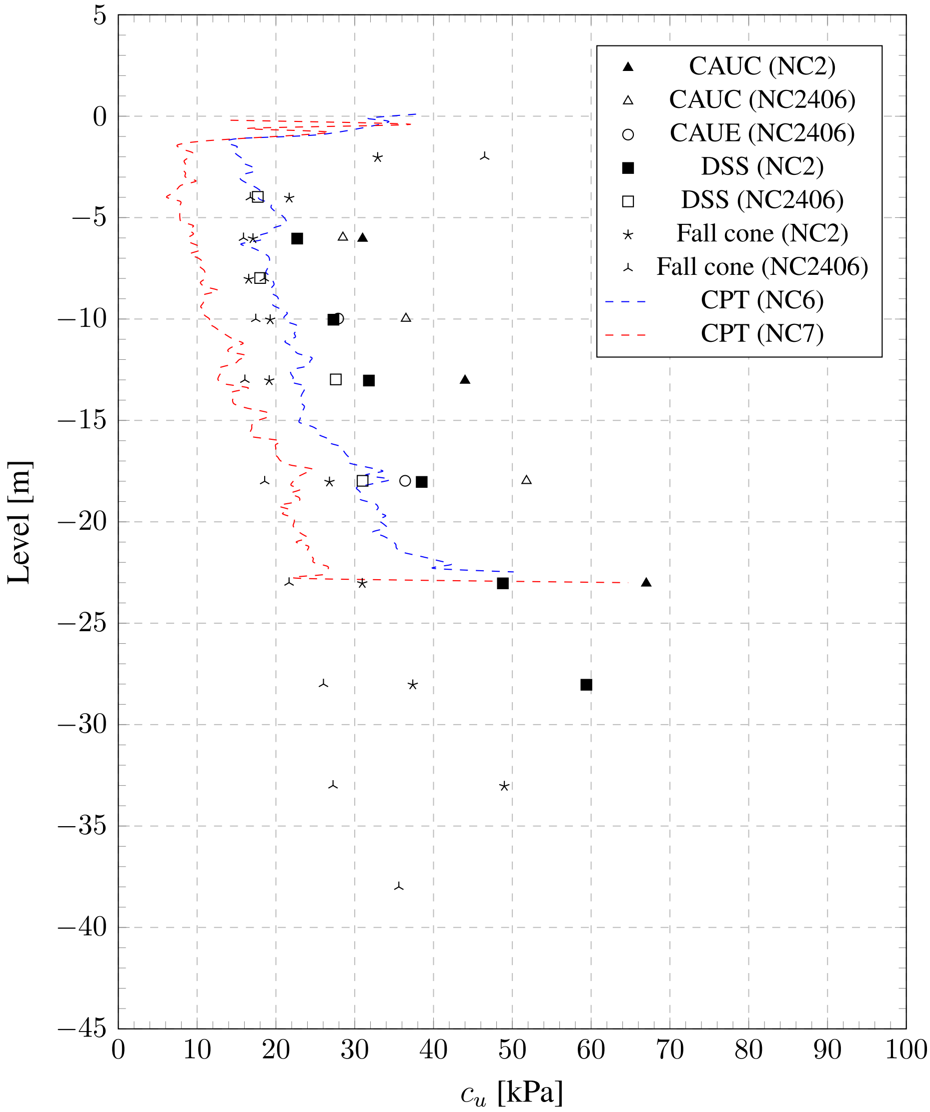

Figure 3.6: Undrained shear strength.

3.3.1 Fill

The compilation of the in-situ and laboratory investigations shown in Figures 3.4, 3.5 and 3.6 together with provided observations of the piston samples resulted in the following stratification: A top layer of asphalt, followed by a fill material consisting of mainly sand, mixed with construction debris such as concrete, wood and brick. Gravel, loam and clay could also be found. The fill material is estimated to extend between the surface level at +2 m down to a level of -1 m. The composition of the different fractions in the fill varies greatly. The saturated unit weight was approximated to 20 kN/m^3 and the natural water content and liquid limit to 30 % and 38 % respectively from piston samples.

3.3.2 Clay

Below the fill is a layer of dry crust, which transitions into looser and grayer sulfide-stained clay with shell fragments and plant residue. Layers of sand can also be found. The clay layer is estimated to extend from a level of -1 m down to level -35 to -40 m in the west and -22 m in the east of the site, underlain with frictional material with a thickness of between 0 and 3 m. The saturated unit weight of the clay was determined from piston samples to 16.5 kN/m^3 and showed little to no variation with depth. The natural water content and liquid limit showed greater variation ranging from 55 % to 70 % and 60 % to 75 % respectively, the clay was therefore divided into three different layers.

The result of the CRS test provides a relationship between stress, strain and pore water pressure for the soil. The preconsolidation pressure (σ'_c) can then determined from plotting of a linear scale stress (x-axis) -strain (reversed y-axis) curve using the Sällfors 1975 method, as shown in Figure 3.7. The first and second straight-line segment of the curve is extended until they intersect. An isosceles triangle with its base against the curve is then drawn in the space formed between the two straight lines and the oedometer curve. The intersection point formed at the left corner of the isosceles triangle represents the preconsolidation pressure. From CRS tests the clay was determined to be normally- to slightly over- consolidated with an OCR ranging from 1.1 to 1.3.

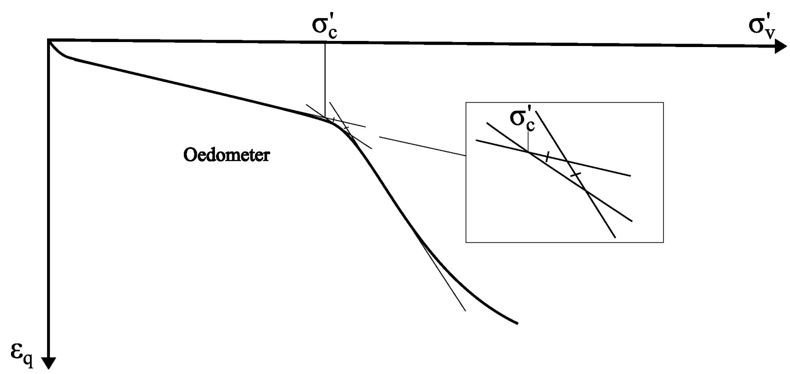

Figure 3.7: Determination of the preconsolidation pressure.

3.3.3 Depth to bedrock

By means of soil-rock sounding the depth to bedrock was determined. It was found that the depth varied greatly, especially between the western and eastern part of the site. In the north east and south east the bedrock sits at a level of -23 m and -25 m respectively. In the north west and south west the bedrock sits at a level of -40 m and -45 m respectively. Due to the large depth to the bedrock, it was decided to be excluded from the model, which allowed for the K_0-procedure to be utilized instead of gravity loading.

3.3.4 Groundwater

The groundwater table was measured to a depth of approximately 2 m, corresponding to a level of +0 m. The same average groundwater level was also observed in the Göta River in connection with the Masthuggskajen project. Measurements from project Masthuggskajen also showed slightly elevated pore pressures in the clay compared to hydrostatic conditions, corresponding to a hydrostatic pressure level of +1.5 m at 20 meters depth. However, Tornborg et al. (2021) showed a hydrostatic increase with depth based on piezometer readings at the Göta tunnel project. Therefore, a hydrostatic increase with depth from level +0 m is assumed.

3.3.5 Input parameters for the Mohr-Coulomb model

The fill layer was modelled using the Mohr-Coulomb model. The friction angle and stiffness was determined empirically by Equations 3.1 and 3.2 from CPT following Trafikverket (2025). The resulting trends are shown in Figure 3.8, from which the friction angle was estimated to 32° and the stiffness to 5 MPa, corresponding well to a description of loosely packed silty sand or sandy silt. Poisson's ratio generally lies in the range of 0.3 to 0.35 for sands and was set to 0.3. Using the Undrained A method, PLAXIS will perform an effective stress analysis and the effective cohesion was set to 1 kPa as to prevent unwanted failure of the soil. The angle of dilatancy was set to 2°, corresponding to $\varphi' - 30°$ (Bentley Systems, 2025a). Assuming non-zero dilatancy in undrained analyses has the implication that the soil layer in question will have an infinite (undrained) shear strength. The values for the fill layer are shown in Table 3.2.

$$\varphi' = 29 + 2.8 \cdot q_c^{0.45} \tag{3.1}$$

$$E'_{ref} = 4.3 \cdot q_t^{0.93} \tag{3.2}$$

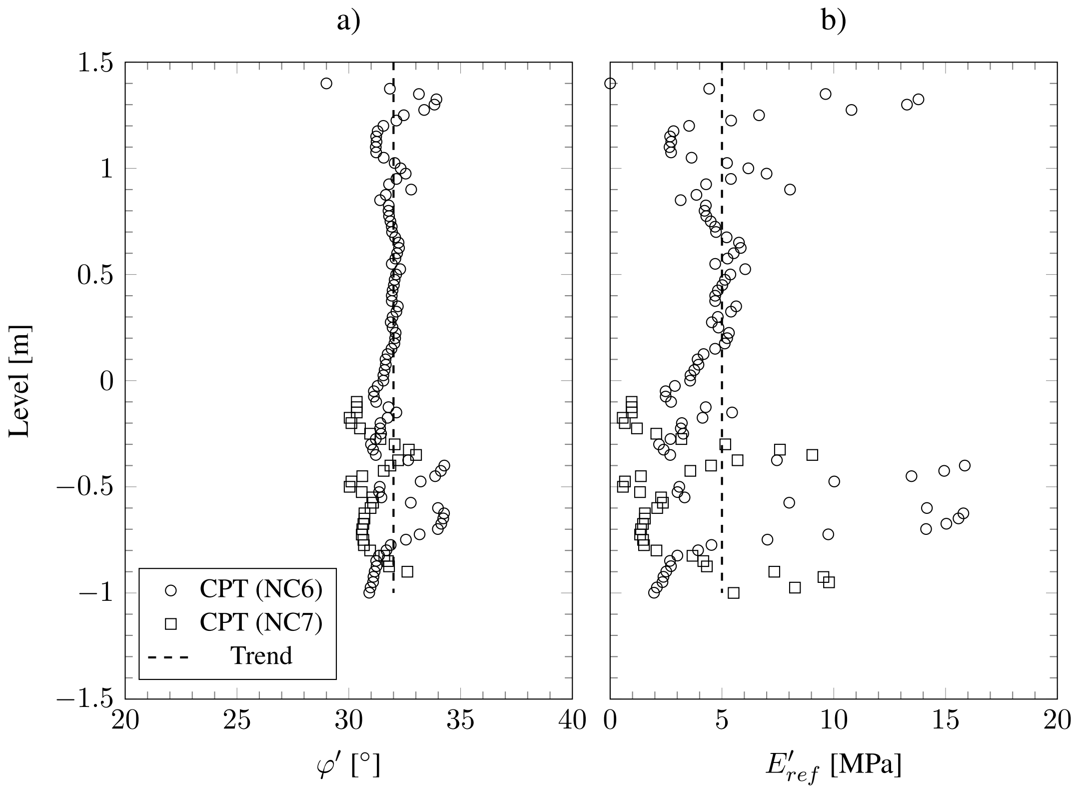

Figure 3.8: Derived properties from CPT at boreholes NC6 and NC7 for fill layer. a) Friction angle, b) Young's modulus.

Table 3.2: Input parameters in PLAXIS for the fill layer using the Mohr-Coulomb model.

Property	Value	Unit
γ_{unsat}	18	kN/m^3
γ_{sat}	20	kN/m^3
E'_{ref}	5000	kN/m^2
ν'	0.3	-
c'	1	kN/m^2
φ'	32	^{o}
ψ	2	^{o}

3.3.6 Input parameters for the NGI-ADP model

The input parameters used for the three clay layers using the NGI-ADP model are shown in Table 3.3. As explained previously, the NGI-AGP model requires input of the shear strain and shear strength from triaxial compression, triaxial extension, and direct simple shear test. These tests were carried out previously on samples from the construction site of Hotel Draken, as well as on samples taken from project Masthuggskajen. The resulting trends used as input for PLAXIS is shown in Figure 3.9. The separation of the clay into different layers enabled the ratio between active, passive and direct shear to change according to the chosen trend, while maintaining the overall increase.

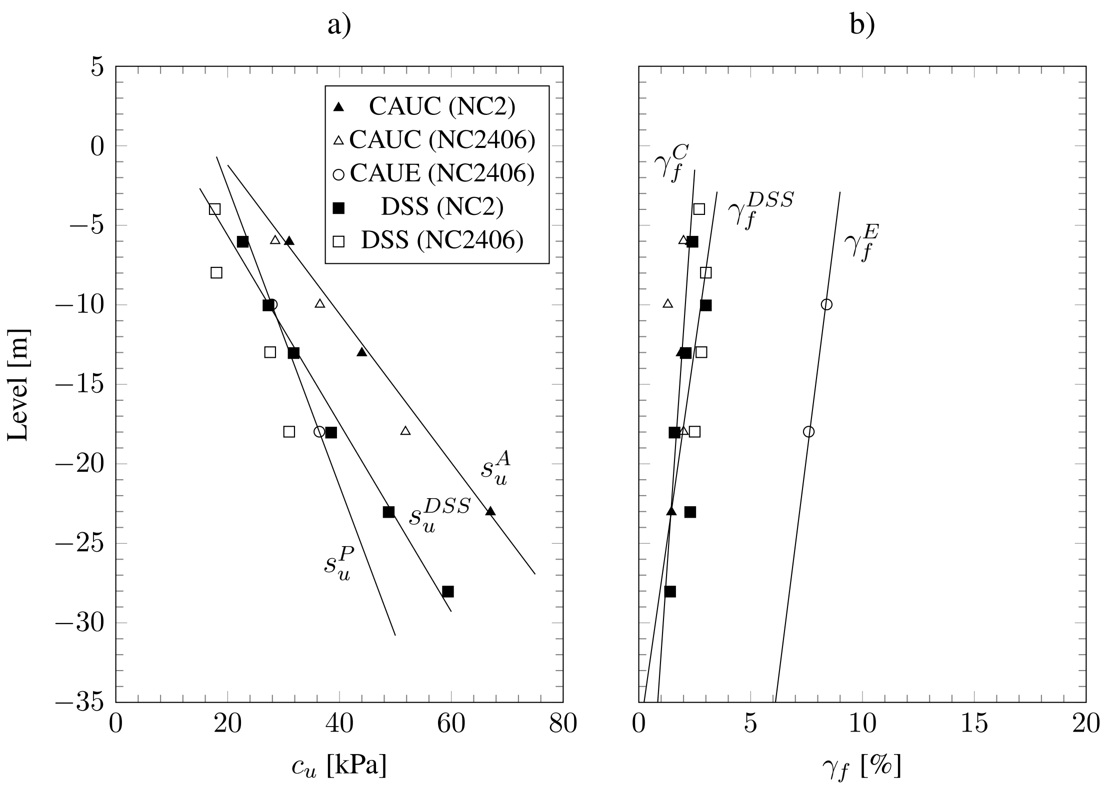

Figure 3.9: Chosen trends for shear strength and shear strain in compression, extension and direct shear for NGI-ADP. a) Undrained shear strength at peak strength, b) Corresponding shear strain at peak strength.

The shear strength and shear strain in compression at different depths were determined from CAUC tests performed on samples from borehole NC2 and NC2406. From these tests the peak strength and corresponding strain was used. The reference depth y_{ref} was set at the top of each layer, from which the increase of shear strength $s^A_{u,inc}$ followed the chosen trend. For the initial mobilization τ_o/s^A_u, the default value of 0.7 was used (Bentley Systems, 2025a). The peak shear strength and strain in extension were determined from CAUE tests, which were only available from borehole NC2406, as no such tests were performed at samples from the Hotel Draken site. Borehole NC2406 was situated about 60 meters north of the construction site of Hotel Draken, but it was assumed to be fairly representative of the soil at Hotel Draken, since the soil in this wider area is considered to be homogenous.

The shear strain and shear strength in direct simple shear were taken from direct simple shear tests performed on samples taken at borehole NC2. The data from the tests were presented as graphs plotting the shear strength versus the change in angle in radians divided by 100. The shear strength was determined as the peak shear strength that was reached during the test. The shear strain, γ_s had to be calculated by finding the corresponding change in angle, γ_c, for the peak shear strength, using Equations 3.3 and 3.4. Here, Δs is the horizontal displacement of the sample, H is the effective height of the sample after consolidation, and D is the diameter of the sample.

$$\Delta s = H \cdot \gamma_c \tag{3.3}$$

$$\gamma_s = \frac{\Delta s}{D} \tag{3.4}$$

The unloading/reloading shear modulus, G_{ur}, should normally be determined from a triaxial test that includes unloading and reloading, by plotting the shear stress vs. the shear strain, from which the slope of unloading/reloading part would represent G_{ur}. Since no such test was performed, G_{ur} instead had to be determined empirically with Equation 3.5, taken from Sponthandboken. Where c_u^{DSS} is the shear strength in direct shear test and w_L is the liquid limit.

$$G_{ur} = G_0 = \frac{504 \cdot c_u^{DSS}}{w_L} \tag{3.5}$$

Table 3.3: Input parameters in PLAXIS for the clay layers using the NGI-ADP model.

Property	Layer 1	Layer 2	Layer 3	Unit
γ_{unsat}	16.5	16.5	16.5	kN/m^3
γ_{sat}	16.5	16.5	16.5	kN/m^3
γ_f^C	2.4	2.1	1.4	%
γ_f^E	8.9	8.4	7.1	%
γ_f^{DSS}	2.7	3	2.3	%
$s_{u,ref}^A$	21.7	32.3	47.3	kN/m^2
y_{ref}	-2	-7	-14	m
$s_{u,inc}^A$	2.1	2.1	2.1	kN/m^2/m
s_u^P/s_u^A	0.83	0.72	0.62	-
τ_0/s_u^A	0.7	0.7	0.7	-
s_u^{DSS}/s_u^A	0.67	0.71	0.74	-
G_{ur}/s_u^A	499	531	499	-

3.3.7 Input parameters for the Creep-SCLAY1S model

For the Creep-SCLAY1S model it is possible to switch off various model features by the choice of input parameters. Destructuration and bonding can be switched off by setting the initial amount of bonding χ_0 to zero. In doing so, the modified intrinsic compression index λ_i^* can be substituted for the modified compression index λ^* as the ICS always will take the shape of the NCS (Equation 3.6). Hence, the input for destructuraion, ξ and ξ_d are only placeholders and will not effect the model (Karstunen and Amavasai, 2017).

$$p'_m = p'_{mi}(1-\chi) => p'_m = p'_{mi} \tag{3.6}$$

λ^* can be determined from oedometer tests by plotting the volumetric strains versus the natural logarithm of the mean effective stress, The slope of the virgin consolidation line represents λ^* and will capture the non linear elastic behavior. κ^* is the slope of the swelling line and would normally be determined in a similar manner as for λ^*. However, this require the oedometer test to incorporate unloading and reloading, from which the swelling line can be obtained. An approximation of κ^* was instead obtained from the slope of the normal compression line. Both λ^* and κ^* was then optimized in PLAXIS using the soil test function until it corresponded to the in-situ CRS tests.

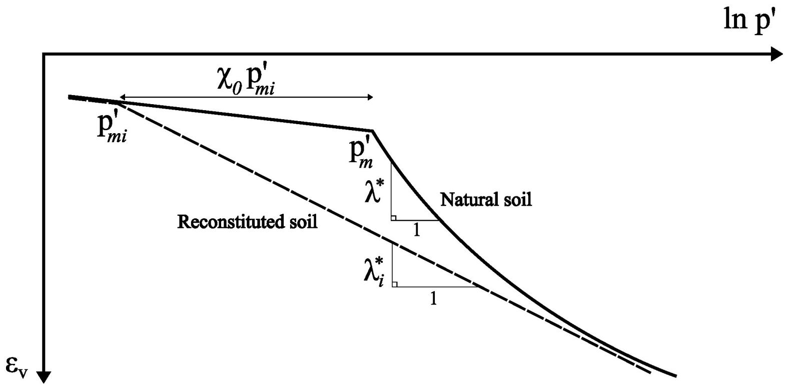

Figure 3.10: Determination of the modified compression index.

The preconsolidation pressure was determined from CRS tests performed at samples from borehole NC2 as described earlier in Section 3.3.2. Using OCR enable an increasing pre-overburden pressure with depth. Thus, in the model POP can be set to zero.

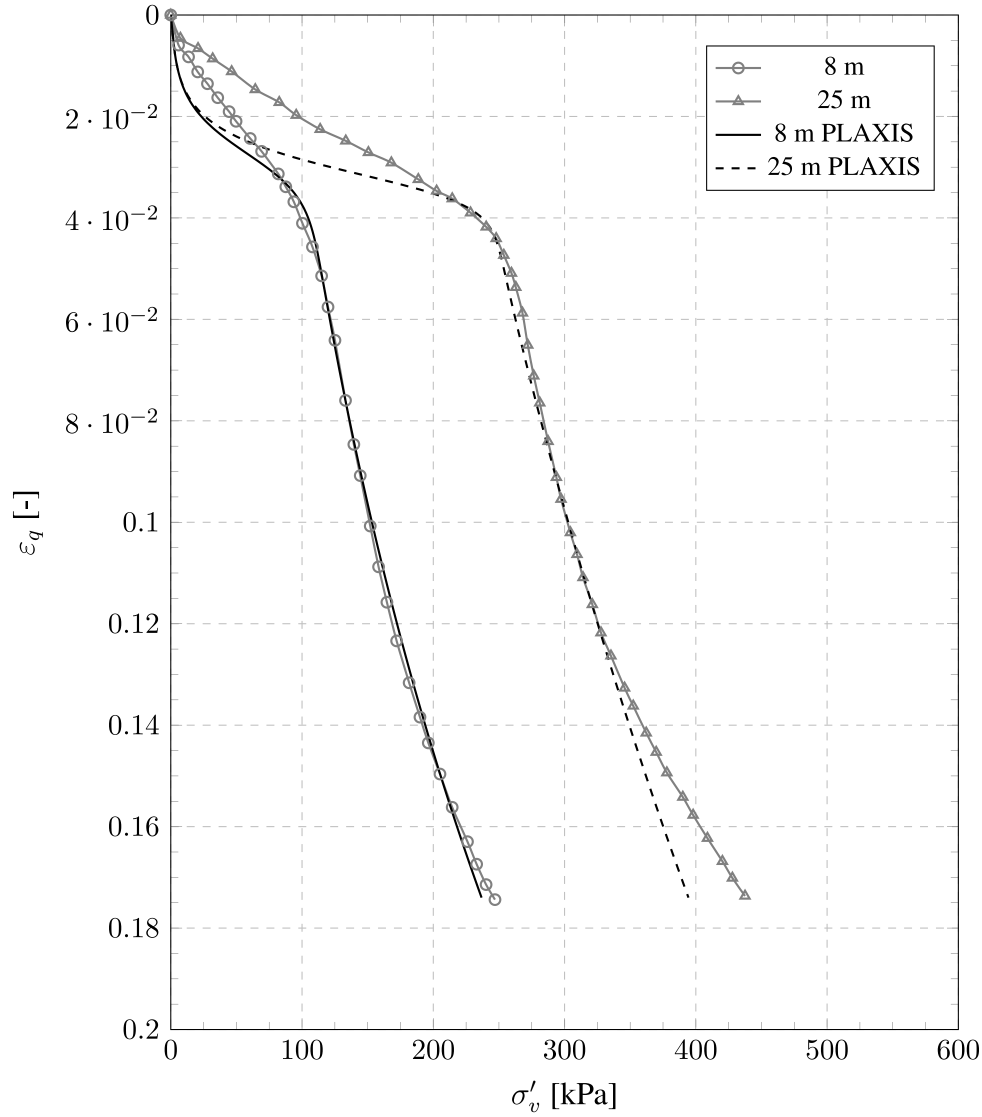

Figure 3.11: CRS test results at borehole NC2 compared to PLAXIS CRS soil test.

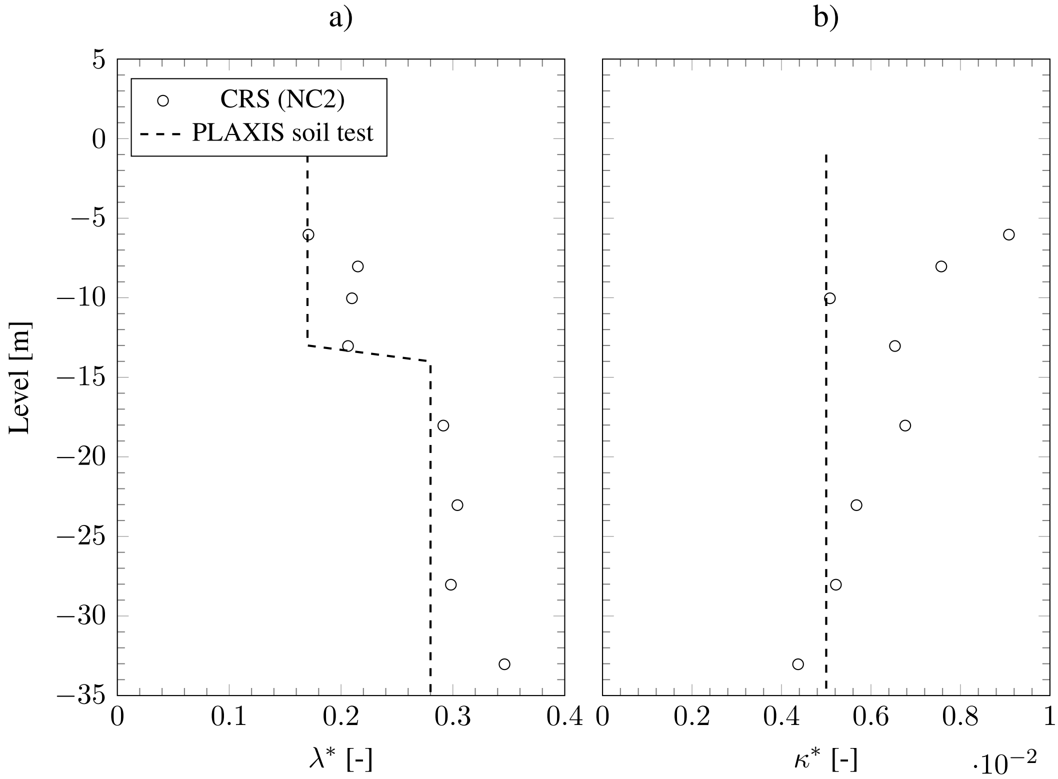

Figure 3.12: Depth dependency and chosen trends for λ^* and κ^* by optimization with CRS soil test in PLAXIS.

The stress ratios at critical state, M_c and M_e, are the slope of the critical state line in compression and extension respectively, interpreted from CAUC and CAUE triaxial tests. The critical state friction angle in compression could then be calculated with Equation 3.7 and from Jaky's formula (Equation 3.8) the normally consolidated coefficient of earth pressure at rest could be approximated. Again, the initial anisotropy and the relative effectiveness of rotational hardening due to deviatoric straining could be calculated from Equations 3.10 and 3.11 respectively, using the normally consolidated stress ratio (q/p') in Equation 3.9 (Karstunen and Amavasai, 2017).

$$sin\varphi'_c = \frac{3M_c}{6+M_c} \tag{3.7}$$

$$K_0^{NC} = 1 - sin\varphi'_c \tag{3.8}$$

$$\eta_{K_0^{NC}} = \frac{3M_c}{6-M_c} \tag{3.9}$$

$$\alpha_0 = \frac{\eta_{K_0^{NC}}^2 + 3\eta_{K_0^{NC}} - M_c^2}{3} \tag{3.10}$$

$$\omega_d = \frac{3(4M_c^2 - 4\eta_{K_0^{NC}}^2 - 3\eta_{K_0^{NC}})}{8(\eta_{K_0^{NC}}^2 - M_c^2 + 2\eta_{K_0^{NC}})} \tag{3.11}$$

CAUE triaxial tests were as previously mentioned only available for borehole NC2406 from project Masthuggskajen. From figure 3.13 M_c was estimated to 1.3 and M_e to 1.4. However, in general $M_c > M_e$ (Karstunen and Amavasai, 2017). Conservatively, M_e can be estimated from the critical state fiction angle in compression by adopting the Mohr-Coulomb failure criterion, which would result in Equation 3.12. The result of such an assumption will in this case implicate a significantly lower critical state stress ratio in extension, as shown with the dashed line in Figure 3.13, more in line with earlier investigation by Tornborg et al., (2021).

$$sin\varphi'_c = \frac{3M_c}{6+M_c} = \frac{3M_e}{6-M_e} => M_e = \frac{3M_c}{3+M_c} = \frac{6sin\varphi'_c}{3+sin\varphi'_c} \tag{3.12}$$

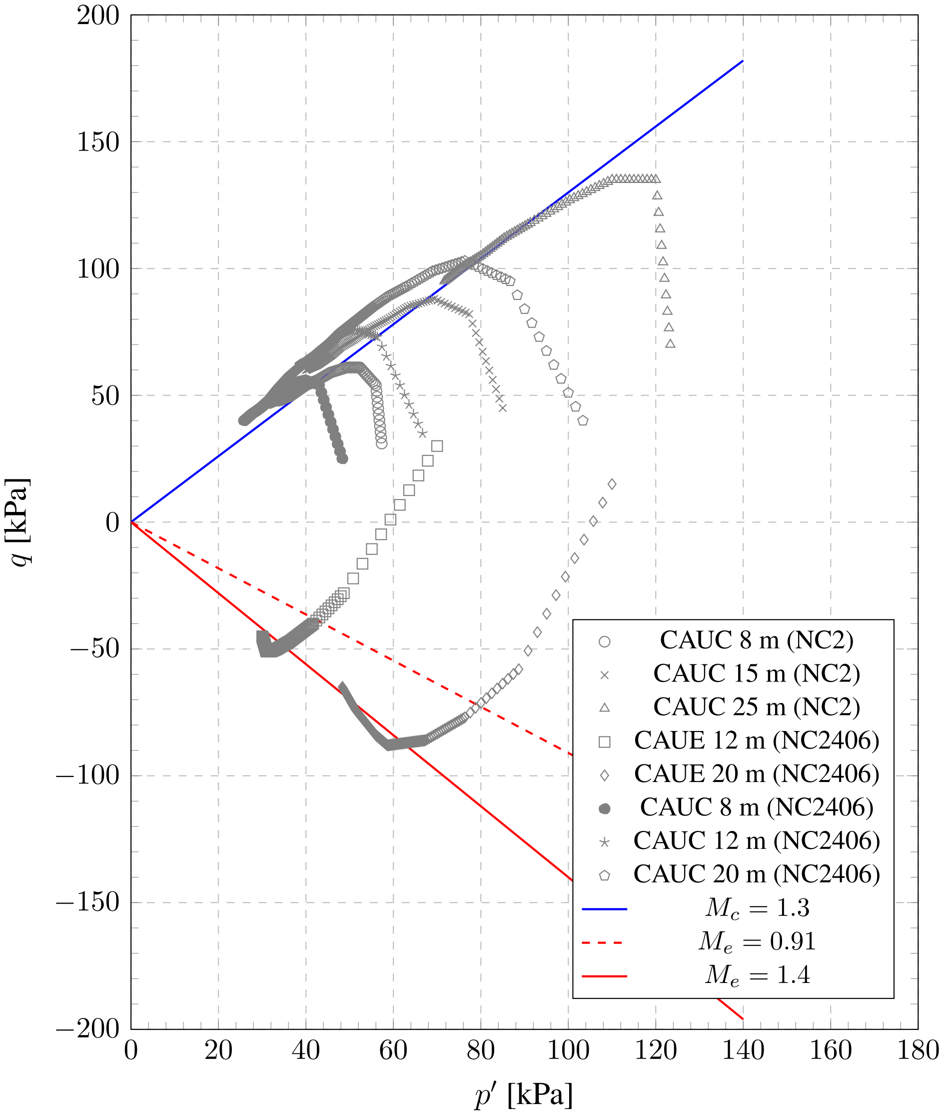

Figure 3.13: Triaxial test results, where $q = (\sigma'_1 - \sigma'_3)$ is the deviatoric stress and $p' = (\sigma'_1 + 2\sigma'_3)/3$ the mean effective stress.

The absolute rate of rotational hardening and the initial void ratio was taken from Tornborg et al. (2021), as it was not possible to obtain these input parameters from the available oedometer data. Furthermore, when using a so called user-defined material model in PLAXIS such as the Creep-SCLAY1S model, it is necessary to define the mechanical behavior of the interfaces separately. The interface friction angel φ_{inter} equals the critical state friction angle in triaxial compression, shown in Equation 3.13.

$$\varphi_{inter} = \varphi'_c = sin^{-1}\left(\frac{3M_c}{6+M_c}\right) \tag{3.13}$$

The reference oedometer modulus E_{oed}^{ref} is the tangential stiffness at the reference vertical stress of p^{ref} (Equation 3.14). The reference vertical stress can be obtained from the oedometer linear scale stress (x-axis) -strain (reversed y-axis) curve, where p^{ref} is the value in the middle of the virgin consolidation line, between the preconsolidation pressure (σ'_c) and limit pressure (σ'_L). In such case E'_{oed} is the oedometer stiffness corresponding the compression modulus M_L and the major principal effective stress (σ'_1) is equal to the preconsolidation pressure.

$$E_{oed}^{ref} = E'_{oed}\left(\frac{p_{ref}}{\sigma'_1}\right) = M_L\left(\frac{p_{ref}}{\sigma'_c}\right) \tag{3.14}$$

Table 3.4: Input parameters in PLAXIS for the clay layers using the Creep-SCLAY1S model.

Property	Layer 1	Layer 2	Layer 3	Unit
γ_{unsat}	16.5	16.5	16.5	kN/m^3
γ_{sat}	16.5	16.5	16.5	kN/m^3
e_0	1.99	1.55	0.96	-
POP	0	0	0	-
OCR	1.1	1.1	1.2	-
α_0	0.5	0.5	0.5	-
χ_0	0	0	0	-
λ_i^* (λ^*)	0.17	0.17	0.28	-
κ^*	0.005	0.005	0.005	-
ν'	0.2	0.2	0.2	-
μ_i^*	0.152	0.152	0.165	-
τ	1	1	1	day
M_c	1.3	1.3	1.3	-
M_e	0.91	0.91	0.91	-
ω	200	200	200	-
ω_d	0.86	0.86	0.86	-
ξ	8	8	8	-
ξ_d	0.5	0.5	0.5	-
K_0^{NC}	0.47	0.47	0.47	-
E_{oed}^{ref}	1003	1120	1151	kN/m^2
φ_{inter}	32.3	32.3	32.3	$^\circ$

3.4 2D model

To model the site in PLAXIS 2D, the plan view shown in Figure 3.1, and the drawings of cross-section 2 and cross-section 4 shown in Figure A.1 and Figure A.2, were used as a basis. Cross-section 2 shows the northern part of the site, which is where the focus of this project is, but the rest of the construction site was also included for the results to be as realistic as possible. The 2D model analysis was done as small strain analysis since the movements of the retaining wall are so small that large strains are not relevant.

The lowering of groundwater was simulated by drawing a new global water level for each stage where the geometry changed below the original groundwater level, and setting it to the global water level. It was done in this way so that the pore pressure would be calculated from the correct depth.

3.4.1 Simplifications

In Figure A.1 it can be seen that in the area between sheet pile wall PU12 and the sheet pile wall of type AZ18 in front of it, the ground is excavated to level -1.87. This was not included in the PLAXIS model. Instead the ground is excavated to level -0.97, like the rest of the model. This is because the excavation to level -1.87 did not occur until at the very end of the project and was filled up almost immediately again, according to information given from Norconsult, so it would likely have had a very small effect on the overall movement of the wall.

No other buildings outside the construction site were included. Including Götatunneln, which is 10 meters to the north of the site would have been complicated and time consuming. The building to the south of the construction site was omitted because it was far away from sheet pile wall PU12, so it was deemed unnecessary to include.

3.4.2 Boundary effects

According to Lees (2016), the placement of the boundaries (i.e. how far the model should reach) should be considered carefully. Boundary effects will be introduced if the boundaries are placed too close to the area of interest. Therefore, the boundaries should be far enough away that the output will not be significantly affected by the placement of the boundaries. Setting the north boundary to where Götatunneln is located, namely 10 meters north of construction site, resulted in very large boundary effects. Because of this, the model had to be stretched further. It was decided that the model should stretch 40 meters north of the construction site, since letting the model reach further than that had very little effect on the final output. The model reaches all the way down to the bedrock level.

3.4.3 Boundary conditions

The boundaries for the groundwater flow were set so that the groundwater could freely flow from through the left boundary, right boundary, and upper boundary. The lower boundary, boundaryXmin, was set to closed, because of the bedrock underneath.

3.4.4 Surcharge load effects

Since information on how the machines were placed during the construction process was limited, assumptions were made regarding this. Two different scenarios were analyzed for the 2D simulations, one with loads and one without any loads, shown in Table 3.5. Loads were placed where it would make sense for them to be during different construction stages, such as right next to a soil mass that was excavated or right next to a sheet pile wall during installation. In the scenario that included loads, there was a continuous load placed to the north of the site, because machines would enter the site from here during the entire construction process, and machines would also be placed there for excavation. The loads were modelled as 5 meter long line loads with a load of 10 kPa.

Table 3.5: Load scenarios for the 2D model

Scenario	Description
1	No loads from machines
2	Continuous load to the north of the construction site, and various loads during the entire construction process

3.4.5 Structural elements

Several structural elements had to be included in the PLAXIS 2D model to accurately model the area. As explained in chapter 2.3.13, the sheet pile walls were modelled as plate elements with surrounding interfaces that enable the interaction between the plate and the soil. They were modelled as isotropic materials, meaning that they behave the same in all directions.

The outer sheet pile wall was of type PU12, whereas the inner sheet pile walls were made of type AZ18. The corner struts were of type HEB400. The properties for these elements are shown in Tables 3.6 and 3.7. Modelling the corner struts as they are in reality would not be possible since they stretch into the third dimension. However, the four corner struts that were installed in the deep elevator shaft were modelled as one node to node anchor going across the excavation. All the structural elements are modelled as linear elastic, which as earlier discussed is satisfactory if the stiffness of a structure is much higher than that of the surrounding soil.

Table 3.6: Properties of sheet pile wall AZ18 and sheet pile wall PU12

Property	AZ18	PU12	Unit
γ	1.15	1.16	kN/m
EA	$31.6 \cdot 10^6$	$29.4 \cdot 10^6$	kN/m
EI	$71.8 \cdot 10^3$	$45.4 \cdot 10^3$	kN/m^2/m

Table 3.7: Properties of corner strut HEB400

Property	Value	Unit
A	0.02	m^2
EA	$4.2 \cdot 10^6$	kN/m
$L_{spacing}$	3.2	m

The concrete was modelled as a soil with a plate in the middle, and its properties are shown in Table 3.8. It was done like this because modelling the concrete using the concrete model in PLAXIS requires a lot of input parameters. Since the concrete was such a small part of the model, it was deemed unnecessary to model the hardening of the concrete, which is not relevant here. The plate was put in the middle of the soil so that the bending moment and shear forces could be directly extracted from the output. The plates were given the same unit weight as the concrete, and the other properties matched the properties of concrete type C30/37.

Table 3.8: Properties of the concrete layer

Property	Value	Unit
γ_{unsat}	24	kN/m^3
γ_{sat}	24	kN/m^3
E_{ref}	33000000	kN/m^2
v	0.2	-

3.4.6 2D Construction stages

The construction phases used in PLAXIS 2D are shown in Table 3.9. They are based on the construction stages that were described for cross-section 2. Some of the construction stages were not included in the PLAXIS 2D model, like the installation of wailing beams, since those cannot be simulated in this 2D model, since they stretch into the third dimension. All the construction stages except the initial stage were done as plastic construction stages, so they were not time-dependent.

Table 3.9: Construction phases used in PLAXIS 2D

Stage	Description
Initial phase	K_o procedure
Null phase	Reset displacements to zero and restore equilibrium
Stage 1	The outer sheet pile wall is installed.
Stage 2	Excavation on the inner side of the northern sheet pile wall to level +1.
Stage 3	Excavation on the entire construction site to level +0.5.
Stage 4	Local excavations to install the sheet pile walls for the deep elevator shafts to level -0.8.
Stage 5	Installation of the sheet pile walls around the elevator shafts.
Stage 6	Phase 1 of the excavation to level -0,97 outside the elevator shafts.
Stage 7	Concrete casting for phase 1 of the excavation to level -0,97.
Stage 8	Phase 2 of the excavation to level -0,97 outside the elevator shafts.
Stage 9	Concrete casting for phase 2 of the excavation to level -0,97.
Stage 10	Excavation to level -1 inside the southern elevator shaft for Phase 3.
Stage 11	Excavation to level -2.43 on the northern half inside the southern elevator shaft for Phase 3.
Stage 12	Concrete casting inside southern elevator shaft for Phase 3.
Stage 13	Excavation to level -2.3 inside the northern elevator shaft and excavation to level -2.43 inside the southern half of the southern elevator shaft for phase 4.
Stage 14	Concrete casting inside the southern elevator shaft for phase 4.
Stage 15	Installation of corner struts at level -1.8 inside the northern elevator shaft.
Stage 16	Excavation to level -5.18 inside the northern elevator shaft.
Stage 17	Concrete casting at the bottom of the northern elevator shaft.

3.4.7 Mesh generation

According to Lees (2016), the mesh should be refined until the results of the analysis do not change. Refining the mesh further past this point is not necessary since it will increase the computation times while barely increasing the accuracy. The mesh close to the northern sheet pile wall was refined more than the mesh further away. This is because the area further away would not have as big of an effect on the results around the sheet pile wall, and it was therefore deemed unnecessary to have a very fine mesh further away, thus increasing computation times. A coarseness factor of 0.5 was set at the area close to the sheet pile wall and a coarseness factor of 0.7 was set at the area further away.

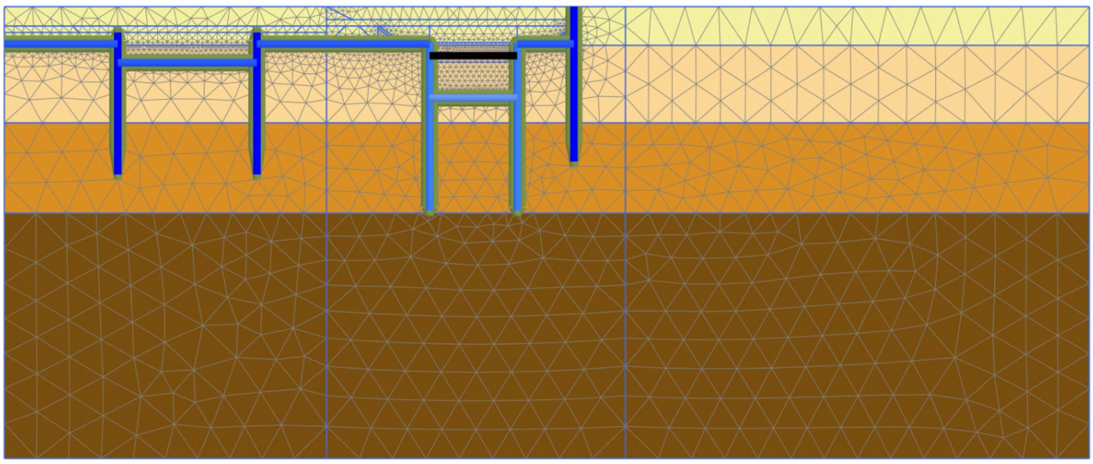

Figure 3.14: Final 2D mesh of the site.

The mesh sensitivity was assessed by comparing the results of the horizontal displacement and bending moment in the northern outer sheet pile wall at the last construction stage, shown in Figure 3.15. It was only done for the scenario that included loads and the same mesh refinement was used for both constitutive models. The results obtained after mesh refinement were very similar to the results obtained beforehand, meaning that mesh refinement did not make a difference.

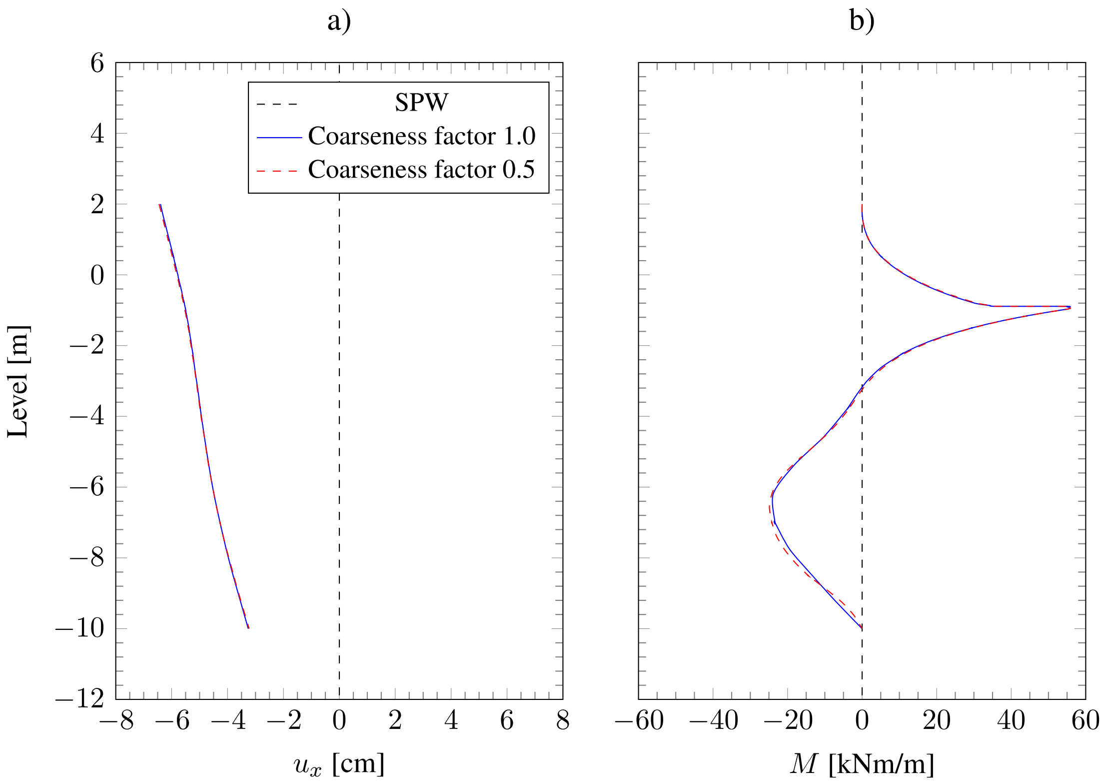

Figure 3.15: Mesh sensitivity study in PLAXIS 2D, using the NGI-ADP model with loads. a) Cumulative horizontal displacement in the sheet pile wall, b) Bending moment.

3.5 3D model

Creating a model in PLAXIS 3D is much more complicated than creating a model in PLAXIS 2D. Unlike the 2D model where the site was modelled as a cross-section, the entire site was modelled in 3D. This means that the wailing beams and corner struts that could not be represented in 2D were included in the 3D model. As can be seen in Figure 3.1, the site is surrounded by other buildings and has a non symmetrical horizontal projection. The eastern and southern part of the excavation did not have any need for sheet pile walls because it was adjacent to a concrete building. Modelling the site in 3D made it possible to include the concrete foundations of these buildings as well as the non-symmetrical effects. The analysis of the 3D model was done as a small strain analysis.

In the 2D model, the lowering of groundwater that took place during excavation was done by creating a new water level for each phase where excavation took place. Doing this in 3D would have been very complicated and time consuming, so the lowering of groundwater was instead done by setting excavated clusters to dry, and by making the soil layers beneath excavated clusters interpolate pore pressures. This ensures that the water pressure starts from zero at the bottom of the excavation, rather than from where the original groundwater level is.

3.5.1 Simplifications

To create a 3D model in a reasonable time, as well as to keep the calculation times fairly short, simplifications were made for the 3D model. For example, the local excavations that were done in several steps, which were simulated in the 2D model, were not simulated in 3D, because it would have made the geometry too complicated and it would also have been very time consuming to include all of this detail. Numerical errors would likely have developed because of errors in the geometry if the site was modelled with too much detail. Furthermore, only the elevator shaft in the northern section, the one shown in cross-section 2, was modelled, meaning that the elevator shafts in the southern half were not included. This was because the southern elevator shafts were unlikely to have any significant results on the horizontal displacement of the northern sheet pile wall. The excavation to level -1.87 right next to the northern sheet pile wall was excluded, just like in the 2D model.

3.5.2 Boundary effects

At the actual construction site there was an inclination of the bedrock from the eastern side to the western side. This could have been included in the 3D model, but it was decided that it was unnecessary because the bedrock is far enough down into the ground that it would not have an effect on the results. The model reaches 40 meters north of the construction site, to be as similar to the 2D model as possible.

3.5.3 Boundary conditions

In a 3D model, the groundwater boundaries need to be determined for six boundaries instead of four, like in a 2D model. All boundaries were set to open, except for boundaryZmin, the boundary at the bottom of the model, because of the bedrock below the site.

3.5.4 Surcharge load effects

It was assumed that there would be a continuous load just to the north of the northern sheet pile wall during the entire construction process, because this is where machines would enter the site. Machines would also be placed here for excavation purposes. Because of these uncertainties regarding the loads, two different scenarios were analyzed, shown in Table 3.10. These scenarios were made so that they would correspond to the scenarios made for the 2D case. The loads were modelled as surface loads with a load of 10 kPa.

Table 3.10: Load scenarios for the 3D model

Scenario	Description
1	No loads from machines
2	Continuous load just north of the northern sheet pile wall, and 2 different loads inside the excavated area

3.5.5 Structural elements

As mentioned in Section 2.3.14, there are different ways to obtain the parameters needed for 3D modelling of sheet pile walls. The values shown in Table 3.11 are based on the recommended values for these parameters, according to the PLAXIS material models manual (Bentley Systems, 2025c), but since there are different ways to obtain these values, a sensitivity analysis was done, which is discussed further in Section 3.6.

Young's modulus for steel E_{steel}, is the stiffness of the steel type, in this case S355. This along with the area moment of inertia against bending over the first axis I_1 and the cross-sectional area A_1 can be obtained from manufacturers specifications. However, since the plate elements in PLAXIS 3D are modelled as a rectangular shaped plate rather than the original AZ or PU profile, the inputs need to be expressed in terms of equivalent parameters. The equivalent thickness of the plate d_{eq} per meter is calculated as for the 2D case with Equation 3.15, derived from the formula for area moment of inertia for a rectangular plate with the height $h = d_{eq}$.

$$d_{eq} = \sqrt{\frac{12 E_{steel} I_1}{E_{steel} A_1}} \tag{3.15}$$

Using the equivalent thickness it is now possible to calculate an equivalent Young's modulus $E_{1.eq}$ for the plate using Equation 3.16, such that the bending stiffness in the first direction of the sheet pile wall is equal to the bending stiffness of the equivalent plate, $E_{steel} I_1 = E_{1.eq} I_{1.eq}$.

$$E_{1.eq} = \frac{12 E_{steel} I_1}{d_{eq}^3} \tag{3.16}$$

The value of I_2 will affect E_2, and is not provided by the manufacturer. According to the PLAXIS material models manual (Bentley Systems, 2025c) I_2 can be assumed as $I_1/20$, since it is known that the bending stiffness in the first direction should be larger than in the second direction. The bending stiffness in the second direction is related as $E_{steel}I_2 = E_{2.eq}I_{2.eq}$.

$$E_{2.eq} = \frac{12E_{steel}I_2}{d_{eq}^3} \approx \frac{12E_{steel}I_1}{20d_{eq}^3} = \frac{E_{1.eq}}{20} \tag{3.17}$$

The equivalent in-plane shear modulus $G_{12.eq}$ for a rectangular plate can be calculated using Equation 3.18. The area moment of inertia against torsion I_{12} is once again an estimate provided in the PLAXIS matarial models manual (Bentley Systems, 2025c). $I_{12} = I_1/10$ again such that $E_{steel}I_{12} = E_{12.eq}I_{12.eq}$. Poison's ratio is the same as for steel $\nu_{steel} = 0.3$.

$$G_{12.eq} = \frac{6E_{steel}I_{12}}{(1+\nu_{steel})d_{eq}^3} \approx \frac{6E_{steel}I_1}{10(1+\nu_{steel})d_{eq}^3} \tag{3.18}$$

The equivalent out-of-plane shear modulus related to shear deformation over the first direction $G_{13.eq}$ depends on the axial stiffness such that $E_{steel}A_{13} = E_{13.eq}A_{13.eq}$. It is assumed that the cross-sectional area that is effective against shear deformation over the first direction is about 1/3 of the total cross-section area, $A_{13} = A_1/3$ (Bentley Systems, 2025c).

$$G_{13.eq} = \frac{E_{steel}A_{13}}{2(1+\nu_{steel})d_{eq}} \approx \frac{E_{steel}A_1}{6(1+\nu_{steel})d_{eq}} \tag{3.19}$$

The out-of-plane shear modulus related to shear deformation over the second direction $G_{23.eq}$ also depends on the axial stiffness such that $E_{steel}A_{23} = E_{23.eq}A_{23.eq}$. Here It is instead assumed that the cross-sectional area that is effective against shear deformation over the second direction is about 1/10 of the total cross-section area, $A_{23} = A_1/10$ (Bentley Systems, 2025c).

$$G_{23} = \frac{E_{steel}A_{23}}{2(1+\nu_{steel})d_{eq}} \approx \frac{E_{steel}A_1}{20(1+\nu_{steel})d_{eq}} \tag{3.20}$$

Table 3.11: Properties of sheet pile walls AZ18 and PU12 in 3D.

Property	AZ18	PU12	Unit
d	0.52	0.43	m
E_1	$6.05 \cdot 10^6$	$6.83 \cdot 10^6$	kN/m^2
E_2	$302 \cdot 10^3$	$342 \cdot 10^3$	kN/m^2
G_{12}	$233 \cdot 10^3$	$263 \cdot 10^3$	kN/m^2
G_{13}	$775 \cdot 10^3$	$876 \cdot 10^3$	kN/m^2
G_{23}	$233 \cdot 10^3$	$263 \cdot 10^3$	kN/m^2
v_{12}	0.3	0.3	-

The properties for the wailing beams were based on information from the manufacturer, and no calculations needed to be done. The values are shown in Table 3.12.

Table 3.12: Properties of waling beams HEB300 and HEB400.

Property	HEB300	HEB400	Unit
A	0.015	0.020	m^2
E	$2.100 \cdot 10^2$	$2.100 \cdot 10^2$	kN/m^2
I_2	$2.517 \cdot 10^{-4}$	$5.770 \cdot 10^{-4}$	m^4
I_3	$8.563 \cdot 10^{-5}$	$1.082 \cdot 10^{-4}$	m^4

The concrete was modelled as a linear elastic material. No plate was put in the middle of the concrete for the 3D model. The properties of the concrete are shown in Table 3.13.

Table 3.13: Properties of the concrete in 3D.

Property	Value	Unit
γ_{unsat}	10	kN/m^3
γ_{sat}	10	kN/m^3
E_{ref}	100000	kN/m^2
v	0.2	-

3.5.6 3D construction stages

The constructions stages for the 3D model are shown in Table 3.14. Because of the many simplifications that were made for the 3D model, the number of construction stages are fewer. This is mainly because of the absence of the local excavations. All the construction stages except the initial stage were done as plastic construction stages.

Table 3.14: Construction phases used in Plaxis 3D

Stage	Description
Initial phase	K_o procedure.
Null phase	Reset displacements to zero and restore equilibrium.
Stage 1	The outer sheet pile wall is installed.
Stage 2	Excavation of the entire construction site to level +1.
Stage 3	Installation of waling beams and corner struts on the outer sheet pile wall.
Stage 4	Excavation on the entire construction site to level +0.5.
Stage 5	Local excavation to install the sheet pile walls for the deep elevator shafts.
Stage 6	Installation of the sheet pile walls around the elevator shafts.
Stage 7	Excavation of the entire construction site to level -0.97.
Stage 8	Concrete casting on the entire construction site.
Stage 9	Excavation to level -2.3 inside the northern elevator shaft.
Stage 10	Installation of waling beams and corner struts inside the northern elevator shaft.
Stage 11	Excavation to level -5.18 inside the northern elevator shaft.
Stage 12	Concrete casting at the bottom of the northern elevator shaft.

3.5.7 Mesh generation

Because the calculation times were already rather long without refining the mesh, the focus of the mesh refinement was on the the area closest to the sheet pile wall. Refining the whole model would have led to calculation times being too long. A coarseness factor of 0.7 was tested and the horizontal displacement of the sheet pile wall very similar to how it was before refining the mesh, as shown in Figure 3.16. However, for the bending moment in different directions, convergence proved more difficult to reach, so the mesh had to be refined further. At a coarseness factor of 0.2 in the area closest to the sheet pile wall, convergence was reached for bending moment M_{11} and bending moment M_{12}. However, it was not possible to reach convergence for the bending moment M_{22}.

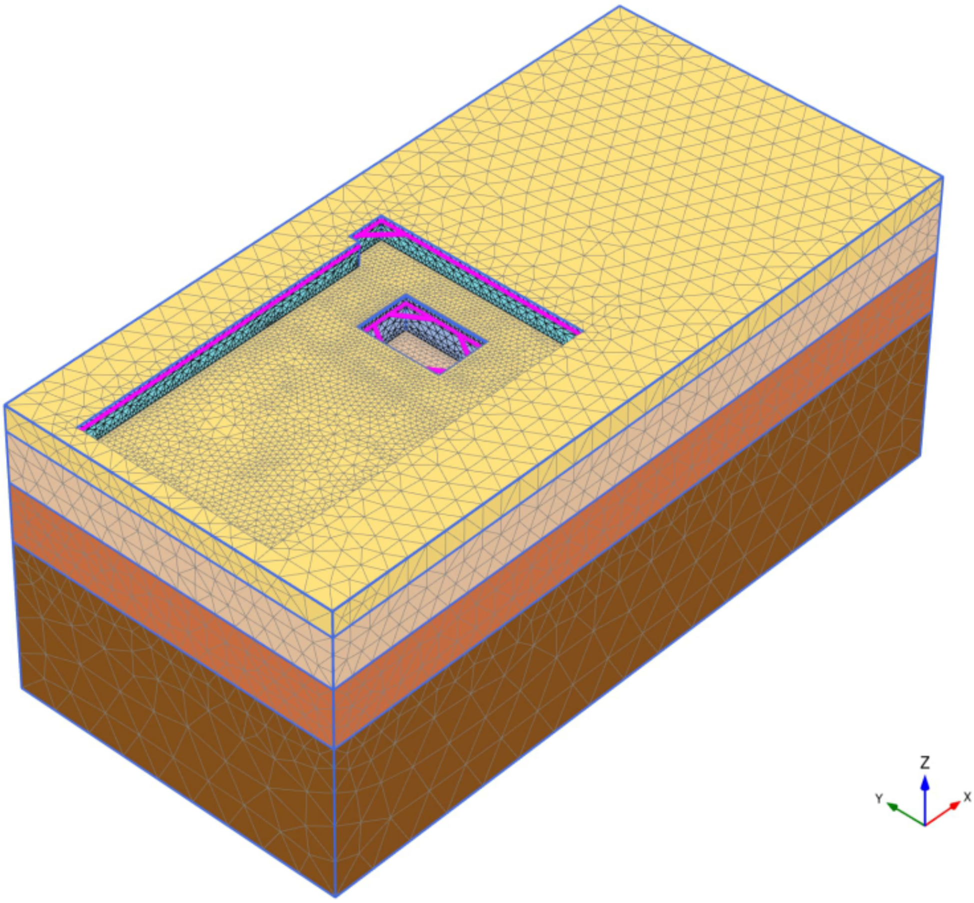

Figure 3.16: Final 3D mesh of the site.

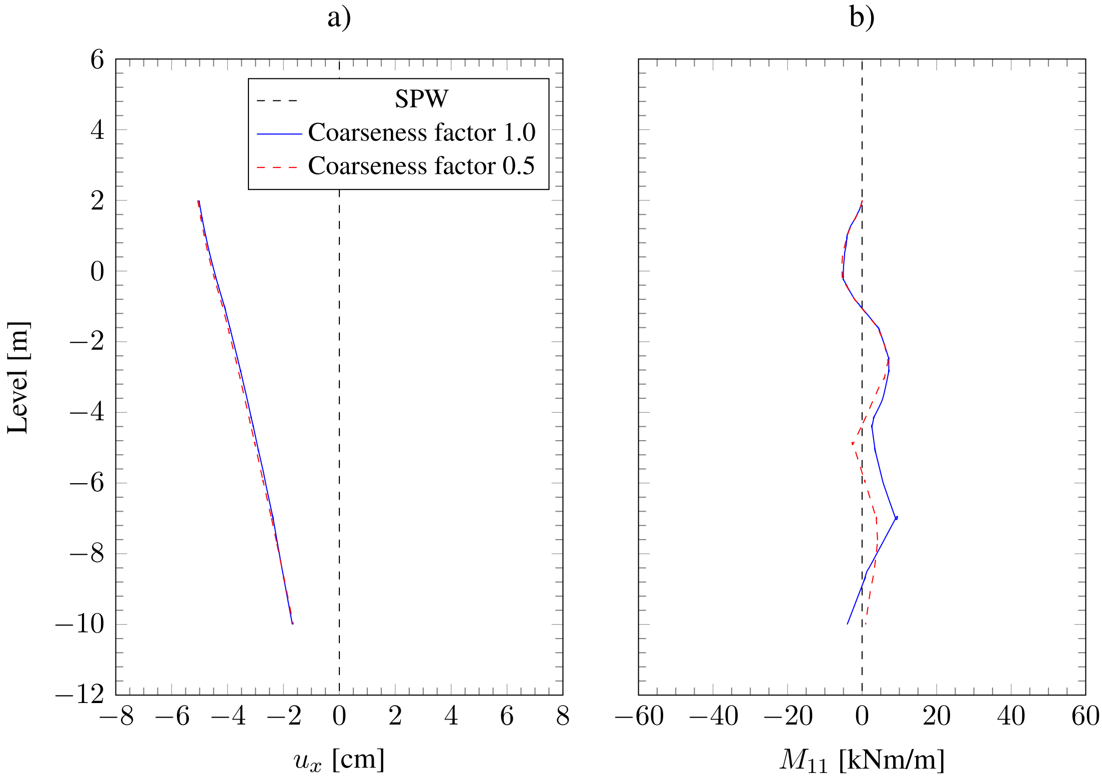

Figure 3.17: Mesh sensitivity study in PLAXIS 3D, using the NGI-ADP model with loads. a) Cumulative horizontal displacement in the sheet pile wall, b) Bending moment.

3.6 Parametric study

The determination of the parameters representing the anisotropic behavior of the sheet pile walls needed to be studied. This is because there is uncertainty in some of the parameters The Plaxis manual gives a brief explanation of what the parameters represent but does not go into detail about how they should be determined.

According to Bentley Systems (2025c), I_2 can be assumed to be $I_1/20$. This is not realistic, since the moment of inertia against bending over the second axis should be magnitudes smaller than the moment of inertia against bending over the first axis. However, there is a possibility that the value of I_2 will have a miniscule effect on the final results. Because of this, a sensitivity analysis was done on I_2 where the results were compared between when using $I_2 = I_1/20$, $I_2 = I_1/1000$, and $I_2 = I_1/10000$, to determine if the magnitude of this value will make any difference.

Another sensitivity analysis of I_{12} was also performed. The Plaxis manual states that $I_{12} = I_1/10$, so this was also compared with $I_{12} = I_1/1000$ and $I_{12} = I_1/10000$.

4 Results

The results obtained during analysis are presented in this chapter. It is divided into several sections, with Section 4.1 and its subsections showing the results of the 2D analysis, and Section 4.2 and its subsections showing the results of the 3D analysis.

4.1 Results of 2D analysis

In this section the results of the 2D analysis of NGI-ADP and Creep-CLAY1S are presented and discussed.

4.1.1 Horizontal displacement in 2D

The cumulative horizontal displacement of the sheet pile wall at different construction stages when using the NGI-ADP model for the scenario including loads are shown in Figure 4.1a. The predictions resulted in a maximum cumulative horizontal displacement of 6.59 cm towards the south at level +2 m during stage 13. During this stage there was an excavation inside the northern elevator shaft, which lead to there being less soil resisting the wall movement on the passive side of the outer sheet pile wall. The concrete casting at the bottom of the northern elevator shaft in the final stage (stage 17) did not contribute to further displacement, but instead moved the wall back to a cumulative displacement of 6.45 cm at level +2 m. This suggests that the concrete helped push the wall back. The shape of the wall obtained an s-shaped curvature at stage 16, similar to what the inclinometer showed. There was barely any difference in the displacement at the top 2 meters of the wall during this stage compared to stage 13, but the lower parts of the wall saw large displacements because of the excavations in the deep elevator shaft.

The cumulative horizontal displacement of the sheet pile wall for when using the Creep-SCLAY1S model is shown in Figure 4.1b. The maximum horizontal displacement of 4.5 cm occurred at the top of the sheet pile wall in both stage 13 and stage 17. This is in contrast to the result from the NGI-ADP model, where stage 13 had a slightly larger displacement than stage 17. The s-shaped curvature of the wall was not obtained here and the overall displacement is much smaller compared to when using the NGI-ADP model, suggesting a stronger soil.

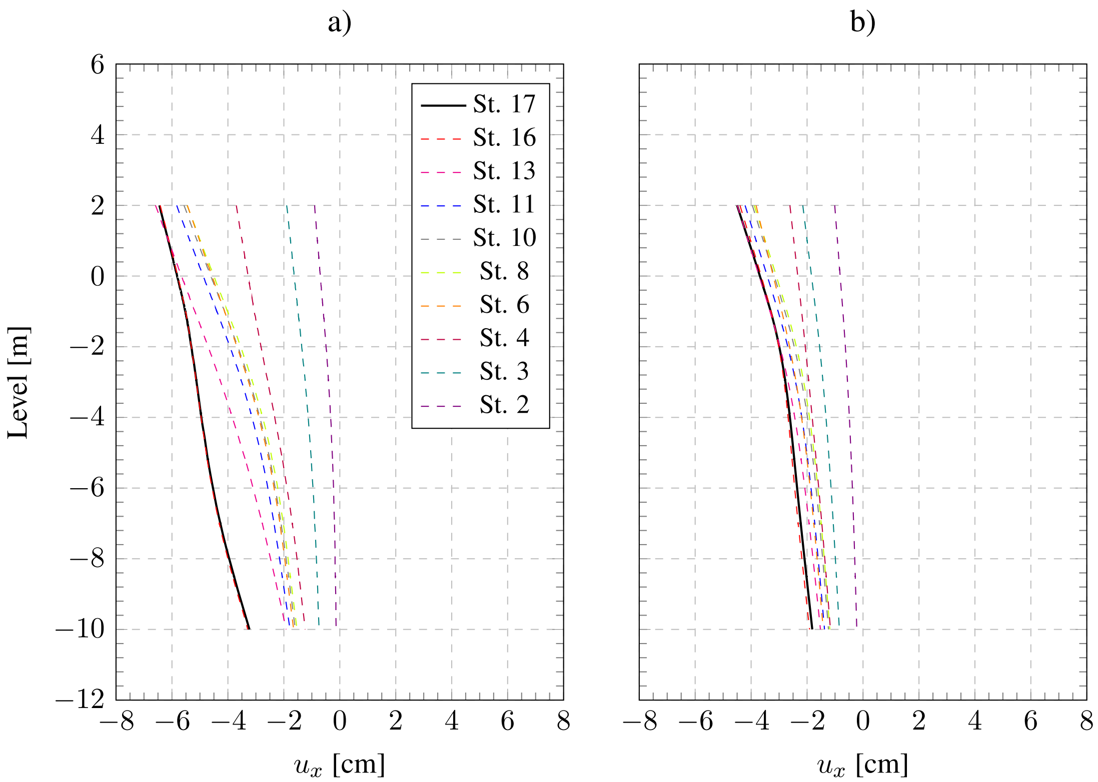

Figure 4.1: Development of the cumulative horizontal displacement in the northern, outer sheet pile wall for stages of excavation in PLAXIS 2D with loads. a) NGI-ADP, b) Creep-SCLAY1S.

The final stages of the different load scenarios, using both the NGI-ADP model and Creep-SCLAY1S model are shown in Figure 4.2, together with the maximum and minimum inclinometer results measured during 1 month post installation of the wall. It becomes clear that the strength of the soil is underestimated when using the NGI-ADP model, as opposed to Creep-SCLAY1S, which is much closer to reality. This is interesting, since NGI-ADP takes direct input of the shear strength, derived from triaxial and direct shear tests. Using the Creep-SCLAY1S model, the predicted displacement of the wall matched the inclinometer results much better. When loads were included, the displacement of the wall at the very top matches one of the inclinometer readings almost exactly. Without any loads the displacement at the top was somewhat underestimated, but the two load scenarios converged at the bottom, just like when using NGI-ADP. However, for both loading scenarios, the displacement was overestimated from around level -6 to level -10, suggesting that the strength of the soil was underestimated at this depth. From Figure 4.2

It can also be seen that when using the NGI-ADP model, the shape of the displacement curve for the wall matches the inclinometer readings much better when including loads, as the maximum cumulative horizontal displacement can be found at the top of the wall. Without any loads, an "s-shaped" curve is not obtained. Instead, the maximum displacement occurs at around level -4 m, which is completely different from the inclinometer results that show that the displacement generally decreases further down. However, by including the loads, the horizontal displacement is overestimated further up the wall, which is not the case when loads are not present. As can be seen, the loads have less of an influence further down the wall, with the two load cases converging towards the bottom.

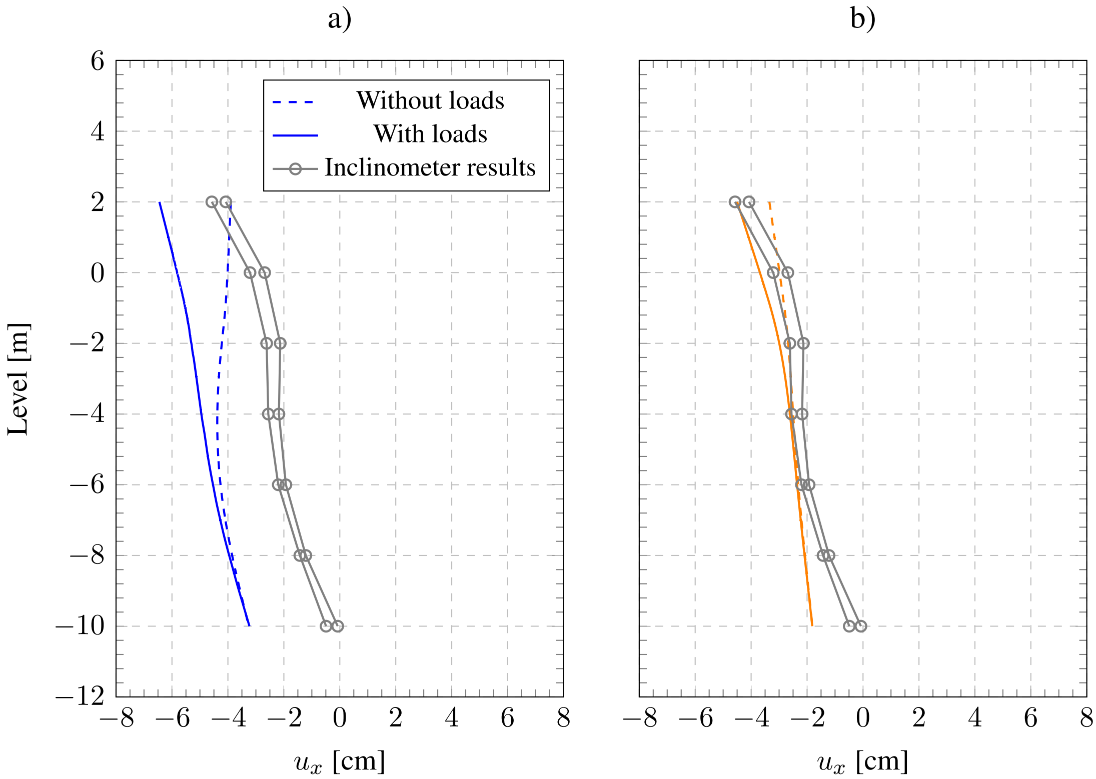

Figure 4.2: Cumulative horizontal displacement in the northern, outer sheet pile wall at the final stage in PLAXIS 2D, compared to inclinometer results. a) NGI-ADP, b) Creep-SCLAY1S.

Figure 4.3a shows the incremental displacements at different stages of the construction, using the NGI-ADP model. The greatest incremental displacements were obtained after stages which included excavations. For the top of the SPW the maximum incremental horizontal displacement was at stage 4, where local excavations in the fill material were carried out to level -0.8 m. For the bottom of the SPW the maximum incremental horizontal displacement was reached at stage 16, where excavation to level -5.18 m was carried out in the clay inside the northern elevator shaft. In stage 16 and 17, displacements in the positive x-direction (away from the excavation) occurred. For stage 16 this displacement occurred at the very top of the sheet pile wall, whereas for stage 17 it occurred from around an elevation of -1.2 meters to the bottom of the wall, although this displacement is very small.

The incremental displacement in the sheet pile wall at different stages using the Creep-SCLAY1S model are shown in Figure 4.3b. The predicted displacements are very different from when using the NGI-ADP model, showing much smaller displacements for most stages. Stage 3 has the largest displacement except at the very tip of the wall, where stage 6 reaches a slightly higher value of 1.2 cm. The displacement at stage 3 using Creep-SCLAY1S is very similar to when using NGI-ADP. This makes sense, since during this stage there is only excavation of the fill layer, which has the same values for both models. For the stages where excavation occurs in the clay layers there are much bigger deformations in the NGI-ADP model than in the Creep-SCLAY1S model, showcasing how different the strength of the clay is in between these models. Some construction stages had very similar deformations between the models whereas other had large differences, leading to the final deformations in the wall being so different in the end.

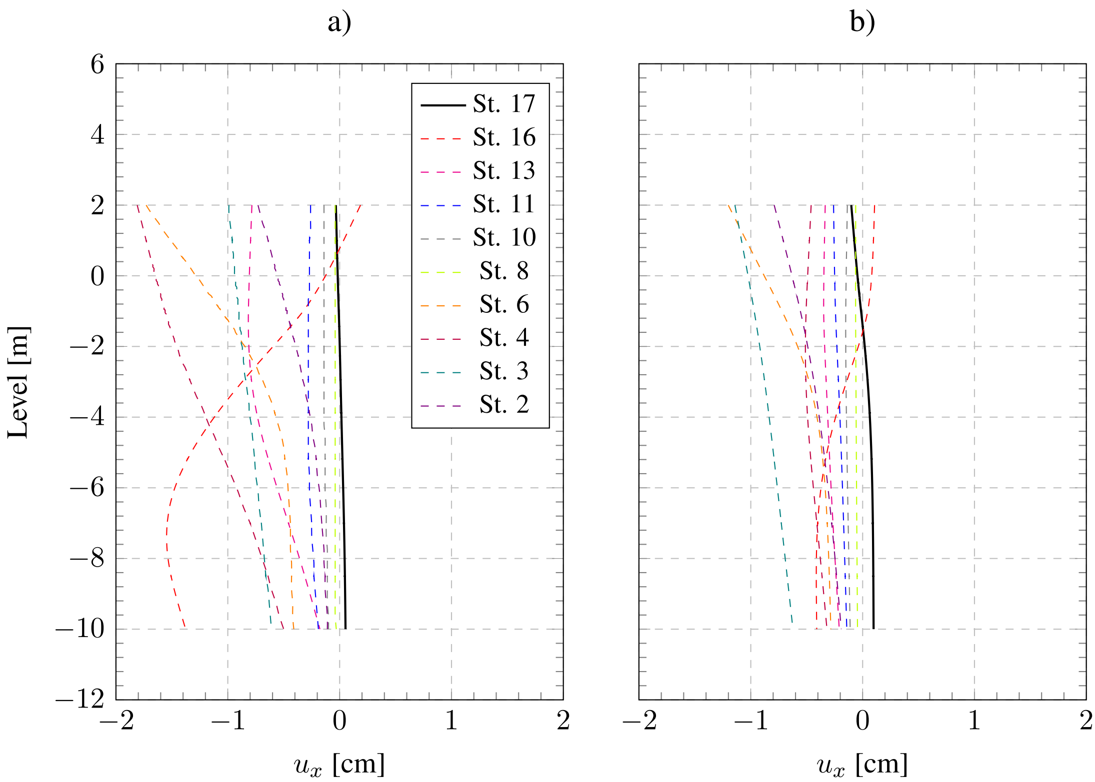

Figure 4.3: Development of the incremental horizontal displacement in the northern, outer sheet pile wall for stages of excavation in PLAXIS 2D with loads. a) NGI-ADP, b) Creep-SCLAY1S.

4.1.2 Bending moment in 2D

In Figure 4.4a, the bending moment for various construction stages, using the NGI-ADP model, are shown. Just like with the horizontal displacement, stage 16 and stage 17 show very similar results, indicating that the concrete casting at stage 17 had very little effect on the result. The maximum bending moment in the negative x-axis is around -25 kNm/m and in the positive x-axis it is 55 kNm/m, both occurring in stage 16 and stage 17. The maximum bending moment being reached at the final stages of the excavation is expected, because that is where the passive pressures from the soil is at its lowest, since that is where the most soil has been excavated. At this point, the active pressures acts over the maximum height. For many of the stages, the bending moment goes from negative to positive somewhere between -1 to -3 meters. The opposite is true however for stage 16 and 17 where the bending moment instead goes from positive to negative at an elevation of -2 meters.

In Figure 4.4b, the predicted bending moment for several construction stages, using the Creep-SCLAY1S model is shown. The bending moment occurs mostly in the positive direction, unlike the NGI-ADP simulation where the bending moment was mostly negative. This means that for a lot of the stages, the wall bends away from the excavation.

Once again, the maximum bending moment in the positive direction is happening at level -1, reaching a value of around 48 kNm/m.

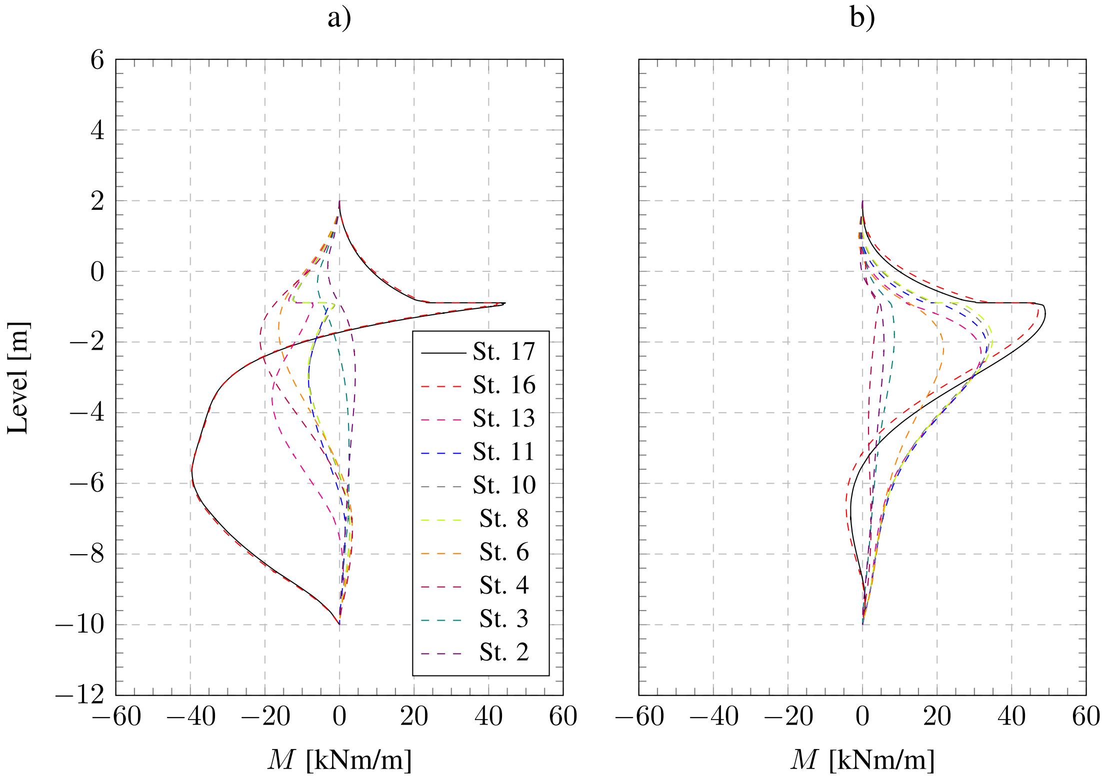

Figure 4.4: Development of the bending moment in the northern, outer sheet pile wall for stages of excavation in PLAXIS 2D with loads. a) NGI-ADP, b) Creep-SCLAY1S.

4.1.3 Shear forces in 2D

The shear forces across the entire sheet pile wall for various construction stages, using NGI-ADP, are displayed in Figure 4.5a. A positive sign value means that the soil is moving towards the excavation, and a negative sign means that the soil is moving away from the excavation. It can be seen that for most cases, the shear forces across the wall are both positive and negative, meaning that different parts of the wall are moving toward and away from the excavation, which explains the curved displacement of the wall. For each stage, the shear forces cross zero at the same point that the maximum bending moment was reached, which is to be expected.

The maximum and minimum shear forces are reached at stage 16 and 17, at a depth of -1m, with a maximum value of 70 kNm/m and a minimum value of -82 kNm/m. For both of these stages it can be seen that the shear force doesn't reach zero at the very bottom, which it does for all other stages. This signals that the bottom of the wall is resisting lateral movement at this stage. Since the shear force is the derivative of the bending moment, this means that the slope of the bending moment curve for these two last stages is non-zero, which can be seen in Figure 4.4a.

The shear forces for the last two stages are significantly larger than for the other stages, which is consistent with the bending moment being larger for these stages too. There is a very rapid increase of the shear force followed by a rapid decrease from stage 7 and onward. This rapid change from a maximum to a minimum value occurs at a depth of -0.89 meters, which is right where the concrete was cast. The concrete pushes against the wall, and to resist movement, the wall pushes back with a force that is equal to the force that the concrete is pushing with. The shear force at this depth is that force. For the last two stages, the shear force goes from approximately 70 kN/m to -80 kN/m.

In Figure 4.5b, the shear forces developed when using the Creep-SCLAY1S model are shown. Here, the shear forces generally increase as the excavation progresses, and the maximum and minimum values are reached at the last two stages, with stage 17 reaching a value of 50 kNm/ at level -1 m, and stage 16 and 17 reaching a value of -16 kNm/m at level -3 m. Here, there is also a rapid increase in shear force where the concrete was cast, but it does not go in the negative direction here.

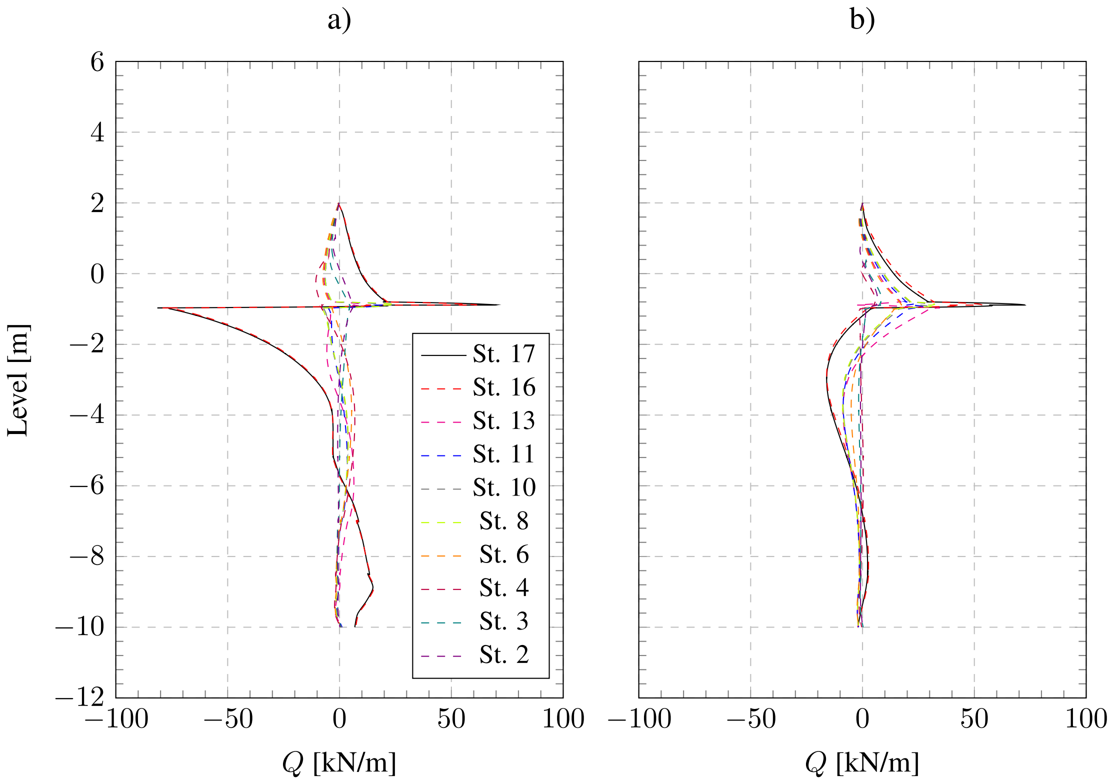

Figure 4.5: Development of the shear forces in the northern, outer sheet pile wall for stages of excavation in PLAXIS 2D with loads. a) NGI-ADP, b) Creep-SCLAY1S.

4.2 Results of the 3D analysis

The results of the 3D analysis for NGI-ADP and Creep-SCLAY1S are presented and discussed in this chapter.

4.2.1 Sensitivity analysis of I_2 and I_{12}

As explained in Chapter 3.6, a sensitivity analysis on the moment of inertia around the second axis, I_2, was performed. The results of this sensitivity analysis are shown in Figure 4.6a. The results show that the difference between using a value of I_2 that is 20 times smaller than I_1 and using a value of I_2 that is 1000 times smaller than I_1 only has a very small effect on the horizontal displacement of the sheet pile wall. The difference is around 1 millimeter at the top of the sheet pile wall, and further down in the clay there is barely any difference. Another analysis was also done, by dividing I_1 with 10000 to get a value for I_2, and the difference to dividing with 1000 is miniscule. Because of this, it was decided that further research on determining an appropriate value of I_2 would not be conducted in this thesis.

A sensitivity analysis of I_{12} was also performed, also shown in Figure 4.6b, and here it can also be seen that using a value of I_{12} that is 1000 and 10000 times smaller than I_1 rather than a value that is 10 times smaller than I_1 barely had an effect on the horizontal displacement of the sheet pile wall.

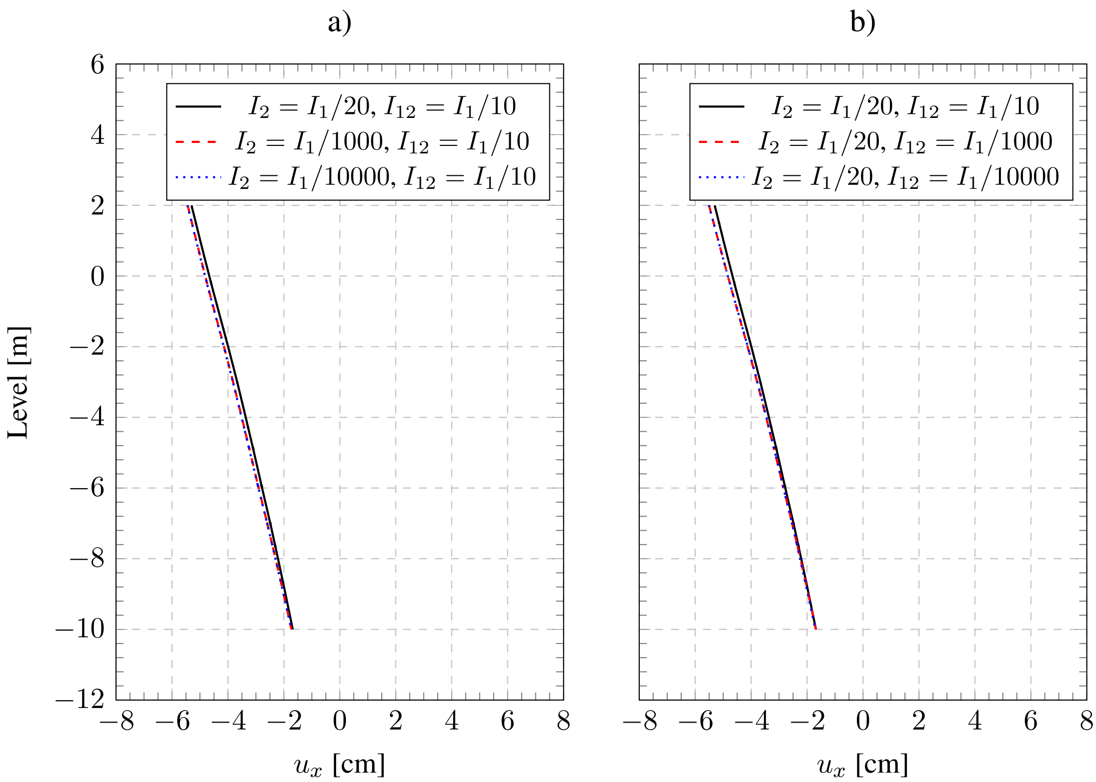

Figure 4.6: Sensitivity study of the second moment of inertia for the cumulative horizontal displacement in the northern, outer sheet pile wall in PLAXIS 3D, using the NGI-ADP model with loads. a) I_2 sensitivity study, b) I_{12} sensitivity study.

4.2.2 Horizontal displacement in 3D

The horizontal displacement of the sheet pile wall, using the NGI-ADP model, is shown in Figure 4.7a. The maximum cumulative horizontal displacement of 5.3 cm was reached at the top of the wall in the last two stages. Just like in the 2D simulations, the concrete casting that happens in the last stage had no effect on the displacement of the wall. The last two stages show a very straight and even displacement across the entire wall, whereas the earlier stages experienced more of a curved displacement.

In Figure 4.7b, the cumulative horizontal displacement of the sheet pile wall, using the Creep-SCLAY1S model is plotted. It's highest displacement was reached at the top of the wall at the last stage of the construction, with a displacement of 2.8 cm, making it much smaller than the displacement of the NGI-ADP simulation.

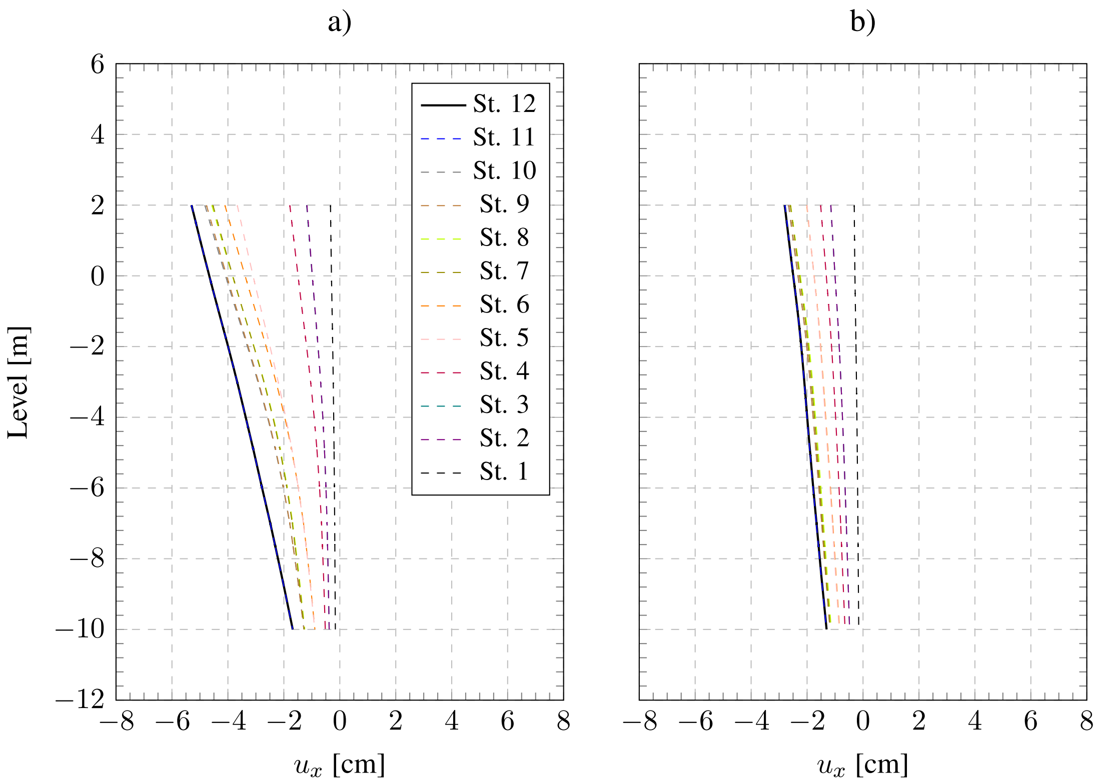

Figure 4.7: Development of the cumulative horizontal displacement in the northern, outer sheet pile wall for stages of excavation in PLAXIS 3D with loads. a) NGI-ADP, b) Creep-SCLAY1S.

The incremental displacement of the wall for each stage is shown in Figure 4.8a. The maximum displacement happened at stage 5, resulting in the top of the wall moving almost 2 cm toward the excavation. During this stage almost half the construction site was excavated from level +0.5 m to level -0.97 m. This stage is a simplification, since it represents several local excavations that have been combined into one stage, which explains why the displacements are much larger for this stage. Stage 11 also saw large displacements further down the wall, which is to be expected since that is where the deep elevator shaft was excavated to level -5.18 m. It is this stage that is responsible for straightening out the wall, removing the curved shape it hade in the earlier stages. Unlike the 2D simulations, all of the displacements occurred toward the excavation, rather than away from it. By looking at the graph it becomes clear that the largest displacements occur during excavations. In the graph it can also be seen that the last stage had zero effect on the displacement of the wall. Stage 11 has a very bent shape of the displacement. This is probably due to the waler holding the wall back toward the top, while the middle of the wall is only kept in place because of the soil on the passive side, some of which is excavated in the deep elevator shaft during this stage.

In Figure 4.8b, the incremental displacement of the sheet pile wall is displayed, using the Creep-SCLAY1S model. Here, stage 2 had the biggest horizontal displacement, with a displacement of 0.84 cm at the top of the wall. During this stage there is an excavation to +1 meters. Stage 7 also resulted in large displacements. It seems that this model is more sensitive to excavations happening further away from the wall, than the NGI-ADP model is. Comparing the two models, it becomes apparent how much stronger the soil is with the Creep-SCLAY1S model. This is especially visible during stage 11, where the difference in displacement at the top and middle of the wall is fairly small, showing that the waling beam is less necessary here.

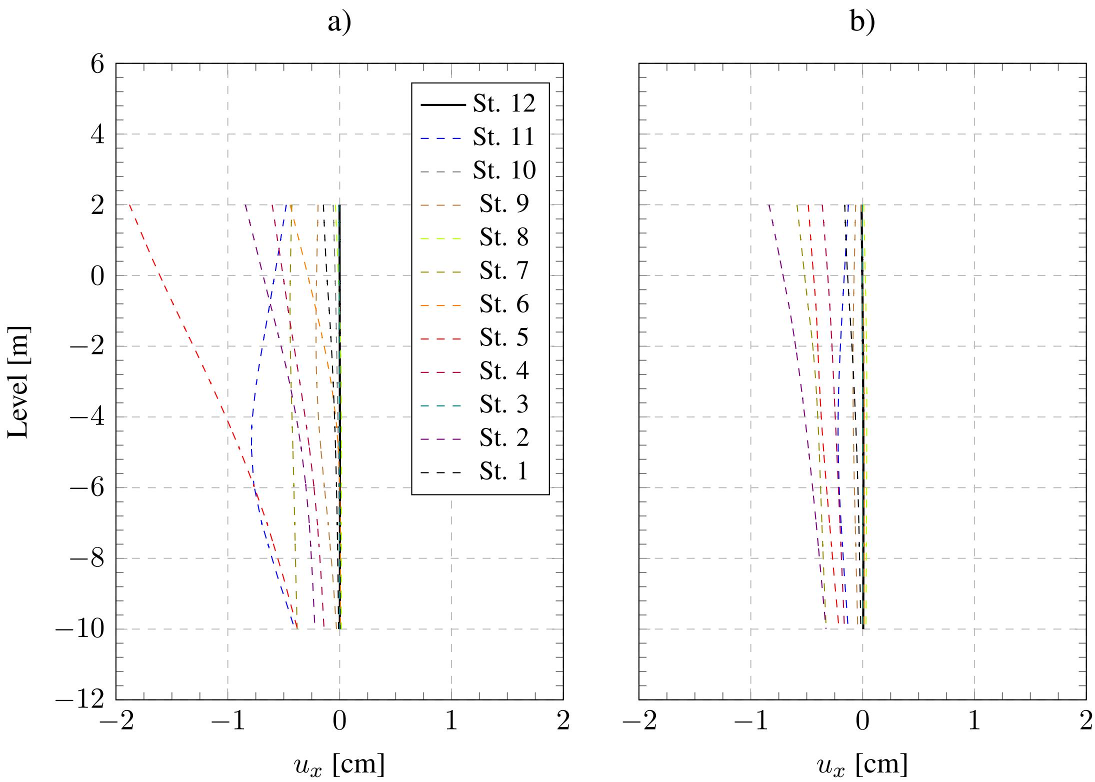

Figure 4.8: Development of the incremental horizontal displacement in the northern, outer sheet pile wall for stages of excavation in PLAXIS 3D with loads. a) NGI-ADP, b) Creep-SCLAY1S.

A comparison of the 2D- and 3D-simulations, together with the maximum and minimum inclinometer readings that was obtained during a 1-month period after the can be seen in Figure 4.9. The graph shows that although the 2D-results for the NGI-ADP simulations more closely matches the curved shape of the inclinometer readings, the 2D results overestimate the horizontal displacement of the sheet pile wall, compared to the 3D results that are closer to the real life inclinometer readings. However, the results obtained during 2D analysis using Creep-SCLAY1S are actually more similar to the inclinometer readings, than the 3D results are when using NGI-ADP, except for around level -9 and downward, where the 3D results are slightly more correct.

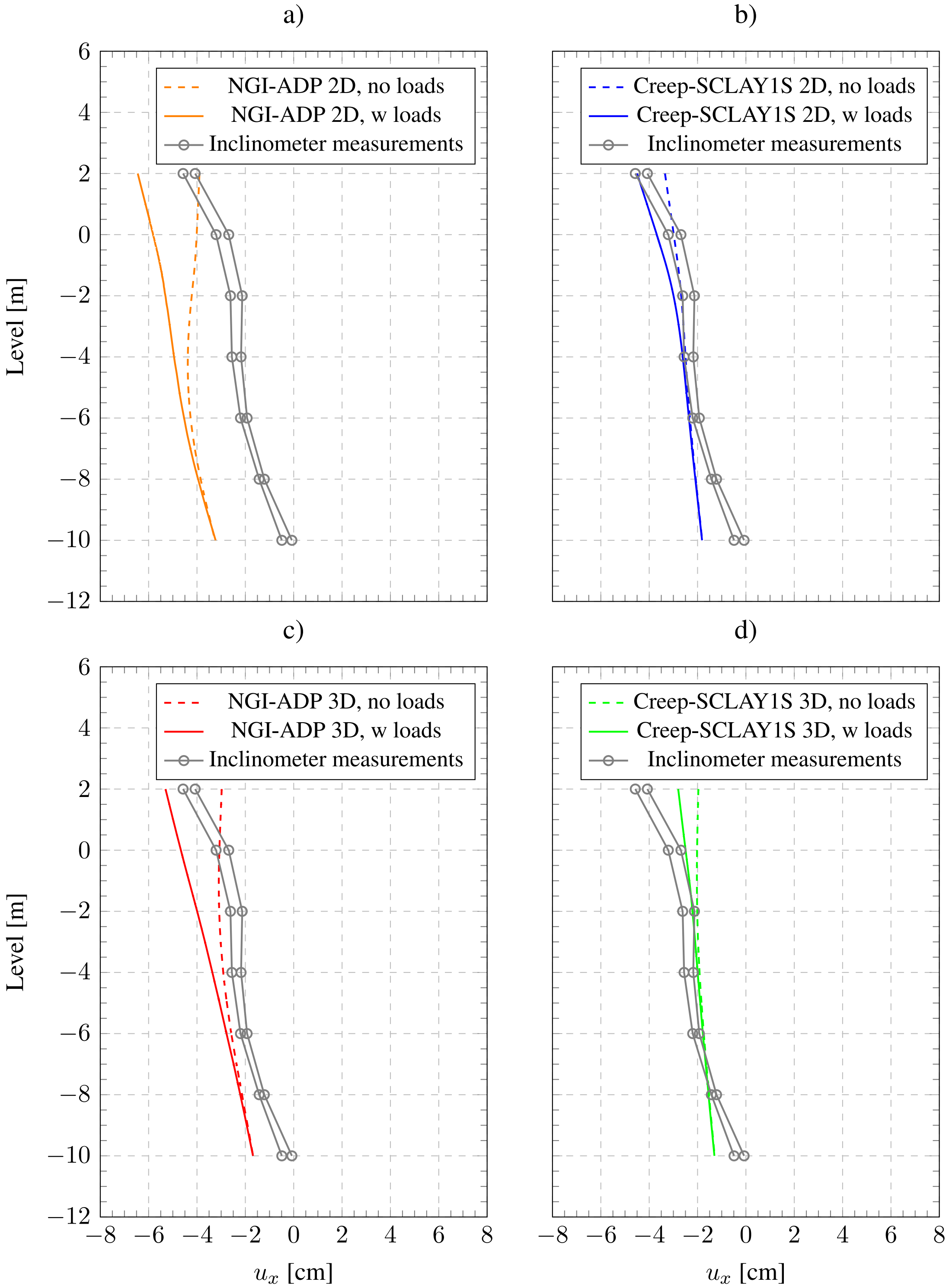

Figure 4.9: Cumulative horizontal displacement in the northern, outer sheet pile wall at the final stage using the NGI-ADP and Creep-SCLAY1S models with and without loads in PLAXIS 2D and 3D, compared to inclinometer results.

4.2.3 Bending moment in 3D

As explained previously, during 3D analysis, the bending moment acts in 3 directions. Only bending moment M_{11} will be analyzed here, since it corresponds with the bending moment that is analyzed in 2D-modelling. The bending moment, using NGI-ADP is shown in Figure 4.10a The bending moment reaches its maximum value in the positive direction, at a depth of 4.5 meters during stage 8, with a value of 22 kNm. In the negative direction (toward the excavation), the maximum bending moment is reached near the top of the excavation, at level +0, which is where it is expected to occur. It can be seen that for the positive bending moment, it decreases during stage 10, which is thanks to the waling beams providing support. What is interesting here is that the maximum and minimum bending moments are not reached during the last stages, but rather during stage 8 and 9. The maximum bending moment should occur when the wall is experiencing the least support, which in the 2D-simulations happened at the last stages. This could be because of the installation of the waling beams in the deep elevator shaft could be modelled realistically in the 3D-model, as opposed to the 2D-model where it was simplified. However, the bending moment reaching 0 for the last two stages at level -4.8, and then sharply bouncing back, seems very unrealistic and is probably due to some numerical error.

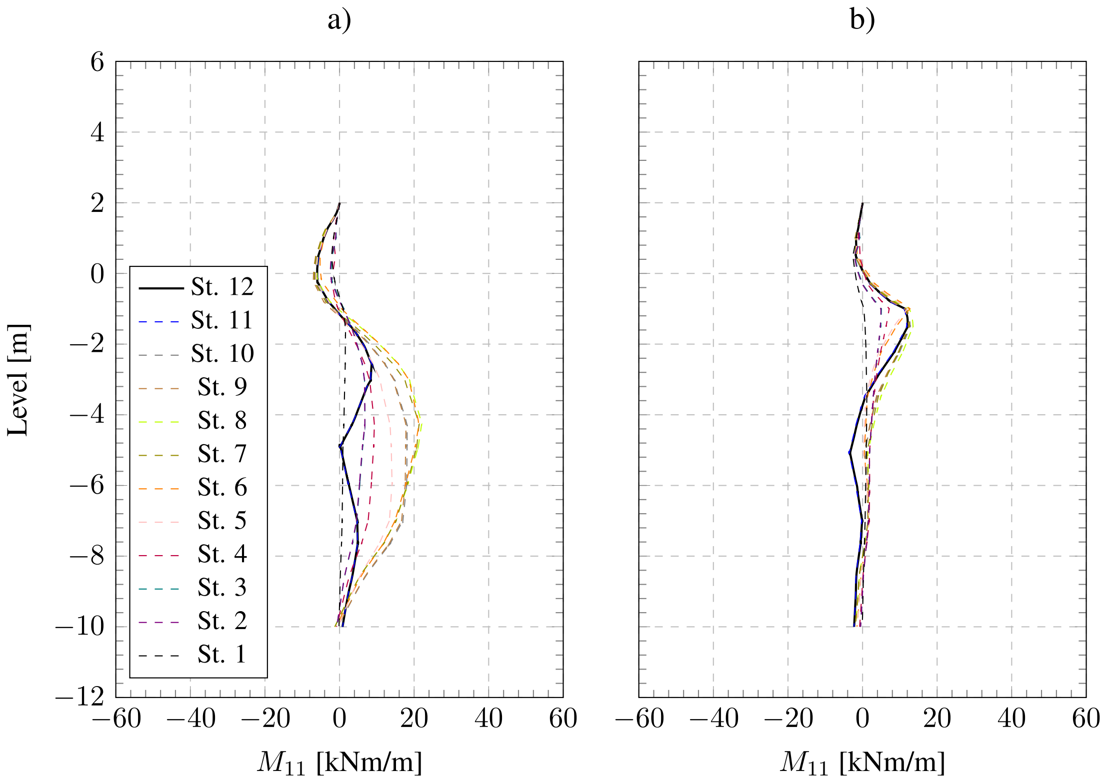

Figure 4.10: Development of the bending moment in the northern, outer sheet pile wall for stages of excavation in PLAXIS 3D with loads. a) NGI-ADP, b) Creep-SCLAY1S.

The bending moment for the sheet pile wall, using the Creep-SCLAY1S model, is shown in Figure 4.10b. The maximum value in the positive direction is once again reached during stage 8, but this time at a depth of 1.5 meters, reaching a value of 16 kNm. Just like with the NGI-ADP simulation, the maximum bending moment in the positive direction is not reached at the last stage, but the maximum bending moment in the negative direction is actually reached at the last stage.

4.2.4 Shear forces in 3D

The shear forces for all the construction stages, using NGI-ADP, are shown in Figure 4.11a. As explained in Chapter 2.3.14, it is shear force Q_{13} that is of interest here, since it corresponds with the shear forces developing in 2D analysis. The shear forces coincide fairly well with bending moment M_{11}, crossing zero at around the same point as the local minima and maxima of the bending moment occur. Just like with the bending moment, the shear forces in the last two stages act differently than the the other stages, with a local minima being reached at level -4.2. The first stage experiences much less shearing than the other stages, being around zero from around -2 meters and downward. Once the excavations start, during stage 2, soil heaving occurs and the shearing increases significantly.

The shear forces for all the construction stages, using Creep-SCLAY1S, are shown in Figure 4.11b. The shear forces are significantly smaller than for the 2D analyses. This could be because of the fact that in a 3D analysis, the stresses can be redistributed in all directions, so the forces are not as concentrated as in 2D. The corner effects simulated in 3D allow the stresses to escape through the corner strut, and the soil can move around the edge of the wall instead of pushing against it. These effects are not present in 2D, because the wall extends infinitely. For the 3D analysis there is also a clear increase in shear force where the concrete was cast, but it is not as rapid as in 2D. This is most likely because there was no plate in the middle of the concrete.

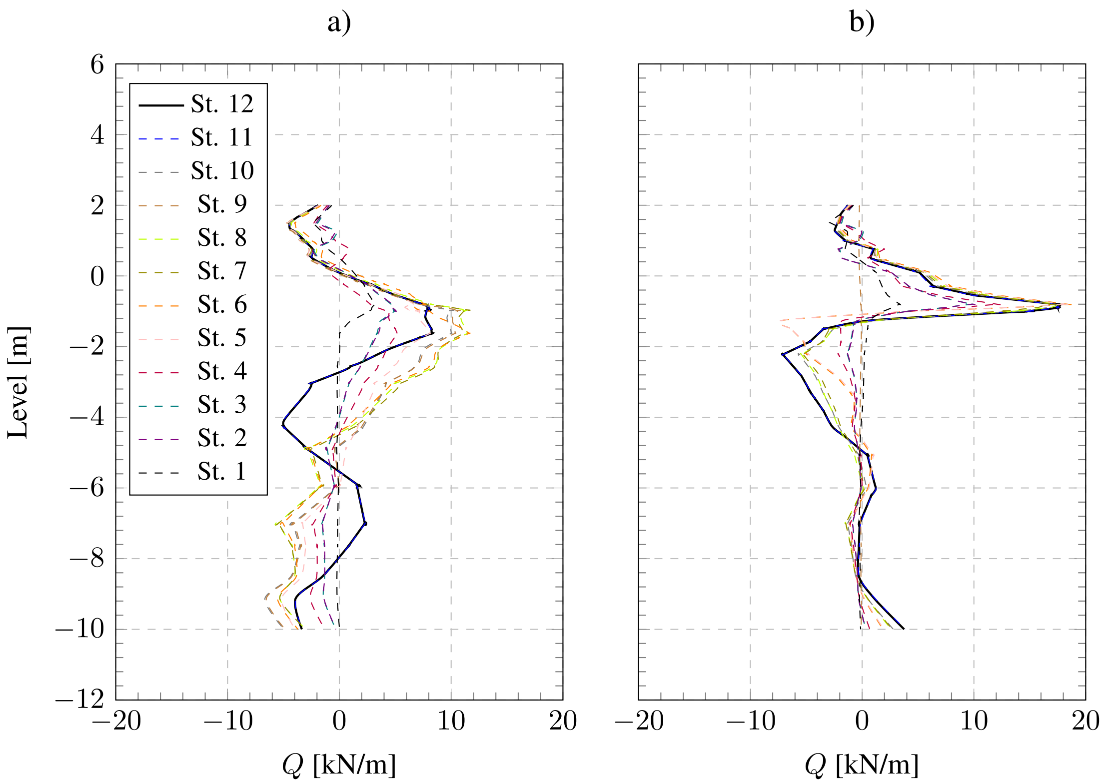

Figure 4.11: Development of the shear forces in the northern, outer sheet pile wall for stages of excavation in PLAXIS 3D with loads. a) NGI-ADP. b) Creep-SCLAY1S

5 Conclusions

The obtained results confirmed what has been shown in earlier research, namely that numerical modelling in PLAXIS 2D sometimes will give significantly different results than the same construction site being modelled in PLAXIS 3D. A 2D analysis will result in predictions of larger deformations and can therefore overestimate the movement of retaining walls in complex geometries that are not well represented with a plane strain model, at least when using the same constitutive model.

However, the results are also highly dependent on the choice of constitutive model, with a 2D simulation of Creep-SCLAY1S performing better in terms of representing reality, compared to NGI-ADP in 3D. Even though the sheet pile walls were modelled the exact same in the two 2D-simulations, there were still significant differences in the horizontal displacement of the wall, as well as in the bending moment, and the shear forces in the wall. This highlights how important the choice of constitutive model is, and how the parameters put into the soil models can affect the results. A more advanced soil model like Creep-SCLAY1S captures the behavior of the clay more accurately than a simpler soil model like NGI-ADP. Using the wrong model can lead to inaccurate and overestimated results.

The choice of I_2 and I_{12} will only have a very small effect on the displacement of the sheet pile wall, meaning that the PLAXIS manuals recommended determination of these parameters are sufficient. Using a much smaller value is not necessary in most cases. As long as I_2 and I_{12} are significantly smaller than I_1, the values are good enough.

Adding loads into the model resulted in a significantly larger deformation of the sheet pile wall as opposed to when loads were not present. When no loads were present, the deformation of the wall ended up with a shape that was very different from the real world deformation. The loads made the biggest difference further up the wall, while further down the impact was smaller. For this study, the construction had already taken place and some limited information was available on where loads were placed, but for construction projects that have not begun yet it is important to think about where machines will be placed in order to correctly place the loads in the model to get an accurate deformation of the soil and structural elements.

6 References

Amavasai, A., Sivasithamparam, N., Dijkstra, J., & Karstunen, M. (2018). Consistent Class A & C predictions of the Ballina test embankment. *Computers and Geotechnics*, *93*, 75–86. `https://doi.org/10.1016/j.compgeo.2017.05.025`

ArcelorMittal. (2022). General catalogue 2022: Metric & imperial edition.

Bentley Systems, I. (2025a). PLAXIS 2D - Materials Models Manual.

Bentley Systems, I. (2025b). PLAXIS 2D - Reference Manual.

Bentley Systems, I. (2025c). PLAXIS 3D - Materials Models Manual.

Bentley Systems, I. (2025d). PLAXIS 3D - Reference Manual.

Bilgin, Ö. (2010). Numerical studies of anchored sheet pile wall behavior constructed in cut and fill conditions. *Computers and Geotechnics*, *37*(3), 399–407. `https://doi.org/10.1016/j.compgeo.2010.01.002`

Ehrmanntraut, E., Wersäll, C., & Massarsch, K. R. (2021). Soil identification by vibration measurements during dynamic penetration testing : A field study. *:*

Finno, R. J., Blackburn, J. T., & Roboski, J. F. (2007). Three-Dimensional Effects for Supported Excavations in Clay. *Journal of Geotechnical and Geoenvironmental Engineering*, *133*(1), 30–36. `https://doi.org/10.1061/(ASCE)1090-0241(2007)133:1(30)`

Grimstad, G., Andresen, L., & Jostad, H. P. (2012). NGI-ADP: Anisotropic shear strength model for clay. *International Journal for Numerical and Analytical Methods in Geomechanics*, *36*(4), 483–497. `https://doi.org/10.1002/nag.1016`

Karstunen, M., & Amavasai, A. (2017). BEST SOIL: Soft soil modelling and parameter determination. *Chalmers University of Technology, Department of Architecture and Civil Engineering*.

Karstunen, M., Krenn, H., Wheeler, S. J., Koskinen, M., & Zentar, R. (2005). Effect of anisotropy and destructuration on the behavior of Murro test embankment. *International Journal of Geomechanics*, *5*(2), 87–97. `https://doi.org/10.1061/(ASCE)1532-3641(2005)5:2(87)`

Knappett, J., & Craig, R. (2012, February). *Craig's soil mechanics* (Eight). Spon Press.

Lees, A. (2016, January). *Geotechnical finite element analysis: A practical guide*. ICE Publishing. `https://doi.org/10.1680/gfea.60876`

Persson, H., & Sigström, D. (2010, June). *Staged excavation in soft clay supported by a cantilever sheet pile wall - Numerical analysis and field measurements of the effect of a wailing beam* (tech. rep.). Chalmers University of Technology. Gothenburg.

Potts, D. M. (1999, January). *Finite element analysis in geotechnical engineering: Volume One - Theory*. Emerald Publishing Limited. `https://doi.org/10.1680/feaiget.27534`

Sällfors, G. (1975). *Preconsolidation Pressure of Soft, High-Plastic Clays* [Doctoral Thesis]. Chalmers University of Technology.

Sällfors, G. (2013). *Geoteknik* (5:e upplagan).

SGF. (2009). *Metodbeskrivning för provtagning med standardkolvprovtagare - Ostörd provtagning i finkornig jord* (tech. rep. No. 1:2009). Svenska Geotekniska Föreningen. Linköping.

Sivasithamparam, N., Karstunen, M., & Bonnier, P. (2015). Modelling creep behaviour of anisotropic soft soils. *Computers and Geotechnics*, *69*, 46–57. https://doi.org/10.1016/j.compgeo.2015.04.015

Svenska Institutet för Standarder. (1991, September). Standard - Geotekniska provningsmetoder - Kompressionsegenskaper - Ödometerförsök, CRS-försök - Kohesionsjord SS 27126.

Tornborg, J., Karlsson, M., Kullingsjö, A., & Karstunen, M. (2021). Modelling the construction and long-term response of Göta Tunnel. *Computers and Geotechnics*, *134*, 104027. https://doi.org/10.1016/j.compgeo.2021.104027

Trafikverket. (2025). Geokonstruktion: Dimensionering och utformning (TRVINFRA-00230, version 3.0).

U.S. Army Corps of Engineers (Department of the Army). (1994, March). *Engineering and Design: Design of Sheet Pile Walls*.

Wang, Z., Zhu, J., & Ma, T. (2024). Review on monitoring of pavement subgrade settlement: Influencing factor, measurement and advancement. *Measurement*, *237*, 115225. https://doi.org/10.1016/j.measurement.2024.115225

Wood, D. M. (2004, July). *Geotechnical modelling*. CRC Press.

Zhang, X., Chen, Z., & Liu, Y. (2017). Chapter 6 - constitutive models. In X. Zhang, Z. Chen, & Y. Liu (Eds.), *The material point method* (pp. 175–219). Academic Press. https://doi.org/10.1016/B978-0-12-407716-4.00006-5

Appendix A

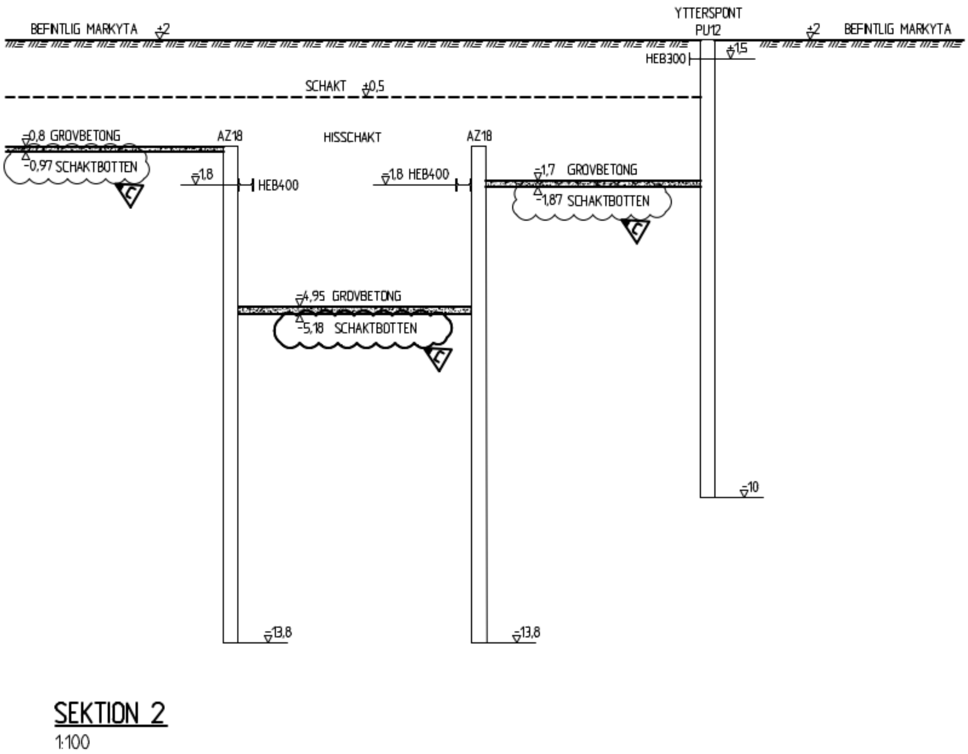

Figure A.1: Cross-section 2

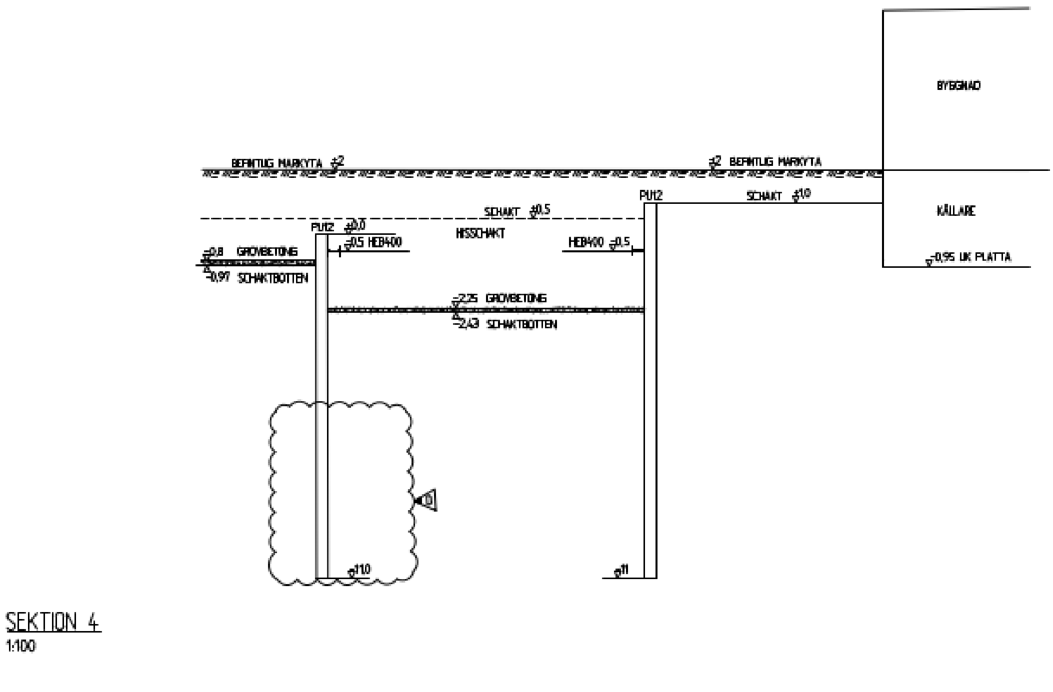

Figure A.2: Cross-section 4

Appendix B

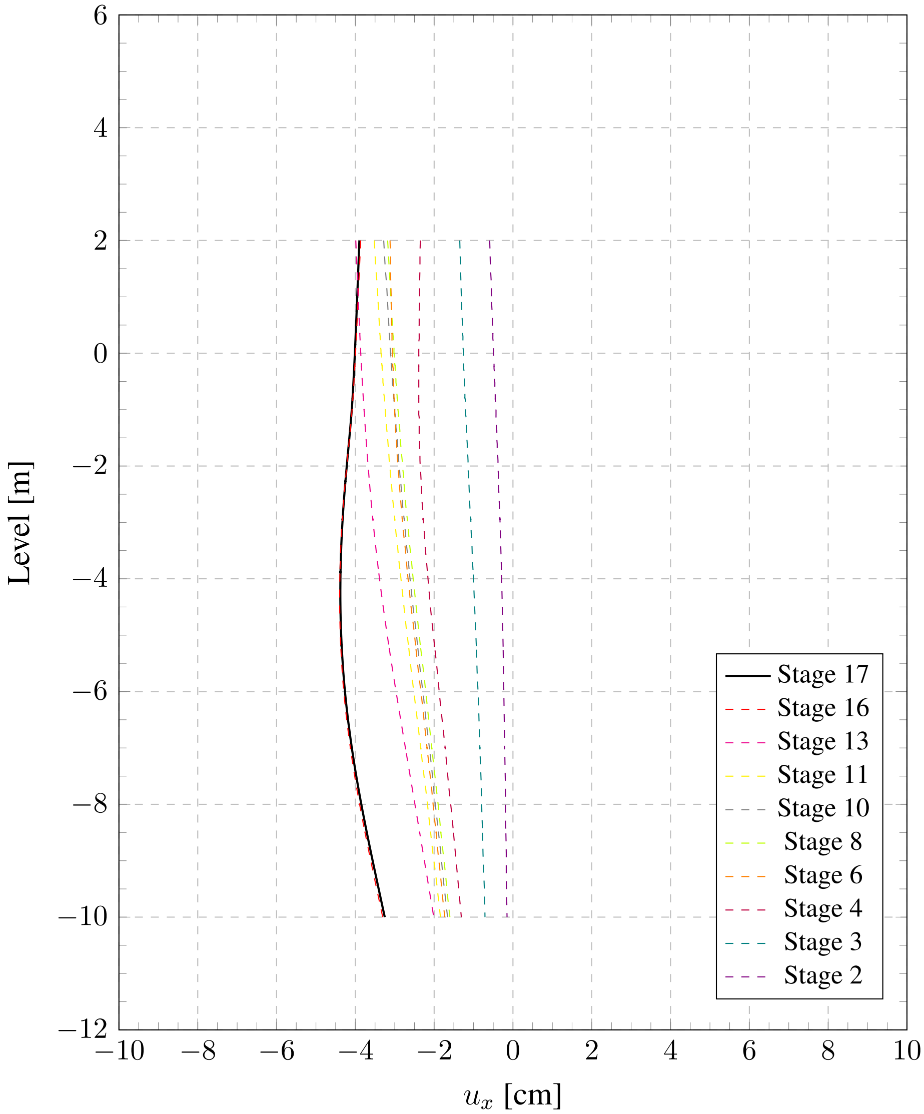

Figure B.1: Development of the cumulative horizontal displacement in the northern, outer sheet pile wall for stages of excavation using the NGI-ADP model without loads in 2D.

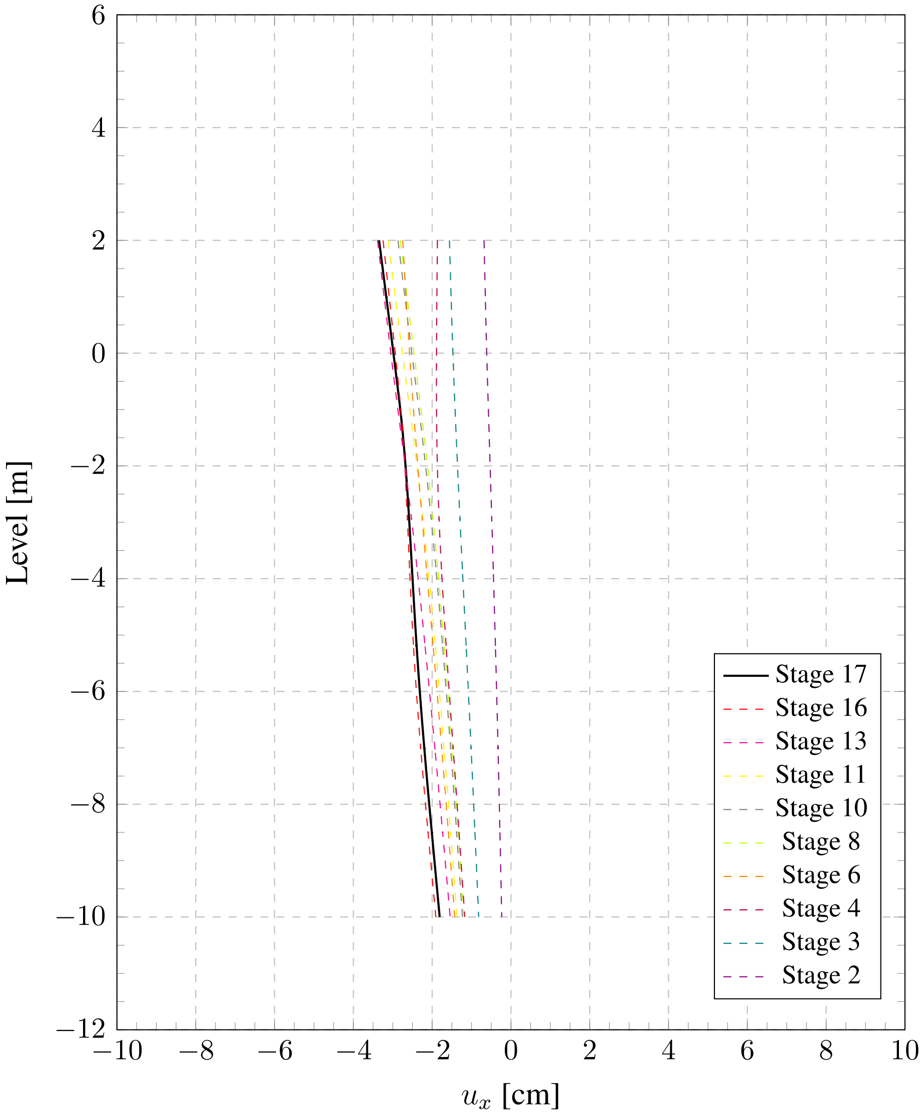

Figure B.2: Development of the cumulative horizontal displacement in the northern, outer sheet pile wall for stages of excavation using the Creep-SCLAY1S model without loads in 2D.

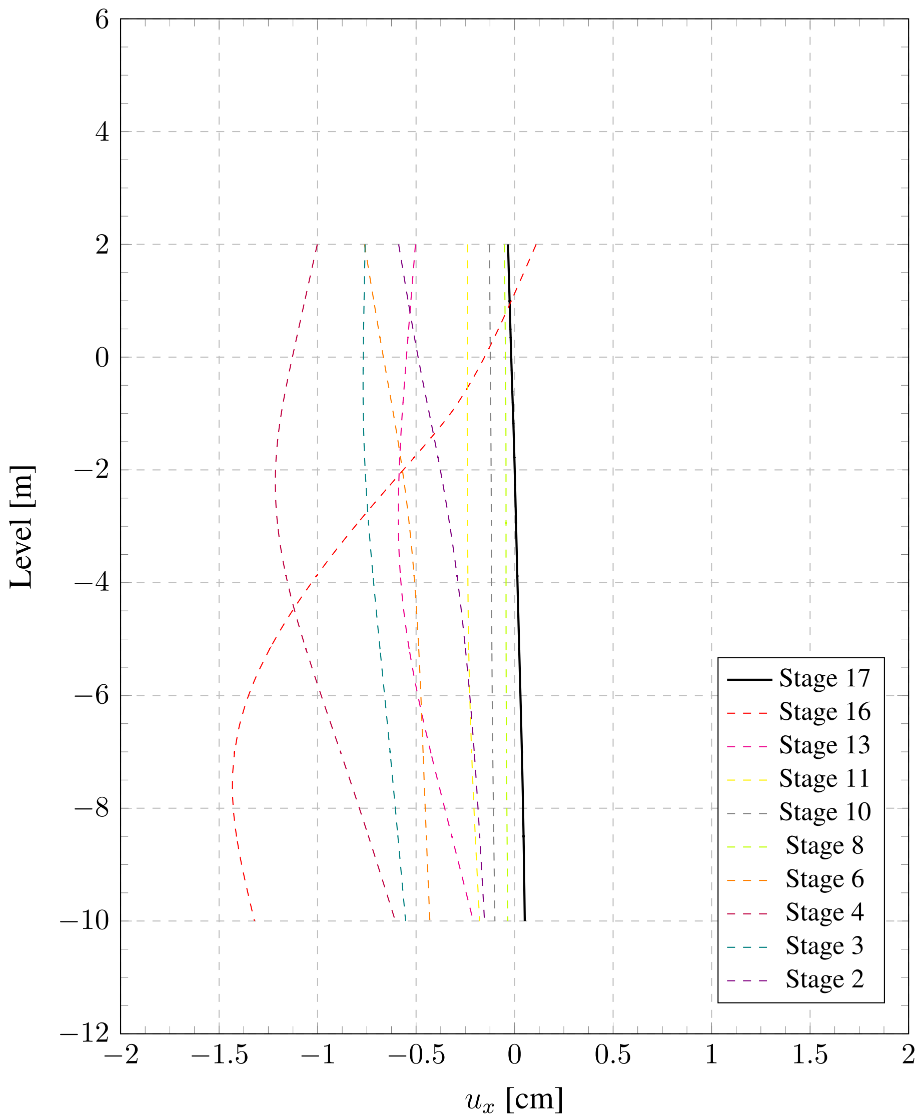

Figure B.3: Development of the incremental horizontal displacement in the northern, outer sheet pile wall for stages of excavation using the NGI-ADP model without loads in 2D.

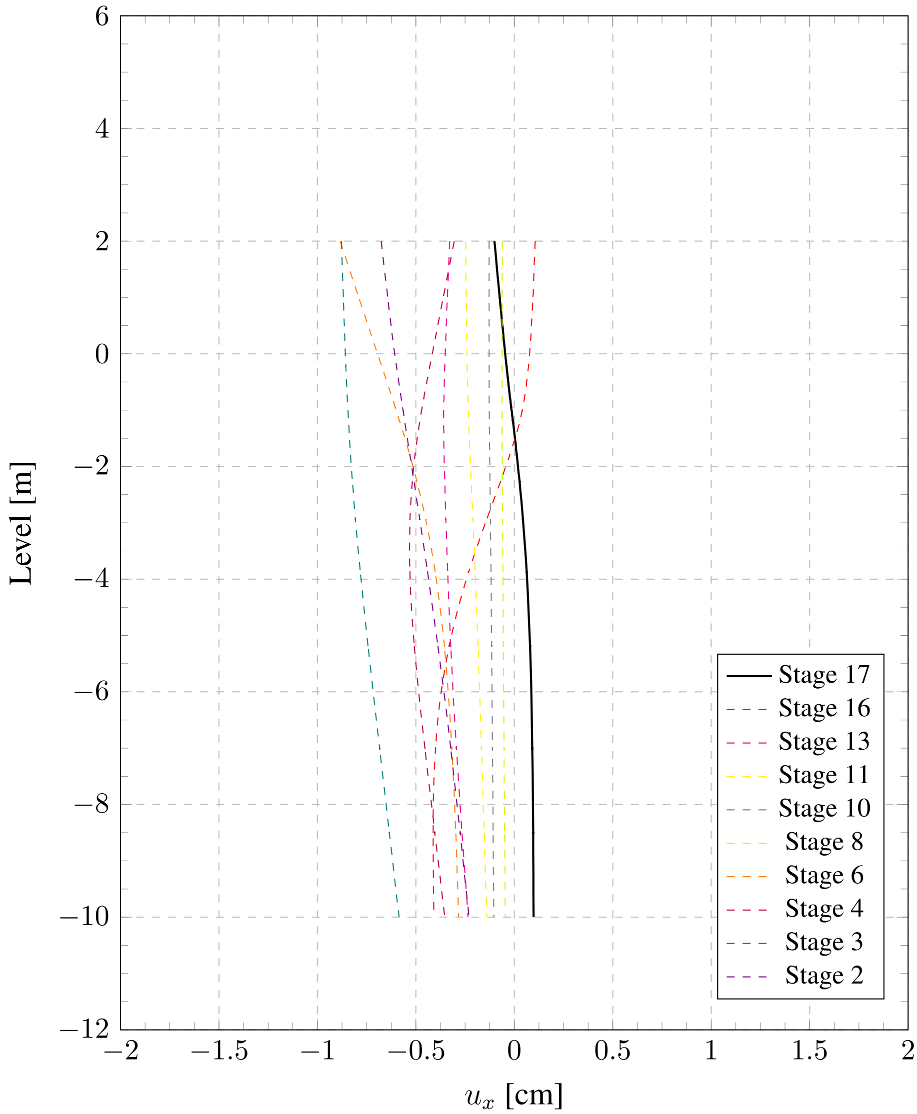

Figure B.4: Development of the incremental horizontal displacement in the northern, outer sheet pile wall for stages of excavation using the Creep-SCLAY1S model without loads in 2D.

Appendix C

Equivalent wall in 3D

AZ18

$$v_{steel} := 0.3$$

$$E_{steel} := 2.1 \cdot 10^{8} \ \frac{kN}{m^2}$$ Young's modulus for steel

$$A_{c.AZ18} := 150.4 \ \frac{cm^2}{m} = 0.015 \ \frac{m^2}{m}$$ Cross sectional area of AZ18 per meter

$$I_{1.AZ18} := 34200 \ \frac{cm^4}{m} = \left(3.42 \cdot 10^{-4}\right) \frac{m^4}{m}$$ Area moment of inertia for AZ18 per meter

$$E_{steel} \cdot I_{1.AZ18} = 71820 \ \frac{kN \cdot m^2}{m}$$ Flexural rigidity for AZ18 per meter

$$E_{steel} \cdot A_{c.AZ18} = \left(3.158 \cdot 10^{6}\right) \frac{kN}{m}$$ Axial stiffness for AZ18 per meter

Equivalent thickness of a rectangular cross section

$$d_{eq.AZ18} := \sqrt{\frac{12 \cdot E_{steel} \cdot I_{1.AZ18}}{E_{steel} \cdot A_{c.AZ18}}} = 0.522 \ m$$

Equivalent Young's modulus of a rectangular cross section

$$E_{1.eq.AZ18} := \frac{12 \cdot E_{steel} \cdot I_{1.AZ18}}{d_{eq.AZ18}^{\ 3}} = \left(6.046 \cdot 10^{6}\right) \frac{kN}{m^2} \qquad E_{2.eq.AZ18} := \frac{E_{1.eq.AZ18}}{20} = \left(3.023 \cdot 10^{5}\right) \frac{kN}{m^2}$$

Equivalent area moment of inertia per meter of a rectangular cross section

$$I_{1.eq.AZ18} := \frac{1 \ m \cdot d_{eq.AZ18}^{\ 3}}{12 \cdot 1 \ m} = 0.012 \ \frac{m^4}{m}$$

$$I_{2.eq.AZ18} := \frac{I_{1.eq.AZ18}}{20} = \left(5.939 \cdot 10^{-4}\right) \frac{m^4}{m}$$

$$I_{12.eq.AZ18} := \frac{I_{1.eq.AZ18}}{10} = \left(1.188 \cdot 10^{-3}\right) \frac{m^4}{m}$$

Check

$$E_{steel} \cdot I_{1.AZ18} = 71820 \ \frac{kN \cdot m^2}{m}$$

$$E_{1.eq.AZ18} \cdot I_{1.eq.AZ18} = 71820 \ \frac{kN \cdot m^2}{m}$$

Equivalent shear modulus of a rectangular cross section

$$I_{12.AZ18} := \frac{I_{1.AZ18}}{10} = \left(3.42 \cdot 10^{-5}\right) \frac{m^4}{m}$$

$$G_{12.eq.AZ18} := \frac{6 \cdot E_{steel} \cdot I_{12.AZ18}}{\left(1 + v_{steel}\right) d_{eq.AZ18}^{\ 3}} = \left(2.325 \cdot 10^{5}\right) \frac{kN}{m^2}$$

$$A_{13.AZ18} := \frac{A_{c.AZ18}}{3} = \left(5.013 \cdot 10^{-3}\right) \frac{m^2}{m}$$

$$G_{13.eq.AZ18} := \frac{E_{steel} \cdot A_{13.AZ18}}{2 \left(1 + v_{steel}\right) \cdot d_{eq.AZ18}} = \left(7.752 \cdot 10^{5}\right) \frac{kN}{m^2}$$

$$A_{23.AZ18} := \frac{A_{c.AZ18}}{10} = \left(1.504 \cdot 10^{-3}\right) \frac{m^2}{m}$$

$$G_{23.eq.AZ18} := \frac{E_{steel} \cdot A_{23.AZ18}}{2 \left(1 + v_{steel}\right) d_{eq.AZ18}} = \left(2.325 \cdot 10^{5}\right) \frac{kN}{m^2}$$

Figure C.1: Calculation of input parameters for sheet pile wall AZ18.

PU12

$E_{steel} = (2.1 \cdot 10^8)\ \frac{kN}{m^2}$ Young's modulus for steel

$A_{c.PU12} := 140\ \frac{cm^2}{m} = 0.014\ \frac{m^2}{m}$ Cross sectional area of PU12 per meter

$I_{1.PU12} := 21600\ \frac{cm^4}{m} = (2.16 \cdot 10^{-4})\ \frac{m^4}{m}$ Area moment of inertia for PU12 per meter

$E_{steel} \cdot I_{1.PU12} = 45360\ \frac{kN \cdot m^2}{m}$ Flexural rigidity for PU12 per meter

$E_{steel} \cdot A_{c.PU12} = (2.94 \cdot 10^6)\ \frac{kN}{m}$ Axial stiffness for PU12 per meter

Equivalent thickness of a rectangular cross section

$$d_{eq.PU12} := \sqrt{\frac{12 \cdot E_{steel} \cdot I_{1.PU12}}{E_{steel} \cdot A_{c.PU12}}} = 0.43\ m$$

Equivalent Young's modulus of a rectangular cross section

$$E_{1.eq.PU12} := \frac{12 \cdot E_{steel} \cdot I_{1.PU12}}{d_{eq.PU12}^{\ 3}} = (6.833 \cdot 10^6)\ \frac{kN}{m^2} \qquad E_{2.eq.PU12} := \frac{E_{1.eq.PU12}}{20} = (3.416 \cdot 10^5)\ \frac{kN}{m^2}$$

Equivalent area moment of inertia per meter of a rectangular cross section

$$I_{1.eq.PU12} := \frac{1\ m \cdot d_{eq.PU12}^{\ 3}}{12 \cdot 1\ m} = (6.639 \cdot 10^{-3})\ \frac{m^4}{m}$$

$$I_{2.eq.PU12} := \frac{I_{1.eq.PU12}}{20} = (3.319 \cdot 10^{-4})\ \frac{m^4}{m}$$

$$I_{12.eq.PU12} := \frac{I_{1.eq.PU12}}{10} = (6.639 \cdot 10^{-4})\ \frac{m^4}{m}$$

Check

$E_{steel} \cdot I_{1.PU12} = 45360\ \frac{kN \cdot m^2}{m}$

$E_{1.eq.PU12} \cdot I_{1.eq.PU12} = 45360\ \frac{kN \cdot m^2}{m}$

Equivalent shear modulus of a rectangular cross section

$$I_{12.PU12} := \frac{I_{1.PU12}}{10} = (2.16 \cdot 10^{-5})\ m^3$$

$$G_{12.eq.PU12} := \frac{6 \cdot E_{steel} \cdot I_{12.PU12}}{(1 + v_{steel}) \cdot d_{eq.PU12}^{\ 3}} = (2.628 \cdot 10^5)\ \frac{kN}{m^2}$$

$$A_{13.PU12} := \frac{A_{c.PU12}}{3} = (4.667 \cdot 10^{-3})\ \frac{m^2}{m}$$

$$G_{13.eq.PU12} := \frac{E_{steel} \cdot A_{13.PU12}}{2\ (1 + v_{steel}) \cdot d_{eq.PU12}} = (8.76 \cdot 10^5)\ \frac{kN}{m^2}$$

$$A_{23.PU12} := \frac{A_{c.PU12}}{10} = (1.4 \cdot 10^{-3})\ m$$

$$G_{23.eq.PU12} := \frac{E_{steel} \cdot A_{23.PU12}}{2\ (1 + v_{steel})\ d_{eq.PU12}} = (2.628 \cdot 10^5)\ \frac{kN}{m^2}$$

Figure C.2: Calculation of input parameters for sheet pile wall PU12.

DEPARTMENT OF ARCHITECTURE AND CIVIL ENGINEERING
CHALMERS UNIVERSITY OF TECHNOLOGY
Gothenburg, Sweden 2026
www.chalmers.se

AVANCEZ
1829
CHALMERS
UNIVERSITY OF TECHNOLOGY